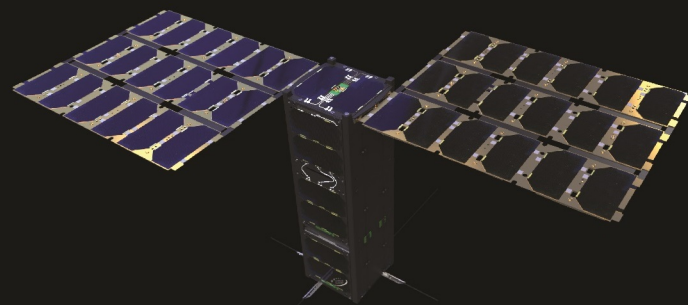


A Metasurface-Based Miniaturized Spectropolarimeter Design

Josip Andrasec

Technische Universiteit Delft



A METASURFACE-BASED MINIATURIZED SPECTROPOLARIMETER DESIGN

by

Josip Andrasec

in partial fulfillment of the requirements for the degree of

Master of Science
in Aerospace Engineering

at the Delft University of Technology,
to be defended publicly on Monday January 14, 2019 at 1:00 PM.

Supervisors:	Dr. ir. J. M. Kuiper,	TU Delft
	Dr. G. Gerini,	TNO Delft
Thesis committee:	Dr. D. M. Stam,	TU Delft
	Dr. ir. A. Cervone,	TU Delft

The work in this thesis was done in cooperation with the TNO Delft, Optics department.

An electronic version of this thesis is available at <http://repository.tudelft.nl/>.

Cover page image: Artists's impression of a cubesat equipped with a spectropolarimeter. Credits:

<https://m.esa.int/spaceinimages/>

<https://www.isispace.nl/cubesats/>

PREFACE

This thesis was done in cooperation with TNO Delft, Optics department. TNO is involved in the development of SPEXone spectropolarimeter. The goal of my thesis internship at TNO was to contribute to a research of novel technology of metasurfaces by conducting a feasibility study of metasurface-based miniaturized spectropolarimeter as a new generation of space spectropolarimeters, for space missions after SPEXone. Many thanks to my supervisor Hans Kuiper at TU Delft Aerospace Engineering faculty for continuous support on this challenging topic, and help in the field of space instrumentation.

It all started during my literature study where I was reviewing possible options for my thesis. During that time, I came across the technology of metamaterials and metasurfaces. After a short time, I found a lot of potential in that technology for space applications. As a first step, I was looking for researchers at TU Delft involved in that field, and have found out that research on metamaterials is already conducting at the Faculty of Applied Sciences, the Department of Imaging Physics. There I met with Aurèle Adam, who suggested me to contact Giampiero Gerini, the person involved in the metasurfaces research group at TNO. Afterwards, he became my daily supervisor. Hereby, I would like to thank him for providing me the freedom during the research, and for supervision during my stay at TNO. Thanks a lot to PhD student Pjotr Stoevelaar for daily helping and teaching me on a wide range of topics. Also, during my thesis internship, I was interacting with many colleges at TNO, and Aerospace Engineering faculty and I would like to thank anyone who helped me on my way. At the end, biggest thanks to my parents and family for continuous support, and encouraging during the study.

*Josip Andrasec
Delft, January 2019*

SUMMARY

This research is focused on the feasibility assessment of a novel technology of metasurfaces in order to design a spectropolarimeter with the thickness of a few micrometers integrated on the detector array. The motivation behind the research is miniaturization of state-of-the-art spectropolarimeters. The requirements for the instrument are derived from SPEXone instrument, as a reference instrument. Beside the miniaturization, two additional requirements are set as a goal: possibility to measure full-Stokes vector of polarization (including circular polarization), and to improve the spectropolarimetric resolution. The reduction in the volume of the instrument is not the main advantage, but also reduction in the number of optical components with respect to the state-of-the-art. A spectropolarimeter with fewer components allows better stability of performances over different external conditions like temperature change, and easier alignment of the whole system.

In recent years the dielectric metasurfaces attract a lot of attention. Firstly, due to its compatibility to CMOS detector technology, which allows integration of thin layers of metasurfaces directly on the detector array, and secondly due to high transmission of the dielectric materials. The metasurface is an array of scatterers with period and size of scatterers smaller than the wavelength. With proper design, the complete control of electromagnetic waves is possible, including amplitude, phase, and polarization at subwavelength resolution. This is convenient because diffraction is not present at that scale. That enables to design optical devices like lenses, waveplates, polarizing beam splitters with similar performances as current technology, but with extreme reduction in thickness.

In this thesis, a systematic electromagnetic performance analysis of metasurfaces is presented. Two types of metasurfaces are designed, first acting as a waveplate, and second as a linear polarizer at different spectral wavelengths. Also, a trade-off of the most suitable spectropolarimetric techniques is done, which led to the Division of Focal Plane (DoFP) type of polarimeter. The combination of these two layers of metasurfaces can modulate the polarization state of light in form of the intensity of light, which is measured on detector pixels. It is shown that with this technique, four unique pixels, each with different polarization modulation, are required to reconstruct four unknowns, the Stokes vector, which fully describes the state of polarization of incident light. Furthermore, the spectral information is measured by designing different sets of four pixels to filter out different parts of the spectrum. The result is two-dimensional detector array which measures spectrum in the vertical axis, and spatial information in the horizontal axis. The spatial information in the vertical axis is achieved by implementing the push broom concept of a satellite. Moreover, the important spectropolarimetric parameters like spectropolarimetric accuracy, spectropolarimetric resolution, and operating spectrum range are estimated. Also, a complete overview of the instrument, which consists of a telescope unit, a bandpass spectral filter and the metasurface integrated on the detector array, is shown. In the end, the performance of the complete system is compared with the reference instrument SPEXone, in order to assess the potential of this concept.

CONTENTS

List of Figures	ix
List of Tables	xiii
1 Introduction	1
1.1 Spectropolarimetry	1
1.2 Applications of Spectropolarimetry from Space	2
1.3 State-of-the-art spectropolarimeters	3
1.4 Introduction to metasurfaces	4
2 Requirements Analysis	5
2.1 Mission overview: SPEXone satellite	5
2.2 Motivation	7
2.3 Mission statement	8
2.4 Requirements List.	8
3 Theoretical Foundation and Methods	11
3.1 Plane-Wave Propagation	11
3.1.1 Plane-Wave Propagation in Lossless Media	12
3.1.2 Plane-Wave Propagation in Lossy Media	12
3.2 The Polarization of Light Waves: Jones and Muller Calculus.	13
3.2.1 Jones Matrix	15
3.2.2 Muller Matrix	16
3.3 Metasurfaces	18
3.3.1 Period of the array	20
3.3.2 Diameter of the Resonators	21
3.3.3 Height of the Resonators	22
3.4 Simulation methods of the Metasurfaces	23
3.4.1 Simulation methods	24
4 Design Concepts	25
4.1 Spectropolarimetric techniques.	25
4.1.1 Modern Polarization Technologies	27
4.2 Selected spectropolarimetric technique.	27
4.2.1 Mathematical Description and Optimization Criteria	28
4.2.2 Stokes error as function of different incident polarization states	32
4.3 Metasurface Design Options	34
4.3.1 Metasurface lattice selection.	35
4.4 Dielectric Metasurface as Micropatterned Waveplate	36
4.5 Dielectric Metasurface as Micropatterned Pleoehroic Fabry-Pérot filter	39
5 Design Analysis	45
5.1 Spatial Resolution.	45
5.1.1 Optical Design Options	46
5.2 Spectropolarimetric Resolution	47
5.2.1 Plane wave's Superposition due to Focused Beam	47
5.3 Transmittance over the spectrum	49
5.4 Fabrication tolerance	51
5.4.1 Impact on Metasurface as Waveplate	51
5.4.2 Impact on Metasurface as Fabry-Pérot Filter.	53

5.5	Performance of complete design (two layered metasurface)	54
5.6	Final concept overview	58
5.6.1	Detector Layout	59
5.7	Polarization Accuracy Calculation	61
5.7.1	Signal-to-noise Ratio Calculation	62
5.7.2	Polarization Uncertainty	64
5.8	Overview of the Results	66
6	Conclusion and Recommendations	69
6.1	Conclusion	69
6.2	Recommendations	70
	Bibliography	71

LIST OF FIGURES

1.1	A schematic illustration of the Stokes parameters. [1]	2
2.1	Light paths through the SPEX optical subsystem. Each of nine arrows in the figure correspond to nine different viewing angle, i.e. connection of nine polarization pre-optics subsystems. [2] .	6
2.2	SPEX polarization pre-optics. Top: schematics. Bottom: mechanical design. For every viewing angle one of polarization pre-optics is attached to the optical subsystem. [2]	6
2.3	Principle of Spectral Modulation. Two bottom bars represent two modulated intensities corresponding to separated beams by PBS. Top bar represents spectrum intensity, which is equal to summation of the two bottom intensities. [2]	7
3.1	(a) Definition of the positive directions of the electric and magnetic vectors for TM waves. (b) Definition of the positive directions of the electric and magnetic vectors for TE waves. [3]	14
3.2	An example of metasurface lens. (a) Scanning electron micrograph showing tilted and (b) top views of a fabricated metasurface lens. (c) Optical microscope image of the center part of a metasurface lens. (d) A 5x5 array of metasurface lenses. [4]	19
3.3	Generic 1-D grating problem with a periodicity of a , where the light is normally incident, the surrounding medium is air ($n = 1$), the refractive index of the grating is n_h , and w is the width of the grating. [5]	20
3.4	Mie resonances of a spherical particle. (A) Scattering efficiency (dimensionless ratio of scattering cross section to geometrical cross section of the particle) versus dielectric permittivity ϵ (lossless particle, $q = 0.5$) for plasmonic ($\epsilon < 0$) and dielectric ($\epsilon > 0$) materials. Abbreviations for resonances: ed, electric dipole; eq, electric quadrupole; md, magnetic dipole; mq, magnetic quadrupole. Higher-order multipole modes are not shown for the sake of simplicity. (B) Scattering efficiency of a lossless dielectric particle (color scale at right) as a function of refractive index n and size parameter. (C) Illustration of electric and magnetic field structures for different electric and magnetic resonances supported by a spherical dielectric particle. [6]	22
3.5	(a) Q_{scat} as a function of wavelength for a Si cylinder in air with $h = 100$ nm and $d = 100$ nm for optical excitation under normal incidence. The peaks correspond to the ED and MD mode, and the corresponding dipole moments and current loops are shown. The polarization of the driving field is shown in the top right. The inset shows the excitation mechanism of the MD mode. (b) Q_{scat} (color) as a function of λ and h for $h = 50$ -250 nm. The particle geometry is shown as an inset. The vertical white line is the crosscut corresponding to the spectrum shown in (a). The white dots correspond to the $\lambda - h$ combinations used for (c-e). (c-e) Normalized electric field intensity $ E ^2$ (color) and electric field lines (gray) in vertical crosscuts through particles with $h = 50$ nm (c), $h = 100$ nm (d) and $h = 175$ nm (e), parallel to the electric driving field. [7]	23
3.6	(a) An example of a simulated geometrical model of the unit cell representing birefringent dielectric metasurface with the hexagonal lattice. (b) Top Floquet port. (c) Bottom Floquet port. (d) The boundary condition of the side walls representing infinite array (only one pair is shown due to clarity)	24
4.1	Venn diagram of polarization measurement/modulation domains [8]	26
4.2	Schematic illustration showing how the waveplate and linear polarizer modify the two different types of the incident state of polarizations. (a) The waveplate transforms the first type of elliptical polarization into linear horizontal polarization. The linear polarizer is oriented in horizontal plane, and all light is transmitted. (b) The waveplate transforms the second type of elliptical polarization into linear vertical polarization. The linear polarizer is oriented the a horizontal plane, and no light is transmitted. (c) Definition of the three angles: α , δ , and θ	30
4.3	Schematic representation of the more general DoFP concept. A set of four different modulating pixel form a superpixel. Three angles are required to fully describe each pixel: α , δ , and θ	31

4.4	(a) Stokes parameters vs. sample number diagram. Sample number is related to different incident polarization states, as indicated on the Poincaré sphere (b), starting from the bottom, and ending at the top of the sphere. (c) The standard deviation of error in estimated Stokes vs. sample number diagram due to the shot noise. Blue points represent 1 superpixel, while red points 10 same superpixels. (d) Four points (Configuration 2 , Table 4.2) forming tetrahedron inscribed inside Poincaré sphere, which represent response of four combinations of waveplates (α , δ) and linear polarizers (θ).	33
4.5	A general overview of metasurface-based applications on polarization control and wavefront shaping [9]	34
4.6	(a) top view of an elliptic cylinder oriented at an angle φ with respect to the x axis. The R_a and R_b are the minor and major axis of the ellipse, respectively. (b) and (c) are two considered types lattices, square, and hexagonal, respectively. (d) Transmittance vs. cylinder's orientation angle, φ diagram for four different geometrical models of the simulated unit cell of the metasurfaces: two different lattices, and two different diameters of the ellipse.	36
4.7	(a) The geometrical model of the simulated unit cell of the metasurface consisted of an array of elliptic cylinders in a hexagonal lattice (with minor and major diameters: $D_x = 108$ nm, and $D_y = 244$ nm). (b) The result of the simulation. The left side of the vertical axis corresponds to the transmittance, and the right side of the vertical axis corresponds to the phase of the electric field. Solid lined represents the polarization in x , and the dashed line represents the polarization in y direction. On the horizontal axis is free space wavelength. (c) Closer look for the shorter range of the spectrum, where can be seen how the transmittance and retardance are mostly uniform.	37
4.8	(a) The geometrical model of the simulated unit cell of the sub-wavelength grating, with the rectangular grating width of $w = 65$ nm, the height of $h_g = 100$ nm, and the grating period of $a_g = 220$ nm (b) The result of the simulation. The left side of the vertical axis corresponds to the transmittance, and the right side of the vertical axis corresponds to the phase of the electric field. Solid lined represents the polarization in x , and the dashed line represents the polarization in y direction. On the horizontal axis is free space wavelength. (c) Closer look for the shorter range of spectrum, where can be seen how the transmittance and retardance are mostly uniform.	38
4.9	Transmission of a light wave with electric field amplitude E_0 through a Fabry-Pérot resonator. [10]	40
4.10	Schematic of the proposed bandpass filter array composed of vertical DBR-based micro-cavities, in which transmissive dielectric metasurface layers are inserted as phase shifting layers to tune their resonance wavelengths over a broad bandwidth. [11]	41
4.11	(a) Front view of the geometrical model of the unit cell of a FP cavity formed by two DBR mirrors consisted of 6 pairs of layers. The selected materials of the high and low refractive index of DBR are TiO_2 , and SiO_2 , respectively. The cavity is made of same material as low refractive index material of DBR. The following dimensions are used in the geometrical model: the period of lattice is $a = 500$ nm, thickness of TiO_2 layers $h_L = 108.052$ nm, thickness of SiO_2 layers $h_H = 172.3662$ nm, length of the cavity $L_{cav} = 516.5$ nm (b) Isometric view of same geometrical model. (c) Front view of the same geometrical model as in the previous model with the addition of embedded $a - Si$ elliptic cylinder inside the cavity. The following dimensions are used in the geometrical model: the period of lattice is $a = 500$ nm, thickness of TiO_2 layers $h_L = 108.052$ nm, thickness of SiO_2 layers $h_H = 172.3662$ nm, length of the cavity $L_{cav} = 466.5$ nm, the height of the elliptic cylinder $h_c = 200$ nm, the diameters of ellipse $D_x = 100$ nm, and $D_y = 400$ nm. (d) Isometric view of the FP cavity with the embedded $a - Si$ elliptic cylinder.	42
4.12	(a) The blue area represents reflectance of simulated DBR mirror consisted of 6 layer pairs. Furthermore, the red solid and dashed line represents transmittance vs wavelength for the FP filter consisted of 6 layer pairs of DBR. Resonant wavelength is located at 1000 nm. (b) FP filter: transmittance vs wavelength for 6, 5, and 4 pairs of layers of DBR.	43
4.13	Transmission vs. wavelength for simulated DBR with 6 pairs of layers, with embedded $a - Si$ elliptic cylinder inside the cavity. Pleochroic Fabry-Pérot filters for different aspect ratio of the ellipse show shift in central wavelengths for two orthogonal polarizations	44

4.14	Uniformly distributed pleochroic FP filters with their center wavelengths stacked periodically in order to cover the finite spectrum with high spectral resolution. The broadband filter is implemented to allow measurement of transmitted peaks of only one orientation of polarization (T_{xx} in this case). In this plot are shown 20 different spectral bands from 1000 to 1020 nm, with a period of 1 nm. The shift in central wavelengths between two orthogonal polarizations is 30 nm. Note that, this is not the result of simulation, but only illustration of the concept.	44
5.1	Definition of the important parameters used in this chapter. [12]	46
5.2	An image space telecentric lens, where the chief rays are all parallel to the optical axis in image space. Note that the image height does not change regardless of where the sensor plane is positioned, as the chief rays defining image height are all parallel to the optical axis. [13]	47
5.3	(a) Graphical illustration of the FB filter with the definition of the incident plane wave angle θ_0 . (b) Result of simulation of FP filter. Transmittance vs wavelength diagram, for different incident angles of plane waves. The used geometrical model in simulation is from Fig. 4.13, AR=4. The transmittance correspond to x polarization orientation ($ T_{xx} ^2$). The used geometrical model in simulation is from Fig. 4.13, AR=4. The transmittance correspond to x polarization orientation ($ T_{xx} ^2$).	48
5.4	(a) Schematic illustration of half cone angle of the focused beam, Θ impinging normally on the FP filter. (b) Transmittance ($ T_{xx} ^2$) vs wavelength for the plane wave and four half cone angles, Θ . The used geometrical model for simulation is from Fig. 4.13, AR=4. For the plane wave and $\Theta = 2$ deg, the spectral resolution is about $FWHM = 1.1$ nm.	49
5.5	(a) Simulated structure with an array of $a - Si$ elliptic cylinders embedded inside the FP cavity. (a) Simulated structure with a TiO_2 sub-wavelength grating embedded inside the FP cavity. (c) The transmittance of the FP filters with an array of $a - Si$ elliptic cylinders embedded inside the cavity for three simulated wavelengths: 1000, 895, and 791 nm. (d) The transmittance of the FP filters with a TiO_2 sub-wavelength grating embedded inside the cavity for three simulated wavelengths: 796.8, 589.1, and 401.6 nm. (e) Refractive index vs wavelength for $a - Si$, and TiO_2 (real part n , and imaginary part k)	50
5.6	(a) Graphical illustration of the simulated unit cell of $a - Si$ elliptic cylinder on the SiO_2 substrate. (b) Top view, indicating diameters of the ellipse (D_x and D_y). (c) and (d) Contour maps (as a function of ellipse diameters D_x and D_y) of the transmittance for x and y polarization directions, respectively. (e) Contour map of the subtraction between transmittance in x and y polarization directions, which is indication of unequal transmittance. (f) Contour map of the retardance, $\delta = \delta_x - \delta_y$. The marker points with the shape of a triangle pointing down, and the triangle pointing up correspond to the closest retardances that are optimized in Table 4.2. The black dots around those two markers points are the diameters of ellipse inside the tolerance of the fabrication. The other two marker points, the triangle pointing to the right and to the left, represent worst case, where the difference in transmittance is the worst.	52
5.7	(a) CN vs. random sampling of diameters of the ellipse and fast axis. (b) Poincare sphere, where blue tetrahedron represents the ideal response of the four pixels, and the red dots are the result of random sampling, representing a deviation in polarization modulation due to fabrication tolerance.	53
5.8	Contour map of center wavelength for different diameters of the ellipse. Black dots show region inside the tolerance range.	54
5.9	A simulation showing expected deviation in center wavelengths (due to the fabrication error) from a planned uniform coverage of the spectrum.	55
5.10	(a) Graphical illustration of the simulated unit cell with an elliptic cylinder placed on the top of the FP filter, separated by the spacer with thickness t (corresponding to Pixel A). (b) Transmittance vs spacer thickness diagram of Pixel A . (c) Transmittance vs spacer thickness diagram of a glass slab.	55
5.11	Mueller parameters (the first row of the Mueller matrix) vs spacer thickness diagram for all four pixels.	57
5.12	The total error in Mueller parameters (sum for all four pixels) vs spacer thickness diagram. Also, the overall error as the sum of all parameters (green curve).	58
5.13	Four unit cells of the simulated two layered metasurfaces, with spacer thickness of 300 nm. Pixels from A to D correspond to (a) to (d), respectively.	58

5.14	Functional Flow block diagram for the metasurface-based spectropolarimeter design.	59
5.15	(a) Graphical illustration of the design of the superpixel (four pixels), consisting of the two-layered metasurface integrated on the detector array. (b) Front view of the superpixel. Note that scheme is not in scale.	60
5.16	(a) Top view of the metasurface as the waveplate with different arrays of elliptic cylinders over the four pixels. (b) Cut-section of the metasurface embedded in the FP filter, with different arrays of elliptic cylinders over the four pixels. Note that scheme is not in scale.	60
5.17	Overview of the detector layout. The superpixels consisted of 4 differently modulated surfaces integrated on the detector array. The horizontal axis corresponds to spatial (image swath), and the vertical axis corresponds to the spectral axis (image length).	61
5.18	Minimum and maximum expected radiance vs wavelength. [14]	62
5.19	Quantum efficiency vs wavelength diagram. Spectral response of a monochrome CMV4000 with the microlenses image sensor. [15]	63
5.20	SNR vs wavelength diagram.	64
5.21	(a) A configuration of superpixels arranged in one line along the swath axis, resulting in 20 superpixels. (b) A configuration of superpixels arranged in five lines along the swath axis, resulting in 100 superpixels.	65
5.22	The standard deviation of error in estimated Stokes vs different incident polarization states (sample number) diagram. Blue points represent 1 superpixel, red points 20 superpixels, and 100 superpixels.	66

LIST OF TABLES

2.1	Requirements overview for SPEXone and Metasurface-based design. Note that parameter <i>Maximum spectral bandwidth</i> refers to the range of wavelengths that can be measured in the designed instrument, while the <i>Achievable spectral range</i> refers to the possible wavelengths for which an instrument can be designed.	9
4.1	The trade-off table for the most suitable spectropolarimetric technique for the metasurfaces. . .	28
4.2	Result of optimization of matrix, \mathbf{W} for two the different configurations. The parameters used in optimization are: α , δ , and θ . In Configuration 1 , only θ is constrained, and the chosen value is 90 deg. In Configuration 2 , two parameters are constrained: α , and θ . The chosen values $\alpha = [60\ 60\ 120\ 120]$, and $\theta = [0\ 120\ 0\ 60]$. The criteria for the optimization is minimization of condition number, CN . Values of angles are in degrees, and the font of the results of optimization is in bold text style.	32
5.1	Overview of the parameters for the best and worst case. Values of angles are in degrees	53
5.2	Overview of the Mueller matrices for all four pixels: the simulated model with a spacer thickness of 300 nm, and ideal model.	56
5.3	Overview of the parameters used in the signal calculation, Eq. (5.16).	63
5.4	Overview of the parameters used in the noise calculation, Eq. (5.17).	64
5.5	Comparison of the requirements of the SPEXone and Metasurface-based design. The color of the text denotes advantage (green color) and disadvantage (red color) over reference instrument SPEXone.	67

1

INTRODUCTION

1.1. SPECTROPOLARIMETRY

Spectropolarimetry is the spectroscopic study of the polarization properties of the observed scene. Spectropolarimetry is a general form of conventional optical spectroscopy. The optical spectroscopy endeavors to measure the reflectance of the observed scene as a function of wavelength. In addition to that, spectropolarimetry also determines the state of the polarization. [16] Spectropolarimetry found many applications in science and engineering, as well as in space. Spectropolarimeter is an optical instrument for the determination of the polarization state of an incident light beam at different wavelengths. In space applications, a spectropolarimeter is integrated to the telescope onboard spacecraft pointing at the Earth or some other celestial body. In classical electromagnetism, the light is defined as electromagnetic radiation consisting of electromagnetic (EM) transverse waves, which are synchronized oscillations of electric and magnetic fields that propagate at the speed of light, in a vacuum. The polarization of a monochromatic wave, which is a discrete wavelength in the spectrum, refers to the direction of the electric field in the plane perpendicular to wave propagation. In nature, the sunlight which illuminates the earth is essentially unpolarized. The scattered light from the ground has a surprisingly large degree of polarization, which is mostly linearly polarized. The circular polarization can occur if scattered light has one-quarter of a wavelength phase shift between two orthogonal directions. That results in a polarization state in which, at each point, the electric field of the wave has a constant magnitude but its direction rotates with time at a steady rate in a plane perpendicular to the direction of the wave. Since the detectors used in telescopes are sensitive only on the intensity of the EM waves, it is convenient to define the polarimetric information in terms of intensity. Common formalism in polarimetry is Stokes vector. Stokes parameters can be written in terms of intensities, where I_x , I_y , $I_{+\frac{1}{4}\pi}$, $I_{-\frac{1}{4}\pi}$, I_l , and I_r represent the intensities transmitted by an ideal variable polarizer placed in the path of the EM waves and adjusted to transmit the x , y , $+\frac{1}{4}\pi$, $-\frac{1}{4}\pi$, linear polarizations and the left (l) and right (r) circular polarizations, respectively [17]:

$$S_0 = I_x + I_y \quad (1.1)$$

$$S_1 = I_x - I_y \quad (1.2)$$

$$S_2 = I_{+\frac{1}{4}\pi} - I_{-\frac{1}{4}\pi} \quad (1.3)$$

$$S_3 = I_r - I_l \quad (1.4)$$

The Stokes parameters of a monochromatic light wave can be grouped in a 4x1 column vector, called Stokes vector:

$$\mathbf{s} = \begin{bmatrix} S_0 \\ S_1 \\ S_2 \\ S_3 \end{bmatrix} = \begin{bmatrix} I \\ Q \\ U \\ V \end{bmatrix} \quad (1.5)$$

In Eq. (1.5) the formalism with parameters $[S_0 \ S_1 \ S_2 \ S_3]^T$ is commonly used in the remote sensing, while $[I \ Q \ U \ V]^T$ is used in astronomy. The schematic illustration of Stokes parameters is shown in Fig. 1.1.

The Stokes parameters of a totally polarized wave satisfy the following condition:

$$S_0^2 = S_1^2 + S_2^2 + S_3^2 \quad (1.6)$$

An important quantity in the description of partially polarized light is the degree of polarization, p which is defined as the ratio of the intensity of the totally polarized component to the total intensity of the EM wave:

$$p = \frac{\sqrt{S_1^2 + S_2^2 + S_3^2}}{S_0} \quad (1.7)$$

The degree of polarization varies from zero for unpolarized light to unity in the case totally polarized light. The degree of linear *DoLP* and circular *DoCP* polarization is usually expressed separately:

$$DoLP = \frac{\sqrt{S_1^2 + S_2^2}}{S_0} \quad (1.8)$$

$$DoCP = \frac{S_3}{S_0} \quad (1.9)$$

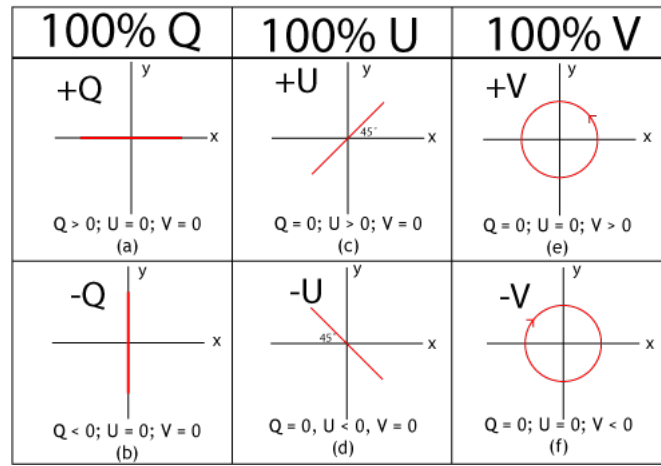


Figure 1.1: A schematic illustration of the Stokes parameters. [1]

1.2. APPLICATIONS OF SPECTROPOLARIMETRY FROM SPACE

The incident light that is scattered by particles in the atmosphere like water droplets, ice crystal, and dust can be polarized. The resulting degree of polarization depend on particle type and size, particle shape, type of scattering, and relative positions of light source, particles, and observer. That can induce a large number of different effects that can be observed. Polarimetry is a key method in atmospheric research, which can provide a characterization of aerosol particles. Remote retrieval of several aerosol properties: the aerosol optical thickness, size distribution, the chemical composition and the particle shape can be retrieved only by the combination of polarization measurements of scattered sunlight with multi-spectral and multi-angle functionality [18], [19]. Also, the measurements are useful to assess the health hazards of aerosols and to probe volcanic ash clouds that impact air traffic. [8] The POLDER instrument has pioneered space-based polarimetric remote sensing. POLDER is a fisheye imager, which implements a filter wheel for multi-spectral and multi-polarization measurements. The wavelength filters (433,670, 865 nm) are repeated three times and with combination of linear polarizers at 0, 60 and 120 degrees. That allows measurements of the linear Stokes parameters for each of the filter bands after three positions of the filter wheel. Because the filter wheel rotates during the flight of the satellite, the three recordings are not the same. The polarimetric accuracy for POLDER measurements is $\approx 2\%$ for scenes with large spatial gradients. [8] A polarimetric accuracy of $\approx 10^{-3}$

is required in order to provide more information about the chemical composition of aerosol particles. [8] Different spectropolarimeter designs are developed that can provide high accuracy polarimetry. One of these instruments is SPEX, which is discussed in next chapter (Chapter 2) as a reference instrument.

Another application of polarimetry is used for detection and characterization of exoplanets or small Solar System bodies. In spatially unresolved polarimetry of exoplanets, the starlight reflected by a planet will usually be polarized, due to scattering within the planetary atmosphere and/or reflection by the surface, while the starlight is unpolarized. [20] The polarimetry is used to enhance the contrast in exoplanets signal. Also, polarimetry can offer additional information (along spectrum), which is important to obtain a physical characterization of celestial bodies. The change of linear polarization of scattered sunlight in different illumination conditions can provide information about some properties of the surface of atmosphereless asteroids. [21]

The circular polarization is very interested in astrobiology. The circular polarization spectrum has the potential to provide a very pure biosignature, which is based on the homochirality of biological molecules together with their optical activity. Typical DoCP levels in the solar system are from 10^{-4} to 10^{-5} , with the highest being Mercury with an integrated DoCP of $\approx 10^{-4}$. [22] Furthermore, the DoCP of comets can reach 2%, although in the majority of comets these values are more typically 0.05–0.2%. [22] The remote sensing of circular polarization is still an area that is not explored well. For example, the light scattered by microbes is in the range 10^{-3} to 10^{-4} in DoCP, which can be an order of magnitude or more higher than typical abiological signals. Another possible application could be a study of vegetation. For instance, DoCP for light reflected by maple leaves is in range between 0.2 to 0.5%, in the vicinity of the chlorophyll absorption features. Depending on the application, the polarimeter should be capable of measuring a DoCP of at least 10^{-4} .

1.3. STATE-OF-THE-ART SPECTROPOLARIMETERS

As the commercial space companies are rapidly growing with the high popularity of miniaturizing space satellites, there is an interest in developing small spectropolarimeters that could fit in small satellites like CubeSats. The miniaturization of instruments allows to fly multiple instruments in a satellite constellation. That improves global coverage and temporal sampling. One of the examples is SCARBO (Space CARBOn Observatory) project, which proposes a novel miniaturized static spectrometer concept on a constellation of small satellites, coupled with aerosol sensors and high-end reference instruments. [23]

The conventional high resolution diffraction grating based spectrometers are inevitably bulky as the resolution of the spectrometer scales inversely with optical path length. [11] In the case of spectropolarimeters, the systems becomes even more complex. To measure polarimetric information as function of wavelength of incident light various techniques are developed over time. Usually, this requires additional optical elements to separate or modulate polarimetric information. One of the main challenges of a spectropolarimeter is the requirement in detection of multiple parameters. An imaging spectrometer is an instrument used to acquire a spectrally-resolved image of the scene, also known as a datacube due to the three dimensional representation of the data. In the case of Stokes imaging spectropolarimeter, additional dimension is required, resulting in four-dimensional (two spatial, one spectral, and one polarization) datacube. Since the most used detector arrays are a two-dimensional arrays, the challenge is to "project" four-dimensional array into a two-dimensional detector array.

Since the measured parameter at the detector pixel is intensity, the state of polarization (SOP) measurement requires some sort of modulation of the light. Therefore, the polarimetry involves the manipulation of light such that several independent intensity measurements can be combined to estimate the polarization state of the incident light. Usually these intensity measurements are related to the state of the polarization by the transformation matrix, which contains information of modulation (manipulation) of the light at each individual detector pixel. The goal of every polarimeter design is to ensure that these intensity measurements are arranged in the most optimal way. The reduction of error amplification after SOP reconstruction is the parameter which is optimized. There are many sources that introduce an error in the measured intensity, to mention a few: shot noise, detector read-out noise, error due to imperfect optical components. Several measurement domains are available for polarization measurements: the spatial domain, the temporal domain, and the spectral domain. [8] Each of these domain modulate the SOP in a different physical domain, but

the principle does not change. For instance, in spatial domain, the pixels that are initially meant to measure the intensity of different spatial locations are used to encode the SOP. That means that the spatial resolution is decreased. Therefore, there is always a trade-off between spatial, spectral and temporal parameters. The selection of the domain depend on the requirements of the spatial, spectral and temporal resolution. Further discussion on spectropolarimetric techniques continues in the Chapter 4.

1.4. INTRODUCTION TO METASURFACES

Metamaterials are artificially created composite materials consisted of a set of scatterers in a regular array in three-dimensional space, designed in such way to modify the incident electromagnetic wave in transmission or reflection. Generally, the size of the scatterers and periodicity of the array is closely related to the wavelengths of the incident wave. The main purpose of developing such materials is to achieve some properties that are not found in natural homogeneous materials. For instance, there are many demonstrations of developing metamaterials with properties like negative refractive index, near-zero index, etc. [24] The progress of metamaterials is very rapid. Over a short period of time, the research of metamaterials had progressed from a theoretical concept to realized physical devices in just a few decades. The metamaterials can be considered as three-dimensional structures, which modifies the EM waves in similar way as natural materials, by propagation through them. The cumulative effect of such structure makes them necessary a thick optical device since the effect of modification of EM waves depend on the propagation path through the material. There is a class of metamaterials, called the metasurfaces, where the scatterers are arranged into a two-dimensional pattern. In this case, the modification of EM waves is achieved by shaping the cross-section of the scatterers, while their height is kept the same. The advantage of the metasurfaces is a reduction in physical space, with respect to three-dimensional metamaterials. [24] The interesting type of the metasurfaces are the dielectric metasurfaces. Firstly due to its compatibility to CMOS detector technology, which allows integration of a thin layer of a metasurface directly on the detector array, and secondly high transmission of the dielectric materials. The period and size of the scatterers is smaller than the wavelength. Therefore, the complete control of EM waves can be achieved: amplitude, phase, and polarization at subwavelength resolution. This is convenient because diffraction is not present at that scale. That enables to design optical devices like lenses, waveplates, polarizing beam splitters with similar performances as current technology, but with extreme reduction in thickness. A more detailed explanation of metasurfaces is presented in Chapter 3.

2

REQUIREMENTS ANALYSIS

In this chapter the requirements of the state-of-the-art spectropolarimeters are analyzed. The SPEXone instrument is used as a reference instrument in this research. In the first section, the concept of the SPEXone instrument is discussed. Then, in the second section, the motivation for this research explained. In the third section the mission statement of research is presented. In the end, in the fourth section, the requirements for this research are derived, which are based on the reference instrument SPEXone with additional modifications, in order to open possibilities for new applications.

2.1. MISSION OVERVIEW: SPEXONE SATELLITE

The SPEXone (Spectro-polarimeter for Planetary Exploration) is an instrument concept planned to be equipped as one of the scientific instruments on NASA's PACE (Plankton, Aerosol, Cloud, ocean Ecosystem) mission. The launch of the spacecraft is scheduled in 2022 into low earth orbit with nominal altitude of 675.5 kilometers. [25] The purpose of the instrument is to measure the characteristics of aerosols in the Earth's atmosphere with a spectropolarimetric technique of spectral modulation. The SPEXone, as an evolution of previous SPEXlite instrument, is developed by a consortium consisting of SRON and Airbus Defence and Space NL, and supported by unique expertise from partner TNO. [2]

Some of the characteristics of the SPEXlite are the high polarimetric accuracy, large viewing angle with high spatial resolution. The principle from SPEXlite was taken in order to develop a compact instrument with five viewing angles and two polarizations projected on a single detector array. The SPEXone is designed as a six-unit CubeSat payload. [2] It has optical functions as spectral modulation, multi-angle imaging and spectrophotometry. [2] The spectral radiance and state of linear polarization are measured in the optical band in the range of 385-770 nm with 2 nm resolution [25], while the spectral resolution for polarization ranges from 20 to 40 nm (depending on the wavelength) according to [26]. This decrease in spectral resolution for polarization is due to the spectral modulation technique, where some finite bandwidth in the spectrum is required in order to encode the polarization information. The instrument has five viewing angles (-57°, -20°, 0°, 20°, 57°). [25] Each viewing angle has a swath of 9 degrees in the across-track direction corresponding to 100 km on the ground. [25] The ground sample distance is 2.5 km. [25] Every viewing angle port operates as a separate pushbroom spectrometer, producing five overlapping strips of data on the ground. That ensures a multi-angular view of ground scenes.

The SPEX utilizes the spectral modulation technique to encode the degree of linear polarization (DoLP) and angle of linear polarization (AoLP) of sunlight scattered by the Earth's atmosphere and the particles on the path. This is achieved by encoding the degree and angle of linear polarization of the incoming light in a sinusoidal modulation of the flux spectrum. The spectral modulation is realized by three optical elements in series. First light passes through a quarter-wave retarder (QWR), then an achromatic multiple order retarder (MOR), and finally through a polarizing beam splitter (PBS). [2] The wavelength-dependent phase shift of the incoming light is accomplished by MOR, which will result in different amplitude and phase of sinusoidal modulation as a function of wavelength. Then PBS acts as two orthogonal linear polarizers, with two separated beams at some angle, which are later projected on a single detector array. The intensity pattern along

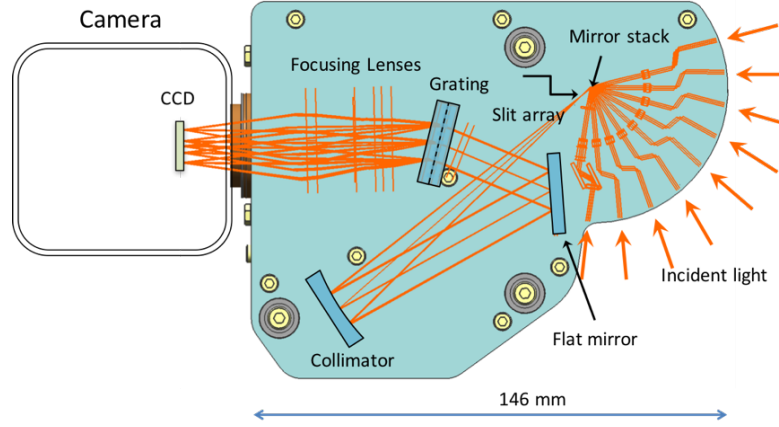


Figure 2.1: Light paths through the SPEX optical subsystem. Each of nine arrows in the figure correspond to nine different viewing angle, i.e. connection of nine polarization pre-optics subsystems. [2]

the spectrum axis of the detector will result in two different sinusoidal functions which are in anti-phase. These two sinusoidal modulation of the intensity spectrum are related to the DoLP and AoLP by amplitude and phase of a sine function, respectively. This modulation can be seen in Fig. 2.3. Equation 2.1 relates the modulated spectrum of the two beams, $I_{\pm}(\lambda)$ and linear polarization state: $P_L(\lambda)$ (DoLP), and $\Phi_L(\lambda)$ (AoLP). [26]

$$I_{\pm}(\lambda) = \frac{I_0(\lambda)}{2} \left(1 \pm P_L(\lambda) \cos\left(\frac{2\pi\delta(\lambda, T)}{\lambda} + 2\Phi_L(\lambda)\right) \right) \quad (2.1)$$

where $I_{\pm}(\lambda)$ is the modulated spectrum, $I_0(\lambda)$ is the incoming flux, $\delta(\lambda, T)$ is the retardance of the retarder (waveplate), and λ is wavelength. [27]

The function of the QWP is to change linearly polarized light with polarization axis along the optical axes

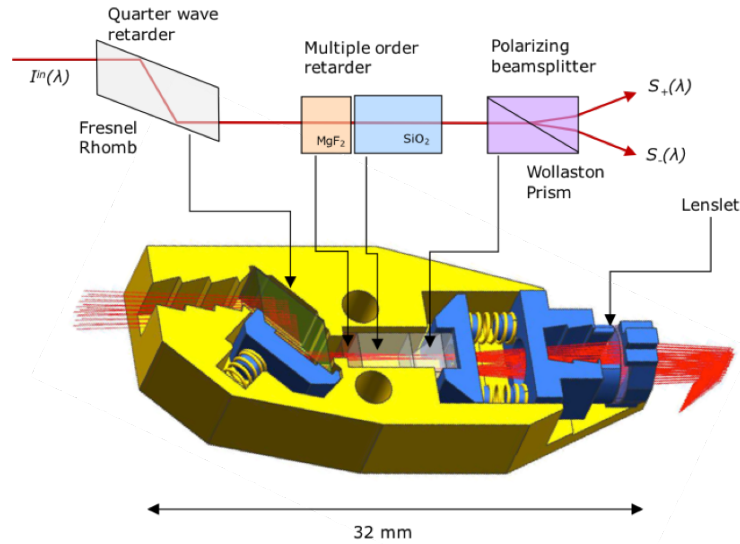


Figure 2.2: SPEX polarization pre-optics. Top: schematics. Bottom: mechanical design. For every viewing angle one of polarization pre-optics is attached to the optical subsystem. [2]

of the MOR into circularly polarized light. [2] The MOR is a composite of two slabs of birefringent crystals: MgF2 and Quartz, where the retardance of combined retarder results in a modulation period of 7nm at 400nm, and 20nm at 800nm. [2] This modulation period limits the spectral resolution for the polarization, since the finite length of modulated sinusoidal curve is used in an algorithm to reconstruct the state of the polarization. In sum, the DoLP and AoLP are derived by determining the amplitude and phase of the modulated intensity spectrum, while the spectral radiance is obtained by summing up the modulation spectra of both beams separated by PBS. The complete assembly of SPEXone consists of five identical pre-slit optical elements (Fig. 2.2) used to encode the state of polarization, and spectrometer (Fig. 2.1) consisting of collimator and diffraction grating. Between those two components is an array of slits (denoted with arrows in Fig. 2.1), which defines the field of view of viewing ports. Once the polarization state of the light is encoded in pre-slit optics, it passes through the slit, then it is collimated by a spherical mirror, folded by a flat mirror, and spectrally dispersed by a holographic grating. In the end, the light is re-focused by a set of nine lenses onto a 2k x 2k CCD detector array. [2]

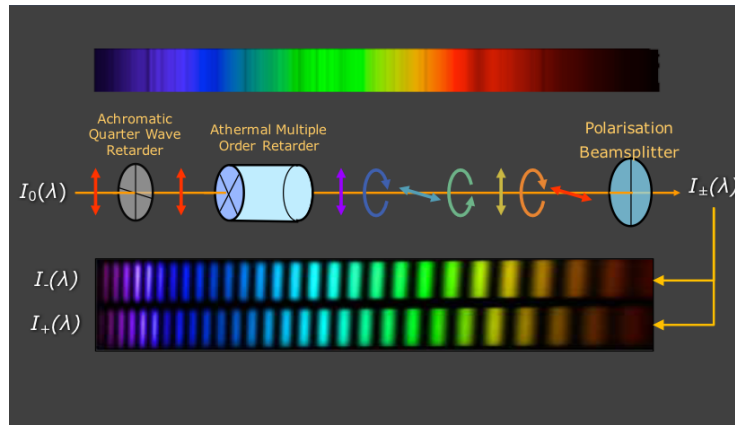


Figure 2.3: Principle of Spectral Modulation. Two bottom bars represent two modulated intensities corresponding to separated beams by PBS. Top bar represents spectrum intensity, which is equal to summation of the two bottom intensities. [2]

2.2. MOTIVATION

The state-of-the-art instruments consist of multiple optical components, and that is their biggest disadvantage. Multiple components make those systems fragile and their performance is sensitive to small variation in the design. By increasing the instrument's complexity, the development becomes long and expensive. The performance of the system is very sensitive to small changes in a single component, which might introduce large error in whole system chain. That makes calibration difficult, and accuracy of the instrument can be limited. The additional problem arises when these instruments are used in space, where a large difference in temperature is present at different areas of instruments. Thermal expansions of different components can introduce errors, which are sometimes hard to compensate. An important requirement of spectropolarimeter is the polarimetric measurement of a large spectral range. That requires the polarization optics (linear polarizers, waveplates) that perform over large spectral ranges, which is not always easy task since the polarization optics is almost by definition chromatic. [8]

In practice, there are several deviations from the ideal case of polarizing optics. For instance, the actual retardance value of the retarder half-wave plate may deviate from the nominal π value and the transmission of the ordinary and extraordinary beam are not identical, even after flat fielding correction. [28] Also, dispersive optics is not ideal, where transmission for two orthogonal polarizations change as a function of wavelength.

In summary, state-of-the-art spectropolarimetry are:

- Handcraft manufactured
- Fragile

- Expensive
- Bulky
- Non customizable

The main motivation for this research is to assess and propose an alternative instrument to state-of-the-art spectro-polarimeters, which is a few micrometers thick micro-patterned layer, directly integrated on the detector array. That would allow an extreme reduction in the number of required optical components (like a diffraction grating, waveplates, and polarizing beam splitters), and consequently unlock new possibilities for smaller satellites to be equipped with such instruments. Another reason is increasing spectral resolution for polarization, which is a drawback of spectral modulation technique since the required spectral bandwidth is necessary to modulate polarization. Lastly, usually, instruments have the only possibility to measure the linear polarization, while circular polarization still stays a challenge of imaging polarimeters. For that reason, a full-Stokes concept that can measure also circular polarization could open possibilities in remote sensing and astronomy.

In summary, the motivation for the research is:

- Reduction in the number of optical components and the volume of the instrument
- Improvement in spectral resolution for polarization
- Adding the possibility to measure circular polarization (full-Stokes spectro-polarimeter)

2.3. MISSION STATEMENT

The mission of the research is to assess the feasibility of miniaturizing state-of-the-art spectro-polarimeters, by implementing a few micrometers thick layer of metasurface directly integrated on the detector array, without reduction in the required spectropolarimetric performances.

2.4. REQUIREMENTS LIST

In this section, the requirements that are considered in this research are derived. The starting point is the reference instrument SPEXone. The goal of this research is to assess the feasibility of a metasurface-based spectropolarimeter. The requirements for the spectropolarimetric performances are taken to be comparable to the reference mission. In addition to that, as explained in subsection 2.2, the requirements related to the volume of the instrument, spectral resolution for polarization, and circular polarization capability are made more strict with respect to the reference instrument. The reason for that is the potential in the metasurfaces, which could enable the improvements in those three aforementioned parameters. In Table 2.1, the requirements for two instruments, the first reference mission SPEXone, and the second instrument considered in this research are presented. Because the SPEXone is designed with a specific purpose for the retrieval of the relevant aerosol and cloud products, the need for multiple viewing angles is an important requirement. In this research only one viewing angle is considered, the reason for that is the simplification of the research, with a focus on the spectropolarimetric part of the instrument, not the optical subsystem. This modification of adding additional viewing angles belongs to the optical subsystem, which can be designed independently from spectropolarimetric subsystem (thin layer integrated on detector array). The difference between single and multiple viewing ports is only in how the beams from different orientations are projected onto the single detector array. The purpose of this research is to provide a more general result of performances for metasurface-based spectropolarimeter, which can be easily customizable to different applications.

Table 2.1: Requirements overview for SPEXone and Metasurface-based design. Note that parameter *Maximum spectral bandwidth* refers to the range of wavelengths that can be measured in the designed instrument, while the *Achievable spectral range* refers to the possible wavelengths for which an instrument can be designed.

Parameter	SPEXone	Metasurface-based design
Swath width	9° (100 km) [25]	9° (100 km)
Viewing angles	5 (-57°, -20°, 0°, 20°, 57°) [25][29]	1
Achievable spectral range	385-770 nm (extended to 385-1600) [26][29]	400-1600 nm
Maximum spectral bandwidth	385-770 nm [26][29]	100 nm
Spectral resolution intensity	4 nm [29]	2 nm
Spectral resolution for polarization	20-40 nm [29]	2 nm
Spatial sampling	2.3x2.7 km ² [29]	2.5x2.5 km ²
Stokes parameters measurements	S ₀ , S ₁ , S ₂ [2] [29]	S ₀ , S ₁ , S ₂ , S ₃
Polarimetric accuracy, DoLP	0.003 [29]	0.003
Polarimetric accuracy, DoCP	-	10 ⁻⁴
Volume	6-unit-CubeSat payload [2]	1-unit-CubeSat payload

3

THEORETICAL FOUNDATION AND METHODS

In this chapter, a theoretical foundation of this research is presented. The first subsection contains an overview of the plane-wave propagation of electromagnetic (EM) waves in the lossless and lossy media. Then, mathematical description of polarization of EM waves is derived in form of Jones and Muller calculus. After that, the theoretical background of the metasurfaces is provided. In the end, the implemented simulation methods of the metasurfaces are described.

3.1. PLANE-WAVE PROPAGATION

An EM wave produced at a localized source expands outwardly in the form of a spherical wave traveling at the same speed in all direction through free space. The plane-wave propagation is introduced in order to approximate the spherical wave at some distant location from the source. The wavefront of the spherical wave appears approximately planar to an observer's aperture located far away from the source. Even though uniform plane waves do not exist, they are used as a concept for the physical understanding of wave propagation in lossless and lossy media.

The purpose of the subsection is not to provide a full derivation of the equations but to show final equations that are used to solve propagation of EM waves in simulation software HFSS (explained in Section 3.4). The theory is based on [30] and [31].

The reduced form of Maxwell's equations in phasor form:

$$\nabla \cdot \tilde{\mathbf{E}} = 0, \quad (3.1)$$

$$\nabla \times \tilde{\mathbf{E}} = -j\omega\mu\tilde{\mathbf{H}}, \quad (3.2)$$

$$\nabla \cdot \tilde{\mathbf{H}} = 0, \quad (3.3)$$

$$\nabla \times \tilde{\mathbf{H}} = j\omega\epsilon_c\tilde{\mathbf{E}}. \quad (3.4)$$

where $\tilde{\mathbf{E}}$, and $\tilde{\mathbf{H}}$ are electric and magnetic vector phasors in the frequency domain, respectively. ω is angular frequency, μ is magnetic permeability, and ϵ_c is the complex electrical permittivity.

$$\epsilon_c = \epsilon - j\frac{\sigma}{\omega} = \epsilon' - j\epsilon'' \quad (3.5)$$

where ϵ is electrical permittivity, σ is conductivity. Also, it can be written in terms of a real part ϵ' , and an imaginary part ϵ'' .

The wave equation for $\tilde{\mathbf{E}}$ is derived by taking the curl of both sides of Eq. (3.2), and substituting Eq. (3.4) into Eq. (3.6).

$$\nabla \times (\nabla \times \tilde{\mathbf{E}}) = -j\omega\mu(j\omega\epsilon_c\tilde{\mathbf{E}}) = \omega^2\mu\epsilon_c\tilde{\mathbf{E}} \quad (3.6)$$

The homogeneous wave equation for $\tilde{\mathbf{E}}$ is:

$$\nabla^2 \tilde{\mathbf{E}} - \gamma^2 \tilde{\mathbf{E}} = 0 \quad (3.7)$$

where ∇^2 is Laplacian operator, and γ is the propagation constant

$$\gamma^2 = -\omega^2 \mu \epsilon_c \quad (3.8)$$

3.1.1. PLANE-WAVE PROPAGATION IN LOSSLESS MEDIA

For a lossless medium (nonconducting) conductivity is equal to zero ($\sigma=0$), and consequently imaginary part is equal to zero ($\epsilon'' = 0$). The wave does not suffer any attenuation as it travels. The propagation constant becomes:

$$\gamma^2 = -\omega^2 \mu \epsilon \quad (3.9)$$

For a lossless media, the wave equations can be written with wavenumber k instead of the propagation constant:

$$k = -\omega \sqrt{\mu \epsilon} \quad (3.10)$$

Then Eq. (3.7) becomes:

$$\nabla^2 \tilde{\mathbf{E}} + k^2 \tilde{\mathbf{E}} = 0 \quad (3.11)$$

For an electric field phasor oriented in $\hat{\mathbf{x}}$ direction (defined in Cartesian coordinates), the Eq. (3.11) is reduced to:

$$\frac{d^2 \tilde{E}_x}{dz^2} + k^2 \tilde{E}_x = 0 \quad (3.12)$$

This is an example of a uniform plane wave, where electric and magnetic fields have uniform properties at all points across an infinite $x - y$ plane, with no electric, and magnetic field along its direction of propagation.

The general solution of the ordinary differential equation, Eq. (3.12) is:

$$\tilde{E}_x(z) = \tilde{E}_x^+(z) + \tilde{E}_x^-(z) = \tilde{E}_{x0}^+(z) e^{-jkz} + \tilde{E}_{x0}^-(z) e^{jkz} \quad (3.13)$$

where $\tilde{E}_{x0}^+(z)$ and $\tilde{E}_{x0}^-(z)$ are constants, which have to be determined from boundary conditions. The first term containing negative exponential e^{-jkz} represents a wave with amplitude $\tilde{E}_{x0}^+(z)$ traveling in the $+z$ direction. In the same way the second term represents a wave traveling in the $-z$ direction.

3.1.2. PLANE-WAVE PROPAGATION IN LOSSY MEDIA

In case of the lossy media Eq. (3.14) can be expressed as:

$$\gamma^2 = -\omega^2 \mu \epsilon_c = -\omega^2 \mu (\epsilon' - j\epsilon'') \quad (3.14)$$

By separating the real and imaginary part γ can be written as:

$$\gamma = \alpha + j\beta \quad (3.15)$$

where α is the medium's attenuation constant and β is phase constant. The general solution for lossy media comprised of two waves, one traveling in the $+z$ direction and another traveling in the $-z$ direction is equal to:

$$\tilde{E}_x(z) = \tilde{E}_x^+(z) + \tilde{E}_x^-(z) = \tilde{E}_{x0}^+(z) e^{-\alpha z} e^{-j\beta z} + \tilde{E}_{x0}^-(z) e^{\alpha z} e^{j\beta z} \quad (3.16)$$

Maxwell's equations describing the propagating waves require that the spatial directions of $\tilde{\mathbf{E}}$, $\tilde{\mathbf{H}}$, and $\hat{\mathbf{k}}$ be perpendicular to each other. That results in directions of $\tilde{\mathbf{E}}$ and $\tilde{\mathbf{H}}$ perpendicular to the direction of propagation. In free space (lossless media) $\tilde{\mathbf{E}}$ and $\tilde{\mathbf{H}}$ are in phase, where each peaks at the same time. If the wave propagates inside a lossy media, the electric and magnetic field are not necessary in the phase, because η_c (intrinsic impedance) has a complex value. Also, if the energy storage inside the media occurs, the field does not have to be always perpendicular to each other. [32] For uniform plane wave traveling in an arbitrary direction, represented by the unit vector $\hat{\mathbf{k}}$, the electric and magnetic field phasors and are related as:

$$\tilde{\mathbf{H}} = \frac{1}{\eta_c} \hat{\mathbf{k}} \times \tilde{\mathbf{E}} \quad (3.17)$$

$$\tilde{\mathbf{E}} = -\eta_c \hat{\mathbf{k}} \times \tilde{\mathbf{H}} \quad (3.18)$$

where η_c is the intrinsic impedance of the lossy medium.

$$\eta_c = \sqrt{\frac{\mu}{\epsilon_c}} \quad (3.19)$$

COMPLEX REFRACTIVE INDEX

Mostly, the electromagnetic properties of materials are provided in form of the complex refractive index, defined as [33]:

$$\tilde{N} = n + jk \quad (3.20)$$

where n is the real part of the complex refractive index and k is absorption index (also called as extinction coefficient) related to attenuation constant, α by:

$$\alpha = \frac{4\pi k}{\lambda_0} \quad (3.21)$$

where λ_0 is the wavelength in the free space.

The complex electrical permittivity is then related to the complex refractive index by two expressions:

$$\epsilon' = n^2 - k^2 \quad (3.22)$$

$$\epsilon'' = 2nk \quad (3.23)$$

3.2. THE POLARIZATION OF LIGHT WAVES: JONES AND MULLER CALCULUS

Polarization is a property that is common to all types of vector waves. Polarization refers to the behaviour of one of the field vectors associated to that wave, observed at a fixed point in space. Light waves are electromagnetic in nature and require four basic field vectors for their complete description: the electric-field strength \mathbf{E} , the electric-displacement density \mathbf{D} , the magnetic-field strength \mathbf{H} and the magnetic-flux density \mathbf{B} . Of these four vectors the electric-field strength \mathbf{E} is chosen to define the state of polarization of light waves. This section serves as an overview of relevant mathematical relations that are used to describe polarized light. Furthermore, the mathematical relations are used to discuss the interaction between polarized light and optical components that compose a polarizing optical system (in this case spectro-polarimeter). Also, the analytic expressions for important ideal polarizing optical components are discussed which are later used to estimate the performance of designed (simulated) optical system. The theory of the polarization of light waves is based on [17].

A light wave is called poly-chromatic if multiple spectrum frequencies are present. On the other side, if only single discrete frequency is present of zero spectral width, a light wave is monochromatic. Between the two cases is the quasi-chromatic wave, which is described by a narrow spectral line of very small but not zero width. For a monochromatic wave, the time variation of the electric vector \mathbf{E} is exactly sinusoidal. At a fixed point in space, the most general oscillation of the electric vector \mathbf{E} can be resolved into three independent, linear, simple-harmonic oscillation E_x , E_y and E_z . Along three mutually orthogonal directions x , y and z , respectively.

$$\mathbf{E} = E_x \hat{\mathbf{x}} + E_y \hat{\mathbf{y}} + E_z \hat{\mathbf{z}} \quad (3.24)$$

$$E_i = \tilde{E}_i \cos(\omega t + \delta_i), \quad i = x, y, z. \quad (3.25)$$

where $\hat{\mathbf{x}}$, $\hat{\mathbf{y}}$ and $\hat{\mathbf{z}}$ are unit vectors along the coordinate axes; \tilde{E}_i and δ_i represent the amplitude and phase, respectively, of the linear oscillation along the i th coordinate axis and ω represents the angular frequency.

The relation between angular frequency and frequency is:

$$f = \frac{\omega}{2\pi} \quad (3.26)$$

Same as in Eq. 3.24, the electric vector \mathbf{E} in phasor representation is then written as:

$$\mathbf{E}_c = E_{xc} \hat{\mathbf{x}} + E_{yc} \hat{\mathbf{y}} + E_{zc} \hat{\mathbf{z}} \quad (3.27)$$

Eq. 3.27 defines a complex vector which completely specifies the state of polarization of the field. For simplicity, the subscript c, to distinguish a phasor is dropped in later expressions.

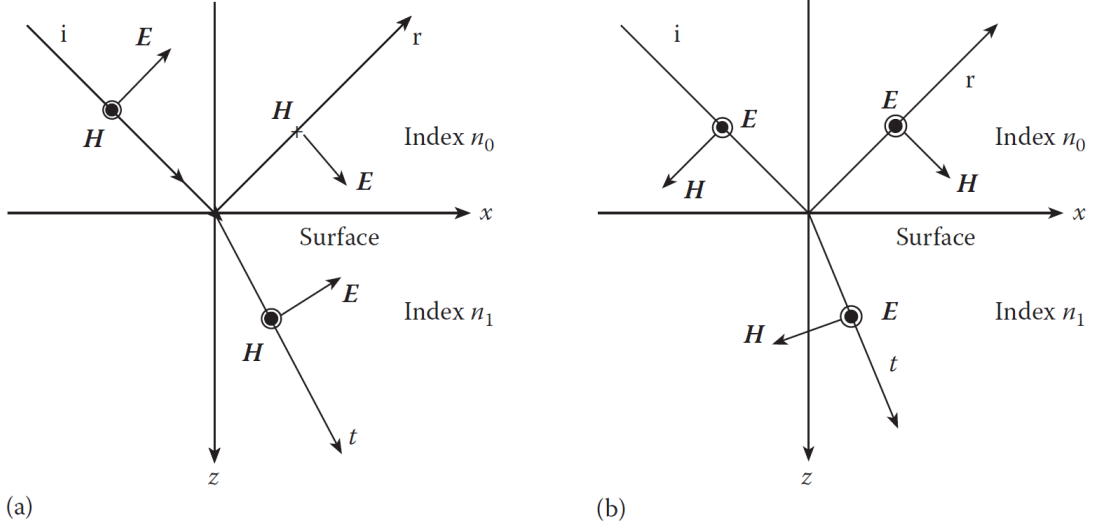


Figure 3.1: (a) Definition of the positive directions of the electric and magnetic vectors for TM waves. (b) Definition of the positive directions of the electric and magnetic vectors for TE waves. [3]

Eq. 3.27 is the general case where light wave has an arbitrary spatial structure. A special case of great interest is that of a uniform TE (transverse-electric) traveling plane wave. The definition of TE and TM (transverse-magnetic) modes are described in Fig. 3.1. The electric vector of a linearly polarized wave of this type varies with position \mathbf{r} and time t according to:

$$\mathbf{E}(\mathbf{r}, t) = [\tilde{E}_i \cos(\omega t - \mathbf{k} \cdot \mathbf{r})] \hat{\mathbf{u}}, \quad \hat{\mathbf{u}} \cdot \hat{\mathbf{u}} = 1, \hat{\mathbf{u}} \cdot \mathbf{k} = 0 \quad (3.28)$$

where $\hat{\mathbf{u}}$ represents a constant unit vector in the direction of the linear polarization, transverse to the direction of wave propagation given by the constant wave-vector \mathbf{k} . \tilde{E} is the amplitude of oscillation which is independent of \mathbf{r} and t . A set of points in space at which the electric field oscillates in phase ($\mathbf{k} \cdot \mathbf{r} = \text{const.}$) makes a sequence of parallel plane wave-fronts perpendicular to the wave-vector \mathbf{k} . The distance that separates two adjacent constant-phase planes of phases separated by 2π defines the wavelength λ which is related to \mathbf{k} by:

$$|\mathbf{k}| = \frac{2\pi}{\lambda} \quad (3.29)$$

The phase velocity of the wave is defined as the velocity of a point in space along the direction of propagation, where the instantaneous magnitude of the field at that point remains constant. If s denotes distance measured along the direction of \mathbf{k} (from the fixed origin), the argument of the cosine function in Eq. 3.28 (the total phase) can be written as $[\omega t - (2\pi/\lambda)s]$. The condition of constant instantaneous magnitude of the field requires that s varies with t such that $[\omega t - (2\pi/\lambda)s]$ is constant.

$$\frac{d}{dt} \left(\omega t - \frac{2\pi}{\lambda} s \right) = 0 \quad (3.30)$$

which gives the phase velocity v as

$$v = \frac{ds}{dt} = \frac{\omega \lambda}{2\pi} = f \lambda \quad (3.31)$$

where f is the frequency of the monochromatic light.

3.2.1. JONES MATRIX

The electric field vector of a single monochromatic, uniform TE plane wave with an arbitrary polarization, propagating in z direction is given by:

$$\mathbf{E}(z, t) = \left[\tilde{E}_x \cos \left(\omega t - \frac{2\pi}{\lambda} z + \delta_x \right) \right] \hat{\mathbf{x}} + \left[\tilde{E}_y \cos \left(\omega t - \frac{2\pi}{\lambda} z + \delta_y \right) \right] \hat{\mathbf{y}} \quad (3.32)$$

where \tilde{E}_x and \tilde{E}_y represent the amplitudes of the electric field components along the x and y axes, and δ_x and δ_y represent the respective phases of these fields. $\hat{\mathbf{x}}$ and $\hat{\mathbf{y}}$ are unit vectors in the positive direction of the x and y axes. In this case the wave is uniform plane wave, with same values of the electric field in a $z = \text{const.}$ plane. Also, it is transverse-electric (TE), without field component along the direction of propagation, $\mathbf{k} = (2\pi/\lambda)\hat{\mathbf{z}}$.

Eq. (3.32) describes the electric field as function of location in direction and time, t . The more concise mathematical description for the wave (Eq. (3.32)) is used in the form of a 2x1 column vector, in the phasor notation:

$$\mathbf{E}(z) = e^{-j2\pi z/\lambda} \begin{bmatrix} \tilde{E}_x e^{j\delta_x} \\ \tilde{E}_y e^{j\delta_y} \end{bmatrix} \quad (3.33)$$

The temporal information is suppressed, because the field components at all points in space for a monochromatic field are known to oscillate sinusoidally with time at the same frequency.

The final reduction of the expression is done by dropping the spatial information about the wave. Considering only the field over one fixed transverse plane, for example, the plane $z = 0$ the expression becomes:

$$\mathbf{E}(0) = \begin{bmatrix} \tilde{E}_x e^{j\delta_x} \\ \tilde{E}_y e^{j\delta_y} \end{bmatrix} \quad (3.34)$$

The vector $\mathbf{E}(0)$ of Eq. (3.34) is concise representation of a single plane wave which is known to be monochromatic, uniform, and transverse-electric. This vector is called the Jones vector of the wave. The Jones vector, in form of complex numbers, contains complete information about the amplitudes and phases of the field components, hence about the polarization of the wave. These two phasors represent two sinusoidal linear oscillations along two mutually perpendicular direction in the wavefront. One Jones vector is adequate for the reconstruction of the entire plane wave.

Final simplified notation for the Jones vector is:

$$\mathbf{E} = \begin{bmatrix} E_x \\ E_y \end{bmatrix} \quad (3.35)$$

where

$$E_x = |E_x| e^{j\delta_x}, \quad E_y = |E_y| e^{j\delta_y} \quad (3.36)$$

Wave intensity, I is the sum of the squared amplitudes of the component oscillations along two mutually orthogonal directions:

$$I = |E_x|^2 + |E_y|^2 = E_x^* E_x + E_y^* E_y \quad (3.37)$$

where superscript $*$ represents complex conjugate.

In practical applications, a beam of polarized light is propagating through a succession of optical devices each of which producing a specific change in the state of polarization. These devices are classified as polarizing optical system. Some of the examples are polarizers, retarders and polarization beam splitters.

Considering a uniform monochromatic TE plane wave incident on a non-depolarizing optical system (in z axis direction) that consists of either a single or series of multiple optical devices, the interaction between the incident wave and the optical system results in one or more modified plane waves emerging from the system. The incident and the outgoing plane waves can be fully described by Jones vectors \mathbf{E}_i and \mathbf{E}_o , respectively. The input Jones vector consisting for phasor components E_{ix} and E_{iy} represent the projection of the incident electric field of light wave onto the Cartesian coordinate system along the transverse x and y coordinate

axes, respectively. The values of the outgoing components E_{ox} and E_{oy} of the Jones vector at the output of the optical system are related to the pair of oscillations of input components E_{ix} and E_{iy} by two linear equations:

$$E_{0x} = T_{11}E_{ix} + T_{12}E_{iy} \quad (3.38)$$

$$E_{0y} = T_{21}E_{ix} + T_{22}E_{iy} \quad (3.39)$$

Equations can be combined in matrix form:

$$\begin{bmatrix} E_{0x} \\ E_{0y} \end{bmatrix} = \begin{bmatrix} T_{11} & T_{12} \\ T_{21} & T_{22} \end{bmatrix} \begin{bmatrix} E_{ix} \\ E_{iy} \end{bmatrix} \quad (3.40)$$

$$\mathbf{E}_0 = \mathbf{T} \mathbf{E}_i \quad (3.41)$$

where

$$\mathbf{T} = \begin{bmatrix} T_{11} & T_{12} \\ T_{21} & T_{22} \end{bmatrix} \equiv \begin{bmatrix} T_{xx} & T_{xy} \\ T_{yx} & T_{yy} \end{bmatrix} \quad (3.42)$$

Equation (3.41) expresses the law of interaction between the incident wave and the optical system as a simple linear matrix transformation of the Jones vector. This expression is the fundamental relation that is used in this research to convey the results of the simulations. The 2x2 transformation matrix, \mathbf{T} is called the Jones matrix of the optical system or optical device (Eq. (3.42)) and its elements T_{ij} are in general complex. The main parameters that affect the value of Jones matrix are:

- The optical system under consideration;
- The frequency of the incident wave;
- The orientation of the system with respect to the incident wave plane;
- The azimuthal orientation of the input transverse coordinate axes (x, y).

The Jones matrix describes the overall effect of the optical system illuminated by the incident wave. The diagonal elements T_{11} and T_{22} of the Jones matrix of the optical system are determined by input-to-output mappings of linear polarizations, whereas the off-diagonal elements T_{21} and T_{12} are determined by the input-to-output mappings of crossed linear polarizations, respectively.

The combined effect of multiple separate optical systems placed in the path of a plane wave of light can be written as a cascade of N optical systems, therefore a chain of N Jones matrices, which correspond to combined optical system:

$$\mathbf{E}_0 = \mathbf{T}_N \mathbf{T}_{N-1} \dots \mathbf{T}_II \mathbf{T}_I \mathbf{E}_i \quad (3.43)$$

Furthermore, the law by which the Jones matrix transforms $\mathbf{T} \rightarrow \mathbf{T}'$ under effect of a coordinate rotation $x, y \rightarrow x', y'$ is:

$$\mathbf{T}' = \mathbf{R}(\alpha) \mathbf{T} \mathbf{R}^*(\alpha) \quad (3.44)$$

where \mathbf{R} is the 2x2 rotation matrix.

$$\mathbf{R}(\alpha) = \begin{bmatrix} \cos(\alpha) & \sin(\alpha) \\ -\sin(\alpha) & \cos(\alpha) \end{bmatrix} \quad (3.45)$$

where α is a counter-clockwise rotation of an angle about z axis.

3.2.2. MULLER MATRIX

Another representation of the states of polarization of a quasi-monochromatic (or monochromatic) TE plane wave of light can be expressed by a set of four real quantities, called the Stokes parameters, each of which has the dimensions of intensity. Stokes parameters are denoted by S_0, S_1, S_2, S_3 , and defined as follows:

$$S_0 = \langle \tilde{E}_x^2(t) \rangle + \langle \tilde{E}_y^2(t) \rangle \quad (3.46)$$

$$S_1 = \langle \tilde{E}_x^2(t) \rangle - \langle \tilde{E}_y^2(t) \rangle \quad (3.47)$$

$$S_2 = 2 \langle \tilde{E}_x^2(t) \tilde{E}_y^2(t) \cos[\delta_y(t) - \delta_x(t)] \rangle \quad (3.48)$$

$$S_3 = 2 \langle \tilde{E}_x^2(t) \tilde{E}_y^2(t) \sin[\delta_y(t) - \delta_x(t)] \rangle \quad (3.49)$$

where $\langle v \rangle$ signifies the time average of v , over an interval of time, T , which is long enough to make the time-average integral independent of T itself.

$$\langle v \rangle = \frac{1}{T} \int_0^T v dt \quad (3.50)$$

First Stokes parameter, S_0 represents the total intensity of the light wave. S_1 represents the difference between the intensities of the x and y components and can be either positive, negative, or zero depending on whether the wave has stronger preference to the x linear polarization, to the y linear polarization, or to neither one of these two states, respectively. S_2 represents the preference of the wave to either the $+\frac{1}{4}\pi$ or the $-\frac{1}{4}\pi$ linearly polarized component. S_3 represents the preference of the wave to either the right-handed or to the left-handed circularly polarized component. S_3 is positive, negative or zero dependent on the wave possessing stronger preference to the right-circular state, the left-circular state or to neither one of these two states, respectively. Stokes parameters can be written in terms of intensities, where I_x , I_y , $I_{+\frac{1}{4}\pi}$, $I_{-\frac{1}{4}\pi}$, I_l , and I_r represent the intensities transmitted by an ideal variable polarizer placed in the path of the wave and adjusted to transmit the x , y , $+\frac{1}{4}\pi$, $-\frac{1}{4}\pi$, linear polarizations and the left (l) and right (r) circular polarizations, respectively.

$$S_0 = I_x + I_y \quad (3.51)$$

$$S_1 = I_x - I_y \quad (3.52)$$

$$S_2 = I_{+\frac{1}{4}\pi} - I_{-\frac{1}{4}\pi} \quad (3.53)$$

$$S_3 = I_r - I_l \quad (3.54)$$

The Stokes parameters of a quasi-monochromatic light wave can be grouped in a 4x1 column vector, called Stokes vector:

$$\mathbf{S} = \begin{bmatrix} S_0 \\ S_1 \\ S_2 \\ S_3 \end{bmatrix} \quad (3.55)$$

The Stokes parameters of a totally polarized wave satisfy the following condition:

$$S_0^2 = S_1^2 + S_2^2 + S_3^2 \quad (3.56)$$

An important quantity in the description of partially polarized light is the degree of polarization, p which is defined as the ratio of the intensity of the totally polarized component to the total intensity of the wave:

$$p = \frac{\sqrt{S_1^2 + S_2^2 + S_3^2}}{S_0} \quad (3.57)$$

The degree of polarization varies from zero for unpolarized light to unity in the case totally polarized light.

The azimuth θ and ellipticity angle ϵ of the ellipse of polarization of the totally polarized component can be written as function of Stokes parameters as:

$$\theta = \frac{1}{2} \operatorname{atan} \left(\frac{S_2}{S_1} \right), \quad \epsilon = \frac{1}{2} \operatorname{asin} \left[\frac{S_3}{\sqrt{S_1^2 + S_2^2 + S_3^2}} \right] \quad (3.58)$$

The partially polarized quasi-monochromatic light propagating thorough a depolarizing optical system that decreases the degree of polarization of the transmitted light can not be expressed with Jones formalism. The reason is that a deterministic 2x2 complex Jones matrix can no longer be used to express the depolarizing incoherent interaction between the incident wave and the optical system. For that reason Muller matrix formulation is introduced. It is based on the representation of the state of polarization of the light wave by a Stokes vector and the representation of the depolarizing optical system by a 4x4 Mueller matrix, all of whose elements are real.

When a light wave is sequentially processed by a cascade of N optical devices, the over-all combined effect is described by a combined Muller matrix:

$$\mathbf{M}_{\text{comb}} = \mathbf{M}_N \mathbf{M}_{N-1} \dots \mathbf{M}_I \mathbf{M}_I \quad (3.59)$$

where \mathbf{M}_k is the Mueller matrix of the k th optical device to operate on the wave and the order in which the devices are encountered by the wave is from I to N .

In similar way as in Jones matrix formulation, the Stokes vector \mathbf{S}_{out} of the wave outgoing from the optical system is obtained by pre-multiplying the Stokes vector \mathbf{S}_{in} of the incident wave by the Mueller matrix of the optical system. From the computed Stokes vector \mathbf{S}_{out} , it is possible to calculate the properties of the outgoing wave as its total intensity, degree of polarization and polarization form.

$$\mathbf{S}_{\text{out}} = \mathbf{M} \mathbf{S}_{\text{in}} \quad (3.60)$$

Eq. (3.60) can be calculated from Jones matrix by expression:

$$\mathbf{S}_{\text{out}} = [\mathbf{A}(\mathbf{T} \otimes \mathbf{T}^*) \mathbf{A}^{-1}] \mathbf{S}_{\text{in}} \quad (3.61)$$

where Muller matrix, \mathbf{M} is equal to:

$$\mathbf{M} = \mathbf{A} (\mathbf{T} \otimes \mathbf{T}^*) \mathbf{A}^{-1} \quad (3.62)$$

\mathbf{A} is the transformation matrix between Jones and Muller matrix, and \otimes is the tensor (Kronecker) product.

$$\mathbf{A} = \begin{bmatrix} 1 & 0 & 0 & 1 \\ 1 & 0 & 0 & -1 \\ 0 & 1 & 1 & 0 \\ 0 & -j & j & 0 \end{bmatrix} \quad (3.63)$$

3.3. METASURFACES

Metamaterials are artificially created composite materials consisted of a set of scatterers in a regular array in three-dimensional space, designed in such way to modify the incident electromagnetic wave in transmission or reflection. Generally, the size of the scatterers and periodicity of the array is closely related to the wavelengths of incident wave. The main purpose of developing such materials is to achieve some properties that are not found in natural homogeneous materials. For instance, there are many demonstration of developing metamaterials with properties like negative refractive index, near-zero index, etc. [24] The progress of metamaterials is very rapid. Over a short period of time, the research of metamaterials had progressed from a theoretical concept to realized physical devices in just a few decades. The metamaterials can be considered as three-dimensional structures, which modifies the EM waves in a similar way as natural materials, by propagation through them. The cumulative effect of such structure makes them necessary a thick optical device, since the effect of modification of EM waves depend on the propagation path through the material. There is a class of metamaterials, called the metasurfaces, where the scatterers are arranged into a two-dimensional pattern. In this case, the modification of EM waves is achieved by shaping the cross-section of the scatterers, while their height is kept the same. Such structures are providing an abrupt change of amplitude, phase and polarization of the impinging EM waves. The advantage of the metasurfaces is reduction in physical space, with respect to three-dimensional metamaterials. [24] The interesting type of the metasurfaces are the dielectric metasurfaces. Firstly due to its compatibility to CMOS detector technology, which allows integration of a thin layer of a metasurface directly on the detector array, and secondly high transmission (depending on the material, and wavelength) of the dielectric materials. The dielectric metasurfaces has advantage over plasmonic-based metasurfaces, which are characterized by higher losses. The period and size of the scatterers is smaller than wavelength. Therefore, the complete control of EM waves can be achieved: amplitude, phase, and polarization at subwavelength resolution. This is convenient because diffraction is not present at that scale. That enables to design optical devices like lenses, waveplates, polarizing beam splitters with similar performances as current technology, but with extreme reduction in thickness. Fig. 3.2 shows an example of fabricated metasurface lens consisted of an array of cylinders. In conventional lenses, the phase distribution over the lens is achieved by the accumulation of phase delay of the incident light, when propagating through different thicknesses of the lens. The thicker part of the lens will introduce more phase delay than a thinner part of the lens. The metasurface lens utilizes different principle, where the outgoing phase

is tuned by proper shaping of cylinder's diameter of local scatterers, while the thickness of the lens is same (Fig. 3.2). The fact that the phase control is achieved with only the transverse dimensions of the scatterers is advantageous because the realization of the structures requires only one lithographic step. Diffractive optics elements require multiple steps, since the phase sampling is given by different thicknesses of layers. The

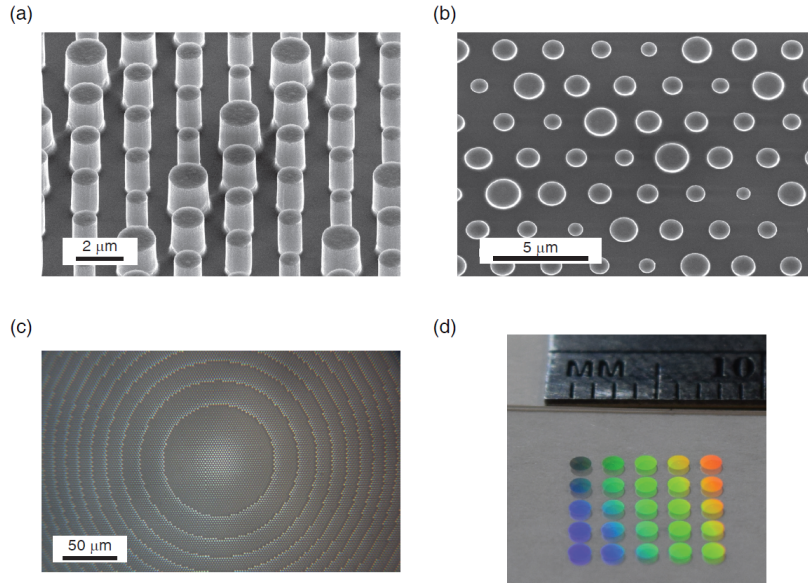


Figure 3.2: An example of metasurface lens. (a) Scanning electron micrograph showing tilted and (b) top views of a fabricated metasurface lens. (c) Optical microscope image of the center part of a metasurface lens. (d) A 5x5 array of metasurface lenses. [4]

response of EM waves propagating through a periodic composite material is not the same for different frequency (wavelength) ranges, or at different length scales of structures. The behavior of a composite material can be classified into three distinguishable regions with respect to the EM wave's wavelength (λ) inside the composite material. The parameters like the effective size of the scatterer ($D_{eff} = D/n$, depending on size and the refractive index of the scatterer), and period of the array (a) have an important role how the EM wave behave propagating through the composite material [24]. Three distinct regions can be identified:

1. No resonances ($\lambda \gg a$)
2. Resonances associated with the individual scatterers ($\lambda \sim D_{eff}$)
3. Resonances associated with the lattice periodicity of the scatterers ($\lambda \sim a$)

In *Region 1*, low frequencies are present, where the wavelength is much larger than the period of the array. To obtain equivalent effective-material properties (permittivity, and permeability), the classical mixing formulas are used. In *Region 3*, the wavelengths are comparable to the period of the array, where more complicated field behavior exist, which can not be treated as effective medium. In this region, the resonances associated with the lattice periodicity occurs, which can be described by Floquet-Bloch theory. The metasurface is an array of scatterers that falls into *Region 2*. The resonances of the surfaces are associated with the resonances of the individual scatterers, but not with the periodicity of the array. If the individual scatterers are designed in proper way, with certain combination of shape and material, the resonance inside the scatterer occurs. [24] The theory behind dielectric metasurfaces, where the resonances occur in individual scatterers can be traced back to Mie scattering of a homogenous dielectric sphere, for which an analytic solution to Maxwell's equations exists. This is further discussed in Subsection 3.3.3. There is a specific type of a metasurface, called high-contrast metasurface. The property of such surfaces is high contrast in refractive index between scatterer and the surrounding medium ($\Delta n > 1$). [5] This planar optical components received considerable interest in the field of integrated optics due to unique optical properties. The fabrication of this patterned structure is done by the very well developed method of lithography. A general shape of these patterned scatterers is an elliptic cylinder, which can provide full manipulation of light (amplitude, phase, polarization)

only by shaping the major/minor axis (diameters) and orientation of the ellipse. [34] Therefore, dielectric high-contrast metasurfaces are chosen as main focus in this research. The alternative to the array of elliptic cylinders is sub-wavelength grating, which allows a larger aspect ratio, and therefore larger anisotropy for two orthogonal directions. This is suitable for materials with lower refractive index since the strength of resonance is proportional to the refractive index of the material.

The important parameters of the dielectric metasurfaces consisted of an array of cylindrical resonators are:

- period of the array, a
- effective diameter of the cylinder, $D_{eff} = D/n$
- height of the cylinder, h

Each of these parameters is further explained in the following subsections.

3.3.1. PERIOD OF THE ARRAY

In order to explain how the period of the array affect the properties of a metasurface, an example of one-dimensional grating is provided. In Fig. 3.3 is depicted simple one-dimensional rectangular grating, with period, a in the direction of the x axis, while its length is extending to infinity in the direction of the y axis. The monochromatic plane wave with the wavelength of λ is normally impinging on the grating from the $-z$ towards the $+z$ direction. The refractive index of the surrounding medium is defined by n_s . The grating equation can be expressed as [5]:

$$\sin(\theta_m) = \sin(\theta_0) + \frac{m\lambda}{an_s} \quad (3.64)$$

where θ_m is the angle of the m -th order (m is an integer) and θ_0 is the incident angle. For normally impinging

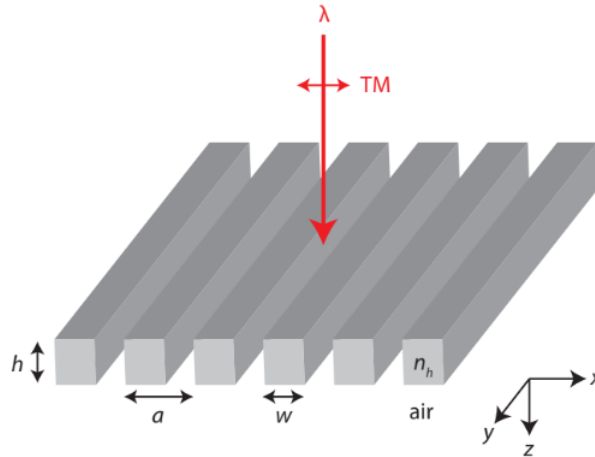


Figure 3.3: Generic 1-D grating problem with a periodicity of a , where the light is normally incident, the surrounding medium is air ($n = 1$), the refractive index of the grating is n_h , and w is the width of the grating. [5]

incident plane wave ($\theta_0 = 0$), with a period, a larger than wavelength, λ the incident plane wave is splitted and diffracted into several beams traveling in the different direction (corresponding to different orders, m). In this case, the grating acts as a diffraction grating, used in optics as the dispersive element for applications like spectrometers.

If the period (a) is smaller than the wavelength (λ), the right-hand side of Eq. (3.64) reaches values greater than one. In this case, the possible solution for θ_m can only be imaginary number (for nonzero integer value for m). The properties of such grating correspond to a guided Bloch mode, instead of transmission free-space mode that occurs when the period is greater than the wavelength. [5] The Bloch mode occurs when a

periodically repeating refractive index of medium is present, with a period similar to the incident wavelength.

By setting the following condition: $\sin(\theta_0) + \frac{m\lambda}{an_s} > 1$, it is possible to estimate required period, a to suppress the diffraction of the light. In addition, the value of incident angle equal to $\theta_0 = -90$ deg, ensures that even an impinging wave with incident angle parallel to the grating will not produce any diffraction.

$$a < \frac{m\lambda}{2n_s} \approx \frac{\lambda}{2} \quad (3.65)$$

Eq. (3.65) represents the condition used to design the period of the array for an operational wavelength. By considering only positive mode order, $m = 1$ and surrounding medium air, $n_s = 1$, the period of the array should be smaller than half of the wavelength ($\lambda/2$).

3.3.2. DIAMETER OF THE RESONATORS

As shown in the previous subsection 3.3.1, on an example of one-dimensional grating (Fig. 3.3), the period of an array has important role on the behaviour of the incident plane wave. Another parameter that has the influence on the behaviour is the width of the grating, w . If only a single propagating Bloch mode along the grating is present, the effective medium theory (EMT) is used as an approximation for understanding this periodic structures. The type of regime for the grating occurs when the width is less than $w < \lambda/(2n_h)$. When this condition holds, the grating can be considered as a homogeneous slab with an anisotropic effective refractive index (deep-subwavelength regime). [5] That allows to make an artificial anisotropic material, which has properties as a birefringent crystal. The properties of the high-contrast metasurfaces can be classified in regime in between diffraction grating and EMT. In this regime subwavelength periodic structure supports more than one propagative Bloch mode (multimode regime). [5]

In sum, three regimes of one-dimensional grating are:

- diffraction grating regime ($\lambda < a$)
- "multimode" regime, in which a few propagative Bloch modes can exist
- EMT regime, in which the grating behaves as a homogeneous slab with an effective index ($w < \lambda/(2n_h)$)

MIE SCATTERING

Looking from a different point of view, the interpretation of metasurfaces can be traced back to the Mie scattering of dielectric spheres. As already mentioned in Section 3.3 (referring to *Region 2*), the resonance associated to individual scatterers, can be explained by the Mie theory, where the geometrical resonances occurs in dielectric nanoparticles. If the size of the scatterers and the period of an array is design in proper way, the coupling between neighboring scatterers is weak. Therefore, the complete behaviour of the metasurface can be interpreted as scattering from individual nanoparticles arranged in the array, since the distance between neighboring nanoparticles is large enough that their interaction is very weak. [6] A sub-wavelength high-index dielectric nanoparticle induces electric and magnetic dipole resonances with comparable strengths when illuminated by a plane wave. [6] The resonant magnetic behavior is result of a coupling of incoming plane wave to the circular displacement currents of the electric field. This magnetic resonance is induced if the wavelength inside the nanoparticle is comparable to its diameter $D = \lambda/n$. (λ is the wavelength of the plane wave, and n is refractive index). [6] When the electric and magnetic resonances spectrally overlap, the backward scattering is not present, leading to unidirectional scattering and Huygens metasurfaces.

In the dielectric sphere, the scattering properties are governed by two parameters: the dielectric permittivity ϵ and a size parameter q defined as $q = 2\pi R/\lambda$ (R is the radius of the sphere). The required index of refraction to achieve well defined resonances of main multipoles is $n > 2$. The nanospheres made of silicon (Si) with with diameter from 100 to 300 nm have strong magnetic and electric dipole resonances in the visible and near-IR spectrum. [6] Regarding the fabrication of metasurfaces, it is important to notice that like in the sphere, the resonances in other geometrical shapes, for instance, in cylinders are also possible. [7] Therefore, it is much easier to fabricate, an array of cylindrical nanostructures than an array of nano-spheres. Adjusting the diameter of the cylinder, it is possible to spectrally position the electric and magnetic dipole resonances. It is shown that by increasing the diameter of the cylinder, while keeping the same height, the red-shift is stronger for the electric dipole, than for magnetic dipole. For low aspect ratios of a cylinder, the MD mode can be positioned at a lower wavelength than the ED mode. [7]

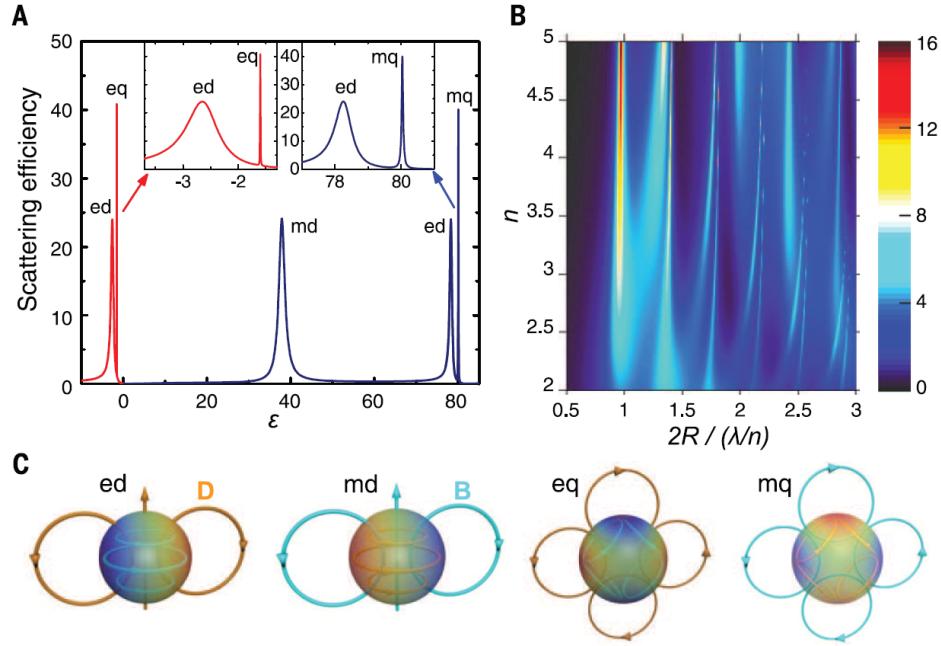


Figure 3.4: Mie resonances of a spherical particle. (A) Scattering efficiency (dimensionless ratio of scattering cross section to geometrical cross section of the particle) versus dielectric permittivity ϵ (lossless particle, $q = 0.5$) for plasmonic ($\epsilon < 0$) and dielectric ($\epsilon > 0$) materials. Abbreviations for resonances: ed, electric dipole; eq, electric quadrupole; md, magnetic dipole; mq, magnetic quadrupole. Higher-order multipole modes are not shown for the sake of simplicity. (B) Scattering efficiency of a lossless dielectric particle (color scale at right) as a function of refractive index n and size parameter. (C) Illustration of electric and magnetic field structures for different electric and magnetic resonances supported by a spherical dielectric particle. [6]

3.3.3. HEIGHT OF THE RESONATORS

In [7] is conducted a systematic study how the influence of nano-particle geometry and environment of the dielectric resonators in visible to the near-IR spectral range. There is a limit when no magnetic mode can be supported in the nano-particle. For cylindrical resonators, this occurs when the height of the cylinder is too short. Fig. 3.5 c), d), and e) illustrates the behavior of the electric field inside the cylinder (denoted by white dashed lines) for three different heights of the cylinder. The electric field shown inside is for the resonant wavelength, which is different for each height. The vertical crosscuts are parallel to the polarization of the electric field. The magnetic dipole is induced by the electric field of light that couples to vertically oriented displacement currents loops (indicated with gray electric field lines) in the cylinder. In order to form the displacement current loop, the phase shift (retardation) of the electric field in direction of cylinder height is required (where the electric field orientation in the top and the bottom part of the cylinder has opposite direction). [7]

The electric dipole does not require retardation inside the cylinder. Because $\mu = 1$ for cylinder and air, the induced magnetic current loop by dipole moment is extended outside the cylinder. [7] When a material contains polar molecules (dielectric material), the orientation inside material is generally randomly oriented. In presence of electric field, the material is polarized by orienting the dipole moments of polar molecules in direction of the electric field. Therefore, the electric dipole resonance inside the cylinder is established by collective polarization of the material inside the resonator by the electric field component of the incident light. The resulting electric dipole moment is oriented perpendicular to the magnetic field polarization.

Fig. 3.5 a) shows the normalized scattering cross section Q_{scat} as function of the wavelength for *Si* cylinder in air with height of $h = 100$ nm and diameter $d = 100$ nm for a normal incident plane wave. It can be noticed that magnetic and electric dipole does not overlap spectrally. By increasing the height of the cylinder, the MD and ED start to spectrally overlap 3.5 b). Also, it can be noticed the peaks are red-shifted, and scattering cross-section is increased. The increase in Q_{scat} is associated by increase in the volume of the cylinder

for the constant geometrical cross section. [7]

Furthermore, due to practical applications cylindrical resonators are placed on a substrate. If the substrate has a similar value of refractive index, the displacement current loop can be extended into the substrate. In this case, the resonance peaks are broader in the spectrum. However, if the refractive index of the substrate is small (for instance SiO_2), the influence of the substrate on the resonance is very weak. [7]

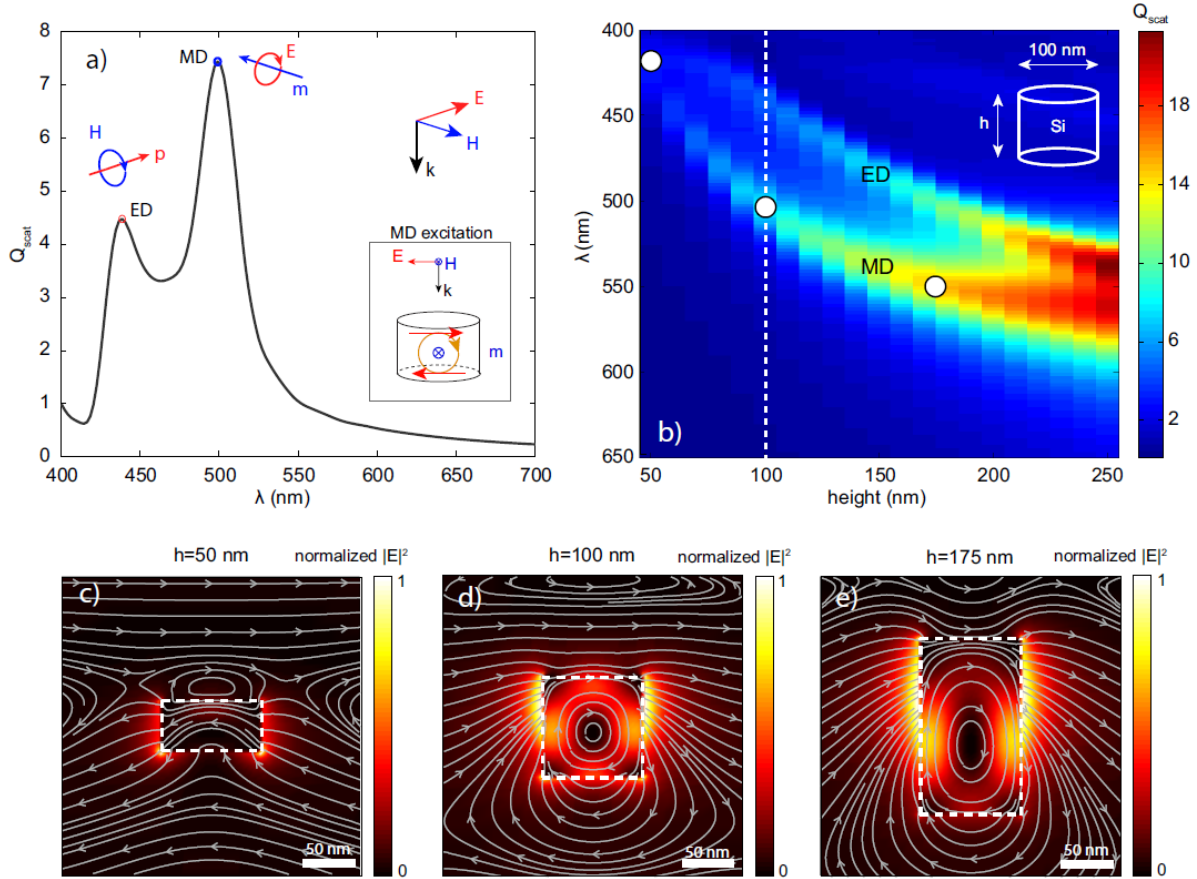


Figure 3.5: (a) Q_{scat} as a function of wavelength for a Si cylinder in air with $h = 100$ nm and $d = 100$ nm for optical excitation under normal incidence. The peaks correspond to the ED and MD mode, and the corresponding dipole moments and current loops are shown. The polarization of the driving field is shown in the top right. The inset shows the excitation mechanism of the MD mode. (b) Q_{scat} (color) as a function of λ and h for $h = 50$ -250 nm. The particle geometry is shown as an inset. The vertical white line is the crosscut corresponding to the spectrum shown in (a). The white dots correspond to the λ - h combinations used for (c-e). (c-e) Normalized electric field intensity $|E|^2$ (color) and electric field lines (gray) in vertical crosscuts through particles with $h = 50$ nm (c), $h = 100$ nm (d) and $h = 175$ nm (e), parallel to the electric driving field. [7]

3.4. SIMULATION METHODS OF THE METASURFACES

There are two conceptually different analytical approaches to describe the behavior of light in dielectric gratings (metasurfaces) [35]:

- Coupled-wave theory
- Floquet-Bloch (modal) theory.

In this research the Floquet-Bloch (FB) theory is applied simply due to the availability of commercial software tool HFSS (High Frequency Structure Simulator), which is a commercial finite element method solver for electromagnetic structures from Ansys. A FB wave is the simplest self-sufficient electromagnetic disturbance that can exist in the periodic medium.

3.4.1. SIMULATION METHODS

The wave equation that is solved by Ansoft HFSS is derived from the differential form of Maxwell's Equations. [31]

The type of excitation that is used in HFSS to model the periodic structures is the Floquet port. This type of excitation is used to simulate planar-periodic structures. The assumption is that structure is infinite array. The analysis is accomplished by analyzing a unit cell. The adjacent boundaries form the side walls of a unit cell, which represent a periodic boundary condition. Another boundary condition to account for the infinite space above and below the array is the Floquet port. The Floquet modes represents the fields on the port boundary, which are plane waves with propagation direction set by the frequency, phasing, and geometry of the periodic structure. In this research, the two main Floquet modes, two orthogonally-polarized plane waves propagating normal to the plane of the array are considered (denoted as TE_{00} , and TM_{00} mode), while higher-order modes are not taken into account. The higher-order modes are not used because the nanostructures are designed below the diffraction limit. All Floquet modes are interrelated by S-matrix, a 4x4 matrix, which interrelates the top and bottom Floquet port. The "FloquetPort 1 : 1" refers to the TE_{00} of the first port, and "FloquetPort 1 : 2" refers to the TM_{00} of the first port. In the same way the second port is denoted as "FloquetPort 2 : 1", and "FloquetPort 2 : 2", respectively. Therefore, the first number denotes the port number, and second the mode number, respectively. Since S-matrix contains all possible combinations of interrelated modes, including the transmission and the reflection coefficients, the Jones matrix shown in Eq. (3.42), which describes the transmission of the system from port 1 to port 2, is constructed by taking the following parameters from S-matrix:

$$\mathbf{T} = \begin{bmatrix} T_{xx} & T_{xy} \\ T_{yx} & T_{yy} \end{bmatrix} = \begin{bmatrix} \mathbf{S}(\text{FloquetPort 1 : 1}, \text{FloquetPort 2 : 1}) & \mathbf{S}(\text{FloquetPort 1 : 2}, \text{FloquetPort 2 : 1}) \\ \mathbf{S}(\text{FloquetPort 1 : 1}, \text{FloquetPort 2 : 2}) & \mathbf{S}(\text{FloquetPort 1 : 2}, \text{FloquetPort 2 : 2}) \end{bmatrix} \quad (3.66)$$

Fig. 3.6 (a) depicts an geometrical model of hexagonal lattice unit cell, representing elliptic cylinder placed on the substrate, where different colors represent different materials. Fig. 3.6 (b) and (c) shows the upper and bottom boundary condition (Floquet ports). Fig. 3.6 (d) shows the periodic boundary conditions on side walls of the unit cell (only one pair of side walls of the hexagonal lattice is shown due to clarity). The convergence condition in all simulations is adjusted in such a way that error in magnitude of S-matrix parameters is less than 0.5%.

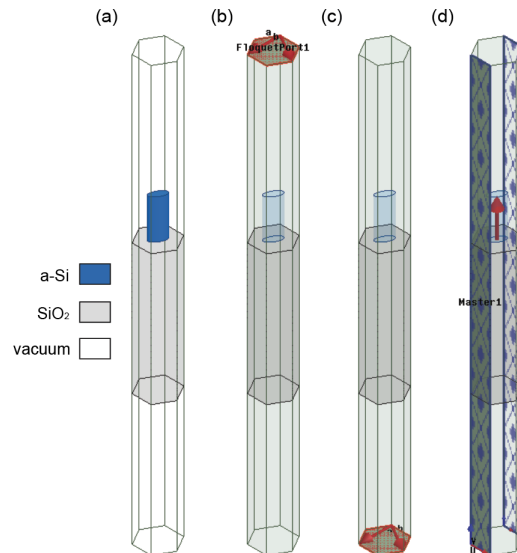


Figure 3.6: (a) An example of a simulated geometrical model of the unit cell representing birefringent dielectric metasurface with the hexagonal lattice. (b) Top Floquet port. (c) Bottom Floquet port. (d) The boundary condition of the side walls representing infinite array (only one pair is shown due to clarity)

4

DESIGN CONCEPTS

Since the main focus of the research are the metasurfaces, the purpose of this chapter is to select the most compatible spectropolarimetric technique for the metasurfaces. First, the common techniques are shown, with brief explanation of their differences, including some of the modern approaches. In the second section selected technique is presented. The main arguments of the selected technique are discussed. The detailed mathematical description and optimization of the selected technique is presented. Also, preliminary polarimetric accuracy for a shot noise limited ideal system is calculated. Then in the third section a metasurface design options are discussed. The selected type of metasurfaces and type of lattice of the geometrical model is shown. In the fourth and fifth section, two optical components of selected spectro-polarimeter are elaborated in detail: the dielectric metasurface as a micropatterned waveplate, and dielectric metasurface as micropatterned pleohroic Fabry-Pérot filter, respectively.

4.1. SPECTROPOLARIMETRIC TECHNIQUES

In this section an overview of spectropolarimetric techniques is presented. In optical polarimetry (ranging from the UV to IR), the Stokes formalism is adopted, where the state of polarization is described in terms of intensity. The reason for that lies in measurements technology. The detectors can measure only the total intensity (photon to electron conversion) at a single detector pixel. The common way to describe the measurement results is in terms of fractional polarization (by dividing the polarized Stokes parameters by the intensity).^[8]

Since the measured parameter at the detector pixel is intensity, the state of polarization (SOP) measurement requires some sort of modulation of the light. Therefore, the polarimetry involves the manipulation of light such that several independent intensity measurements can be combined to estimate the polarization state of the incident light. Usually, these intensity measurements are related to the state of the polarization by transformation matrix, which contains information of modulation (manipulation) of the light at each individual detector pixel. The goal of every polarimeter design is to ensure that these intensity measurements are arranged in the most optimal way. The reduction of error amplification after SOP reconstruction is the parameters which is optimized. There are many sources that introduce an error in the measured intensity, to mention a few: shot noise, detector read-out noise, error due to imperfect optical components. Three measurement domains are available for polarization measurements: the spatial domain, the temporal domain, and the spectral domain. ^[8] Each of these domain modulate the SOP in a different physical domain, but the principle does not change. There is always a trade-off between spatial, spectral and temporal parameters, since the increase in resolution of one parameter will inevitably decrease the resolution of other two parameters. The selection of the domain depend on the requirements of the spatial, spectral and temporal resolution.

It is important to note that different nomenclature for polarimetry exists depending on the community in which is used. In the remote sensing community different polarimetric techniques are categorized with labels: "division of ... ". In the astronomical community, each implementation that enables a polarization measurement is called "modulation": spatial, temporal, spectral modulation. ^[8] However, the nomenclature is not applicable to all polarimeters, as the new technology is emerging. The overview of different polarimet-

ric techniques in form of the Venn diagram can be seen in the Fig. 4.1.

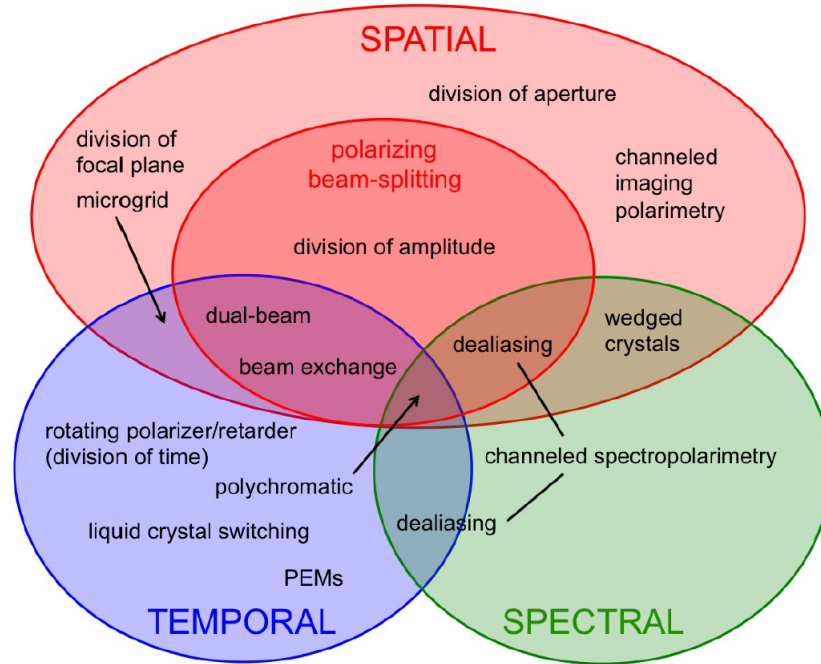


Figure 4.1: Venn diagram of polarization measurement/modulation domains [8]

The spatial domain offers several options that can measure complete Stokes vectors within a single snapshot [8]:

- **Division of focal plane (DoFP)** - In the division of focal plane, the polarimetric modulation can be implemented at the detector level. The microgrid polarizer arrays allow that different modulation of polarization is achieved at each detector pixel. The combination of intensity measurements of pixels yields instantaneous polarization data. The light is modulated locally at the image plane, usually consisted of four different pixels.
- **Division of aperture (DoA)** - In division of aperture method, the different modulation of polarization is placed to different parts of the aperture. The same image of an object is projected at different parts (by an additional optical component, for example, lens array) on the detector array, consisting of four identical images, where each part of the detector is modulated differently.
- **Division of amplitude (DoAM)** - The division of amplitude is the simplest method in terms of retrieving the Stokes parameters. The image of an object is divided into four beams by two polarizing beam-splitters, where each image is projected on the different detector array. The difference in intensity of those beams results in the first three Stokes parameters (S_0 , S_1 , and S_2).
- **Channeled imaging polarimetry (CIP)** - The channeled imaging polarimetry is based on diffraction optics, where the polarization is modulated in spatially distributed interference fringes, by a polarization grating. A polarization grating is an optical component that combines the functions of a hyper-efficient polarizer and a unique beam-splitter into a thin film.

From this can be deduced that the DoAM takes most of the volume (the most robust), the DoFP takes least of the volume (the most compact option), while the DoA and CIP are somewhere in the middle in terms of instrument volume.

The temporal modulation or division of time polarimeter designs involves sequential measurements. The

practical implementations include rotating polarizers (filter wheel) and rotating retarders in combination with a fixed polarizer. There are also some modern polarimeters with faster temporal modulation enabled by liquid crystal components: Liquid Crystal Variable Retarders (LCVRs) with fixed axes and electronically controllable retardance, or Ferroelectric Liquid Crystals (FLCs), which have a fixed retardance but a switchable axis orientation. The advantage of such components is that they do not physically rotate. Other fast temporal modulators include photo-elastic modulators (PEMs) and Pockels cells. [8] However, these types of polarimeters are not considered in this research, because the main focus is the implementation of metasurfaces.

The spectral modulation is a relatively recent technique, where the spectral domain is utilized for the polarization modulation (reference instrument SPEXone, already discussed in section 2.1).

4.1.1. MODERN POLARIZATION TECHNOLOGIES

In this subsection are listed two modern technologies that could enable development of a spectropolarimeter.

LIQUID CRYSTAL COMPONENTS

The Liquid Crystal Variable Retarders (LCVR) are very popular polarization modulator nowadays, although their development is still in progress. Moreover, technical solutions now exist for wide-field and achromatic LCVR. Active liquid crystal elements are space-qualified, and they are an available option for a polarimeters design on-board satellites. [8]

MICROPATTERNING (METASURFACES)

The micropatterning technology fabricated using state-of-the-art lithographic techniques allows to manipulate the light at the pixel level. This is usually achieved by integrating a thin layer on each pixel, which modifies the light propagating through it. Popular solutions are microgrid polarizer arrays. With advances in lithography, the write-grid structures can be fabricated at small scales, so that their applicability moves down to UV wavelengths. [8]

Micropolarizer arrays provide only linear polarization capability, and therefore the only measurement of linear polarization. For full-Stokes polarimeters, a micropatterned retarder in combination with a regular polarizer has been developed. [36] The combination of these two layers integrated on the top of a detector pixel allows complete modulation of polarization.

This type of technology is the subject of this research, and it is further discussed in Section 4.3.

4.2. SELECTED SPECTROPOLARIMETRIC TECHNIQUE

In this subsection, a trade-off of spectropolarimetric techniques is conducted. The temporal domain is regarded as an inappropriate option, since it is not convenient to have active elements on-board nano satellites with limited power source. Furthermore, a preliminary study showed that due to current limitation in fabrication of nanostructures, there is an uncertainty in controlling the spectrum, in case of metasurfaces. There is about a few nanometers spectral shift (deviation in discrete wavelength filtering) from the planned design (see Subsection 5.4.2 for more details). By discarding the temporal and spectral domain, in this preliminary trade-off, there is only spatial domain left as a possible choice.

The identified criteria for the trade-off are:

- Instrument volume
- Instrument complexity (number of optical components)
- Polarization accuracy
- Polarization aliasing

In Table 4.1, the trade-off for the most suitable spectropolarimetric technique for the metasurface is shown. Since the main goal of this research is the miniaturization of the spectropolarimeters, the weight of instrument volume criterion is the highest. Furthermore, instrument complexity criterion is regarded as the second most important because the reduction in a number of optical components makes an instrument more stable.

Table 4.1: The trade-off table for the most suitable spectropolarimetric technique for the metasurfaces.

Criteria	Weight	DoFP	DoA	DoAM	CIP
Instrument volume	5	1	0.75	0.5	0.75
Instrument complexity	4	1	0.75	0.25	0.25
Polarization accuracy	3	1	1	0.75	0.75
Polarization aliasing	1	0.5	1	1	1
Total		12.5	10.75	6.75	8

The polarization accuracy, as the third criterion, refers to the performance of the instrument. The last criterion is polarization aliasing, which is present in techniques like DoFP where large superpixels are required to modulate the polarization. The error in estimated polarization can be introduced if the state of polarization is not uniform over the whole area of superpixel used to reconstruct the polarization.

The result from trade-off showed that the DoFP is the best option. This is mainly due to a very simple configuration, with extremely small instrument volume. Compared with other techniques, DoFP polarimeter utilizes a micropolarizer array. The micropolarizer is integrated on top of the detector array. In most cases, the micropolarizer consists of four differently oriented linear polarizers: 0° , 45° , 90° , and 135° , forming a superpixel arranged in 2×2 array. This configuration of the polarimeters are only capable of measuring the linear components of the Stokes vector, S_1 and S_2 . In [36] showed a full-Stokes DoFP polarimeter, by using a LCP (Liquid crystal polymer) micropolarizer and LCP microretarder. To reconstruct the complete Stokes vector, a minimum of four measurements are needed. A similar concept is presented by [37], by using micropolarizer array made of a thin piece of birefringent crystal. Different retardances are achieved by changing the thickness of the crystal at the pixel level. They showed that this design takes advantage of four different retardances to measure the state of polarization of the incident beam from by the combination of four differently encoded pixels.

The following two subsection deals with the detailed description of the selected technique, the DoFP. This includes the reconstruction of polarization, the optimization, and polarimetric accuracy estimation.

4.2.1. MATHEMATICAL DESCRIPTION AND OPTIMIZATION CRITERIA

Since polarimeters are indirect sensing systems, the desired polarization parameters must be derived from a set of direct measurements of intensity. Hence, there is a system of equations, which must be solved. The known parameters are intensities measured on each pixel, but also the reconstruction matrix consisting the information how each pixel is modulated. The reconstruction matrix has many different names, by different researchers, for instance "instrument matrix", or "modulation matrix". Also, inverse of that matrix is known as the "data reduction matrix", or "demodulation matrix". [8] This reconstruction matrix can be optimized in such way, that amplification of error is minimum. This is done by making the matrix well-conditioned. That will ensure that the individual measurements by the polarimeter are as independent as possible. Also, this independence of the four modulated pixels (used to reconstruct a full-Stokes vector), can be graphically illustrated on the Poincaré sphere, where the vertices on the sphere are spaced in such a way that their distance is maximum. This results in a geometrical shape with maximum volume, which corresponds to regular tetrahedron inscribed inside the Poincaré sphere. [8] [36] [37]

The most general relation for the polarization state transformation of incident light passing through an optical component is related by the Mueller matrix (Eq. (3.60)):

$$\mathbf{S}_{\text{out}} = \mathbf{M} \mathbf{S}_{\text{in}} \quad (4.1)$$

The combined Mueller matrix of the system is equal to multiplication of two Mueller matrices: $\mathbf{M}_{\mathbf{p}}$ (the linear polarizer) and $\mathbf{M}_{\mathbf{w}}$ (the waveplate).

$$\mathbf{M} = \mathbf{M}_{\mathbf{p}} \mathbf{M}_{\mathbf{w}} \quad (4.2)$$

The waveplate can be defined by two parameters: the retardance, δ_i , and the fast axis orientation α_i (with respect to horizontal axis, x) of i th pixel. The Mueller matrix as a function of these two parameters for the

waveplate is equal to [37]:

$$\mathbf{M}_w = \begin{bmatrix} 1 & 0 & 0 & 0 \\ 0 & \cos^2(2\alpha_i) + \sin^2(2\alpha_i) \cos(\delta_i) & \sin(2\alpha_i) \cos(2\alpha_i) [1 - \cos(\delta_i)] & -\sin^2(2\alpha_i) \sin(\delta_i) \\ 0 & \sin(2\alpha_i) \cos(2\alpha_i) [1 - \cos(\delta_i)] & \sin^2(2\alpha_i) + \cos^2(2\alpha_i) \cos(\delta_i) & \cos(2\alpha_i) \sin(\delta_i) \\ 0 & \sin(2\alpha_i) \sin(\delta_i) & -\cos(2\alpha_i) \sin(\delta_i) & \cos(\delta_i) \end{bmatrix} \quad (4.3)$$

The Mueller matrix for the linear polarizer can be expressed as [37]:

$$\mathbf{M}_p = \frac{1}{2} \begin{bmatrix} 1 & \cos(2\theta_i) & \sin(2\theta_i) & 0 \\ \cos(2\theta_i) & \cos^2(2\theta_i) & \sin(2\theta_i) \cos(2\theta_i) & 0 \\ \sin(2\theta_i) & \sin(2\theta_i) \cos(2\theta_i) & \sin^2(2\theta_i) & 0 \\ 0 & 0 & 0 & 0 \end{bmatrix} \quad (4.4)$$

where θ_i is the angle from the transmission axis (with respect to horizontal axis, x) of i th pixel.

The first component of the outgoing Stokes vector, $S_{out,0}$ corresponds to the intensity of the light beam which is transmitted by the system. This value corresponds to the dot product of the incident state of polarization, described by the Stokes vector \mathbf{S}_{in} , with the first row of the combined Mueller matrix \mathbf{M} :

$$I = S_{out,0} = \frac{1}{2} [1 \ B \ C \ D] \begin{bmatrix} S_0 \\ S_1 \\ S_2 \\ S_3 \end{bmatrix} \quad (4.5)$$

where vector $\frac{1}{2}[1 \ B \ C \ D]$ represents the first row of the Mueller matrix, \mathbf{M} .

Therefore, the intensity that is transmitted depends on how the waveplate and the linear polarizer are designed, i.e. how the parameters α_i , δ_i , θ_i are chosen. The first extreme case is when the total transmission of the incident light occurs (the waveplate transforms the incident polarization into linear polarization along the linear polarizer). The second case is when nothing is transmitted through the system (the waveplate transforms the incident polarization into linear polarization perpendicular to the linear polarizer). These two cases are illustrated in Fig. 4.2. Therefore, there exists one type of the incident polarization that will be transformed in such a way, that all incident light is transmitted through the linear polarized. This is shown in Fig. 4.2 (a), where for a specific configuration of the waveplate and linear polarized ($\alpha = 60$ deg, $\delta = -60$ deg, and $\theta = 0$ deg), the incident polarization is (right-handed) elliptical polarization. In Fig. 4.2 (b), is the opposite case, which corresponds to (left-handed) elliptical polarization, oriented perpendicular to the first type of polarization. In this case, no light is transmitted through the linear polarizer, because the polarization after the waveplate becomes linear polarization perpendicular to the linear polarizer. Since there are four unknowns in the Stokes vector, to solve the system of equations, a minimum of four pixels are required. So, combining four different pixels (Eq. (4.5)), consisted of different combinations of the waveplates and linear polarizers, the system of equations can be written in matrix form:

$$\mathbf{I} = \mathbf{W} \mathbf{S}_{in} \quad (4.6)$$

where \mathbf{I} is a $n \times 1$ column vector containing the set of intensity measurements and \mathbf{W} (called polarimetric measurement matrix) is a $n \times 4$ matrix whose rows represent the first rows in Mueller matrices of corresponding pixel. The intensity vector, \mathbf{I} , and polarimetric measurement matrix, \mathbf{W} are known, while the incident Stokes vector is unknown, \mathbf{S}_{in} .

$$\begin{bmatrix} I_1 \\ I_2 \\ I_3 \\ I_4 \end{bmatrix} = \begin{bmatrix} S_{out,0,1} \\ S_{out,0,2} \\ S_{out,0,3} \\ S_{out,0,4} \end{bmatrix} = \frac{1}{2} \begin{bmatrix} 1 & B_1 & C_1 & D_1 \\ 1 & B_2 & C_2 & D_2 \\ 1 & B_3 & C_3 & D_3 \\ 1 & B_4 & C_4 & D_4 \end{bmatrix} \begin{bmatrix} S_0 \\ S_1 \\ S_2 \\ S_3 \end{bmatrix} \quad (4.7)$$

where $S_{out,0,i}$ represent the first Stokes parameter of the outgoing light, of i th pixel. The matrix \mathbf{W} is defined as:

$$\mathbf{W} = \frac{1}{2} \begin{bmatrix} 1 & B_1 & C_1 & D_1 \\ 1 & B_2 & C_2 & D_2 \\ 1 & B_3 & C_3 & D_3 \\ 1 & B_4 & C_4 & D_4 \end{bmatrix} \quad (4.8)$$

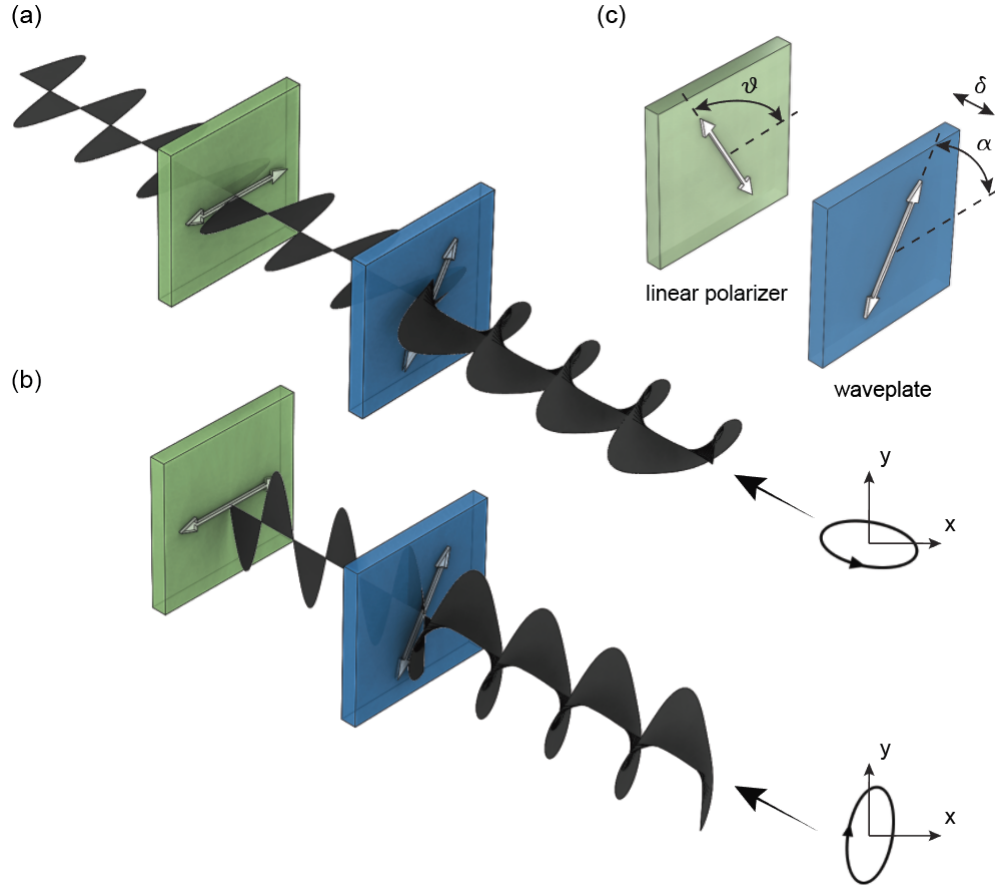


Figure 4.2: Schematic illustration showing how the waveplate and linear polarizer modify the two different types of the incident state of polarizations. (a) The waveplate transforms the first type of elliptical polarization into linear horizontal polarization. The linear polarizer is oriented in horizontal plane, and all light is transmitted. (b) The waveplate transforms the second type of elliptical polarization into linear vertical polarization. The linear polarizer is oriented the a horizontal plane, and no light is transmitted. (c) Definition of the three angles: α , δ , and θ .

The parameters B_i , C_i , D_i can be derived from Mueller matrices of corresponding pixels [36]:

$$B_i = \cos(2\theta_i) [\cos^2(2\alpha_i) + \sin^2(2\alpha_i) \cos(\delta_i)] + \sin(2\theta_i) \sin(2\alpha_i) \cos(2\alpha_i) [1 - \cos(\delta_i)] \quad (4.9)$$

$$C_i = \cos(2\theta_i) \sin(2\alpha_i) \cos(2\alpha_i) [1 - \cos(\delta_i)] + \sin(2\theta_i) [\sin^2(2\alpha_i) + \cos^2(2\alpha_i) \cos(\delta_i)] \quad (4.10)$$

$$D_i = \sin(2\theta_i) \cos(2\alpha_i) \sin(\delta_i) - \cos(2\theta_i) \sin(2\alpha_i) \sin(\delta_i) \quad (4.11)$$

where $i = 1, 2, 3, 4$ denotes the number of pixel, and therefore the row number in the matrix \mathbf{W} .

The Stokes vector of the incident light is determined by multiplying the inverse of \mathbf{W} by intensity vector \mathbf{I} .

$$\mathbf{S}_{\text{in}} = \mathbf{W}^{-1} \mathbf{I} \quad (4.12)$$

If the matrix \mathbf{W} of the polarimeter is well-known (from calibration of the polarimeter), and the measured vector of intensities \mathbf{I} , the value of \mathbf{S}_{in} can be obtained just by solving Eq. (4.12). For a full description of the solution \mathbf{S}_{in} , a minimum number of four independent pixel are required. Two different situations can be distinguished by taking into account if the number n of polarization analyzers is equal or higher than four. The first, when the matrix \mathbf{W} of Eq. (4.6) is a non-singular square matrix ($n = 4$), its inverse \mathbf{W}^{-1} exists and it is unique, leading to Eq. (4.12). The second, when the number of used pixels is larger than four ($n > 4$), \mathbf{W} is a

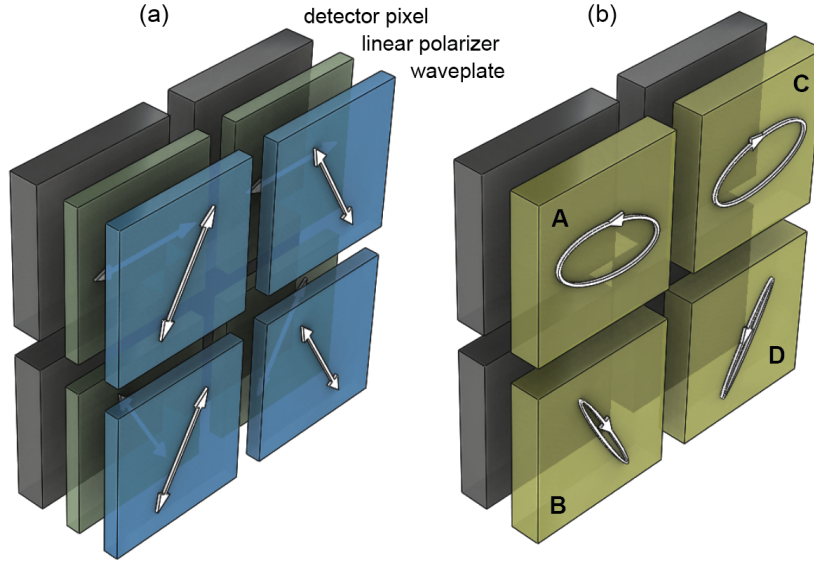


Figure 4.3: Schematic representation of the more general DoFP concept. A set of four different modulating pixel form a superpixel. Three angles are required to fully describe each pixel: α , δ , and θ

$n \times 4$ rectangular matrix and in general no solution exists. However, the solution can be found by minimizing the mean square error by the use of the pseudoinverse $\tilde{\mathbf{W}}^{-1}$, which is defined in Eq. (4.13):

$$\mathbf{S}_{\text{in}} = \left(\mathbf{W}^T \mathbf{W} \right)^{-1} \mathbf{W}^T \mathbf{I} = \tilde{\mathbf{W}}^{-1} \mathbf{I} \quad (4.13)$$

where \mathbf{W}^{-1} , \mathbf{W}^T and $\tilde{\mathbf{W}}^{-1}$ are the inverse, the transpose and the pseudoinverse of the matrix \mathbf{W}^{-1} , respectively.

In presence of noise, different configurations of matrix \mathbf{W} will transmit the error in a different way. In fact, as a consequence of the not idealistic optical elements, and error in measuring the intensity at detector pixel, the values of the reconstructed Stokes vector will always be associated with an error.

In case of Eq. (4.12) and 4.13, the effect of noise within the intensity vector \mathbf{I} will introduce error in estimated Stokes vector:

$$\mathbf{S}_{\text{in}} + \Delta \mathbf{S}_{\text{in}} = \mathbf{W}^{-1} (\mathbf{I} + \Delta \mathbf{I}) \quad (4.14)$$

$$\mathbf{S}_{\text{in}} + \Delta \mathbf{S}_{\text{in}} = \tilde{\mathbf{W}}^{-1} (\mathbf{I} + \Delta \mathbf{I}) \quad (4.15)$$

where $\Delta \mathbf{I}$ is the error associated to the intensity measurements and $\Delta \mathbf{S}_{\text{in}}$ the solution transmitted error in Stokes vector.

There are three different indicators that can be used to minimize the noise transmitted through the matrix inversion, from the vector \mathbf{I} to the solution \mathbf{S}_{in} : the condition number (CN), the Equally Weighted Variance (EWV) and the error associated at every component of the Stokes vector. [38] The CN quantifies if the matrix \mathbf{W}^{-1} is well-conditioned (not singular). The EWV and the variance associated at every component of \mathbf{S}_{in} are related with the propagation of errors from the vector \mathbf{I} to the solution \mathbf{S}_{in} . The theoretical minimum value of CN is equal to 1, which is obtained for unitary matrices as they do not amplify the error. However, this low value of CN can not be achieved for matrix \mathbf{W} . For a polarimeter, $\sqrt{3}$ is a minimum value of CN. [37] [38] Since there are multiple definitions of condition number, in this work it is used definition used in [38]:

$$CN(\mathbf{W}) = \frac{\sigma_{\max}(\mathbf{W})}{\sigma_{\min}(\mathbf{W})} \quad (4.16)$$

where σ_{max} and σ_{min} are the maximum and minimum singular values different from zero of the matrix \mathbf{W} .

In this work only CN is considered in the optimization of matrix \mathbf{W} . By applying this optimization for $n = 4$, the results lead to four sets of the waveplates and linear polarizers that represented upon the Poincaré sphere, correspond to the vertices of a regular tetrahedron. By repeating the optimization process, in all the cases regular tetrahedrons are obtained with the same (minimum) CN , but with different orientations. Therefore, there are infinite solutions that give the best solution (CN) when optimizing a polarimeter with four pixels. In other words, the minimized CN leads to a system of equations, with maximum independence of parameters. The noise propagation of the intensity measurements is minimized. This more general modulation of polarization has an advantage when metasurfaces are used. This is due to the fact that there are more degrees of freedom in designing the nanostructures, because of the infinite number of possible solutions. Table 4.2 shows results of optimization of matrix, \mathbf{W} (Eq. (4.8)) for two the different configurations. In the first configuration (**Configuration 1**), when only angle of the linear polarizers, θ is constrained, and equal to 90 deg for all four analyzers. The resulting angles for waveplate fast axis, α and retardance, δ is the one possible solution with smallest CN . In second configuration (**Configuration 2**) some additional restrictions are set in order to simplify the simulation of metasurfaces (see Section 4.3.1). The values of selected orientation angles (α , and δ) are selected in such a way to be aligned with hexagonal lattice axes (0, 60 and 120 deg). As can be seen for this configuration (**Configuration 2**) the CN is still high, equal to 1.8278. The used optimization algorithm is *interior-point*.

Table 4.2: Result of optimization of matrix, \mathbf{W} for two the different configurations. The parameters used in optimization are: α , δ , and θ . In **Configuration 1**, only θ is constrained, and the chosen value is 90 deg. In **Configuration 2**, two parameters are constrained: α , and θ . The chosen values $\alpha = [60\ 60\ 120\ 120]$, and $\theta = [0\ 120\ 0\ 60]$. The criteria for the optimization is minimization of condition number, CN . Values of angles are in degrees, and the font of the results of optimization is in bold text style.

	CN	Pixel A $\begin{bmatrix} \alpha_1 \\ \delta_1 \\ \theta_1 \end{bmatrix}$	Pixel B $\begin{bmatrix} \alpha_2 \\ \delta_2 \\ \theta_2 \end{bmatrix}$	Pixel C $\begin{bmatrix} \alpha_3 \\ \delta_3 \\ \theta_3 \end{bmatrix}$	Pixel D $\begin{bmatrix} \alpha_4 \\ \delta_4 \\ \theta_4 \end{bmatrix}$
Configuration 1 (with constrained θ)	1.7321 ($\approx \sqrt{3}$)	102.2671 102.5608 90	33.4199 137.1592 90	139.8419 132.7521 90	69.6638 129.3268 90
Configuration 2 Selected configuration (with constrained α and θ)	1.8278	60 60 0	60 14 120	120 60 0	120 14 60

4.2.2. STOKES ERROR AS FUNCTION OF DIFFERENT INCIDENT POLARIZATION STATES

In this thesis the term polarimetric accuracy is used to describe the performance of polarimeter. It is defined as an uncertainty in Stokes parameters. It describes the noise level in polarization above which a polarization signal can be detected (in some literature is also called polarimetric sensitivity). [8]

In this subsection is shown the performance of the selected configuration (**Configuration 2**) shown in Table 4.2 for the shot noise limited system. The shot noise of every pixel is estimated by the expression:

$$I_{noise,i} = N_{randn} \sqrt{S_{out,0,i}} \quad (4.17)$$

where $I_{noise,i}$ is estimated intensity measured on the detector of i th pixel, N_{randn} is normally distributed random number (generated by Matlab function), and $S_{out,0,i}$ (Eq. (4.1)) is the outgoing intensity passing through ideal system composed of corresponding waveplate and linear polarizer, defined by Mueller matrix in Eq. (4.2).

The estimated intensity on the detector, $I_{det,i}$ of i th pixel is calculated as:

$$I_{det,i} = S_{out,0,i} + I_{noise} = S_{out,0,i} + N_{randn} \sqrt{S_{out,0,i}} \quad (4.18)$$

Using Eq. (4.13) the Stokes vector, \mathbf{S}_{est} is estimated, where \mathbf{I}_{det} is $n \times 1$ vector containing simulated intensities at all pixels:

$$\mathbf{S}_{est} = \tilde{\mathbf{W}}^{-1} \mathbf{I}_{det} \quad (4.19)$$

Then the relative error of normalized Stokes parameters is defined as:

$$ES_k = \frac{S_{in,k} - S_{est,k}}{S_{in,0}} \quad (4.20)$$

where ES_k is error in k th Stokes parameter. In the end, by taking the standard deviation of the certain number of simulation gives the estimation of uncertainty in reconstructed Stokes parameters. The number of simulations (each generating different random numbers for noise estimation) used is equal to 200. The result is vector with the shape of $n \times 1$, \mathbf{ES}_k representing the result of errors in Stokes parameters for 200 simulations.

$$\sigma(\mathbf{ES}_k) = std(\mathbf{ES}_k) \quad (4.21)$$

In Fig. 4.4 (a) is shown 1000 uniformly sampled incident states of polarization, which can be visually seen

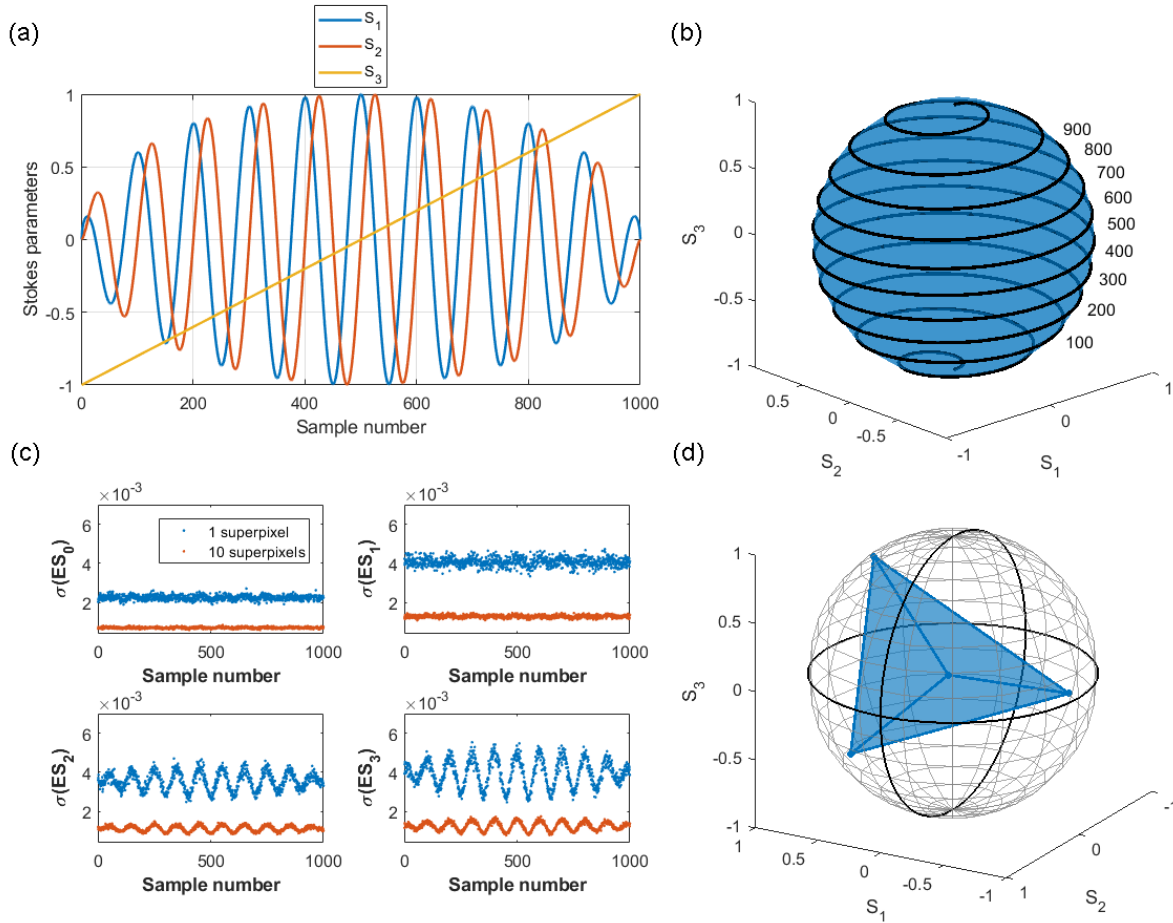


Figure 4.4: (a) Stokes parameters vs. sample number diagram. Sample number is related to different incident polarization states, as indicated on the Poincaré sphere (b), starting from the bottom, and ending at the top of the sphere. (c) The standard deviation of error in estimated Stokes vs. sample number diagram due to the shot noise. Blue points represent 1 superpixel, while red points 10 same superpixels. (d) Four points (**Configuration 2**, Table 4.2) forming tetrahedron inscribed inside Poincaré sphere, which represent response of four combinations of waveplates (α , δ) and linear polarizers (θ).

on Poincaré sphere (Fig. 4.4 (b)), starting from the bottom, spiraling to the top of the sphere. In Fig. 4.4 (c) can be seen the result for the standard deviation of error in Stokes parameters (all four Stokes parameters) as a function of 1000 different incident polarization states. Lastly, Fig. 4.4 (d) represents four differently modulated pixels that form a tetrahedron (denoted by blue lines) inscribed inside Poincaré sphere for the values listed in the second configuration (Table 4.2, **Configuration 2**). The point of calculating the uncertainty for

the 1000 different incident polarizations is to show how the uncertainty is related to different incident states of polarization. It can be seen that for this specific configuration, the uncertainty in Stokes parameters S_0 and S_1 is mostly uniform, while S_2 and S_3 oscillate as function of the state of the polarization. This can be explained as a property of matrix, \mathbf{W} (or how the four points on Poincaré sphere are distributed), which does not amplify the error equally for different inputs (\mathbf{S}_{in}). By proper tuning, it is possible to optimize for certain states of polarization.

The result of uncertainty calculations is a preliminary estimation of polarization sensitivity. In Fig. 4.4 (c) are shown two simulations. First (denoted with blue dots) are for a single superpixel (4 different pixels), and second (denoted with red points) are for 10 same superpixels. As can be seen by increasing the number of pixels the standard deviation is decreased from $\approx 4 \times 10^{-3}$ to $\approx 1 \times 10^{-3}$ (the assumption is that state of polarization of incident light is the same at all 10 superpixels). The reason for that is increase in the total amount of the signal that is measured and therefore increase in signal-to-noise ratio (SNR). The simulated amount of the signal on each pixels in this calculation is used to be equal to 10^5 (i.e. the incident Stokes, \mathbf{S}_{in} is normalized to that value), which is approximately the limit for detector pixel's well depth (limit in how many electrons the pixel can store before it saturates). For the shot noise limited system, the signal of 10^5 electrons correspond to the signal-to-noise ratio, $SNR = 316$ at each pixel. The purpose of this calculation is to estimate theoretical minimum of the uncertainty in Stokes parameters. The uncertainty calculation of a real design, including the other sources of noise is estimated in Subsection 5.7.2.

4.3. METASURFACE DESIGN OPTIONS

The recent advances in metasurfaces have been applied to the demonstrations of many exotic optical phenomena and various useful planar optical devices. Many of these metasurface-based applications are promising alternatives to replace conventional optical devices, as they largely benefit from ultra-thin, lightweight, and ultra compact properties, provide the possibility of overcoming several limitations suffered by their traditional counterparts, and demonstrate versatile novel functionality. [9] Fig. 4.5 illustrates schematically an overview of metasurface applications. It can be seen that the functions of many traditional optical components can be also achieved by metasurfaces.

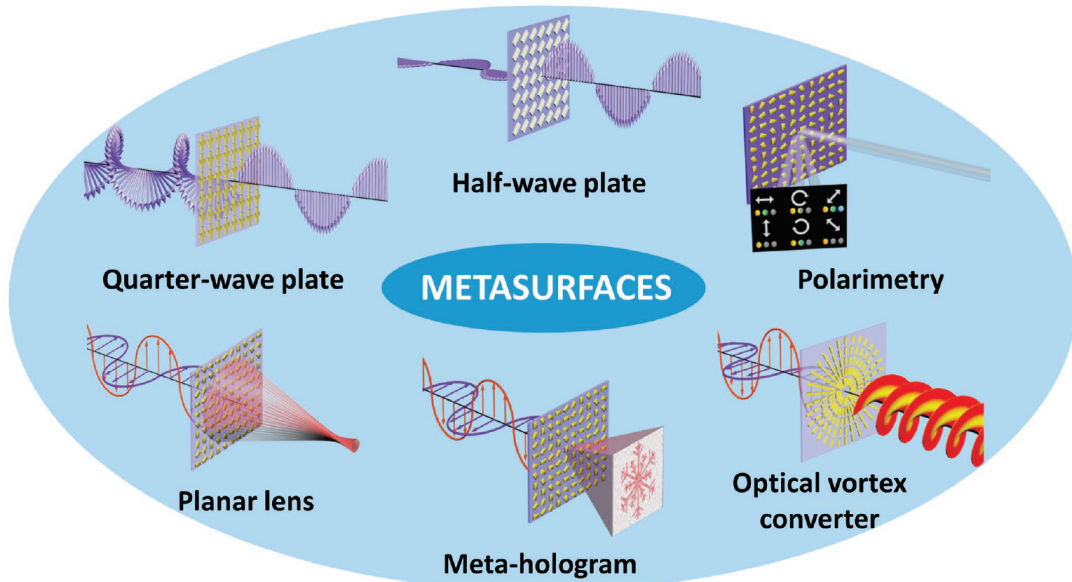


Figure 4.5: A general overview of metasurface-based applications on polarization control and wavefront shaping [9]

As already shown in the previous section, in this research, a different approach is studied, where full polarization states are encoded by four different surfaces, each consisting of a combination of two layers of

metasurfaces which have functions of waveplate, and linear polarizer, respectively. As discussed later, the second layer which operates as linear polarizer will also operate as a spectral filter. That allows measuring the polarization state at different wavelengths. This concept allows a design of full-Stokes spectro-polarimeter consisted of only two layers of metasurfaces. In this case, the layers of metasurfaces are integrated closely to the detector array, providing low cross-talk among adjacent pixels.

In [34] is shown that full control of phase and polarization is possible by resonators in the shape of elliptic cylinders. By proper design of diameters of ellipse and orientation of elliptic cylinder, any value of retardance of phase and fast axis can be achieved, respectively. Furthermore, in [9] are presented several examples of metasurface-based quarter-wave plates and half-wave plates.

In [11] is proposed and experimentally demonstrated an metasurface-based optical bandpass filter. It is a Fabry-Pérot (FP) resonator created by two distributed Bragg reflectors (DBRs). A metasurface is embedded inside the FP cavity as a phase shifting layer. The center wavelength of the filter is tuned by changing the transverse dimension of the metasurface nanostructures, while the height of the cavity is constant. The filter can be integrated on top of the detector array to realize on-chip high-resolution spectrometers.

In this research is shown a different concept, by using asymmetrical metasurfaces embedded inside a Fabry-Pérot cavity. That allows the separation of central wavelengths for two orthogonal polarizations. This principle enables to filter out a narrow band of the spectrum at only one polarization orientation. Therefore, this layer has two functions: as a linear polarizer, and as a narrowband spectral filter.

4.3.1. METASURFACE LATTICE SELECTION

In this subsection, the type of the metasurface lattice is selected. In [39] showed that the rotational symmetry of metasurfaces is the important parameter, especially for the incident plane waves at an oblique angle. An increase in rotational symmetry can increase their small range of operational angles, which is one of the limiting factors of metasurfaces.

Since the properties of metasurfaces are defined by the response of an individual scatterers, as well as by its coupling to neighbors. When the area of elliptic cylinder's cross-section is large enough, close to the period of the lattice, the orientation angle, φ of the cylinder has a huge impact on the response of the metasurface. In Fig. 4.6 (a) is illustrated top view of an elliptic cylinder oriented at an angle φ with respect to the x axis. The R_a , and R_b are the major, and minor axis of the ellipse, respectively. In Fig. 4.6 (b) and (c) are depicted two considered types lattices, square, and hexagonal, respectively. Fig. 4.6 (d) shows how the total transmittance changes as a function of different orientation angles of elliptic cylinders, φ for the two different lattices, square and hexagonal, at a normal incident plane wave. It can be noticed that when the size of the ellipse is small with respect to the lattice ($R_a = 122$ nm, and $R_b = 54$ nm), the transmittance is mostly uniform for different orientations of the elliptic cylinders. However, when the diameters are large enough (close to the period of the lattice, $R_a = 220$ nm, and $R_b = 97$ nm), the transmittance is not uniform, but periodic, where period corresponds to the angle of lattice axes. Therefore, for the square lattice, the period is 90 degree, while for the hexagonal lattice is 60 degree. Also, the amplitude of the oscillations is a little bit smaller for the hexagonal lattice.

Although the response for the different orientations of cylinders, φ is almost the same, the argument for choosing the hexagonal lattice is due to the faster simulation of metasurfaces. This allows to simulate the metasurface only once, for the elliptic cylinders oriented only at 0 deg angle, and the response of metasurface for two other orientations 60 and 120 deg (orientation of hexagonal lattice), is calculated by simple rotation expression of Jones matrix (Eq. (3.44)). This is possible due to the symmetry of the lattice. This is the reason why the orientations for the fast axes, α and angles of linear polarizers, θ are chosen in **Configuration 2** (Table 4.2) to be oriented along the axes of the hexagonal lattice.

The used material of the elliptic cylinder is amorphous silicon, ($a - Si$), with refractive index $n_{a-Si} = 3.6392$ (by *Pierce and Spicer 1972*). The height of the cylinder used in this simulation is 600 nm. The material of the substrate is fused silica, SiO_2 , with refractive index $n_{SiO_2} = 1.4504$ (by *Malitson 1965*). The height of the substrate is 2000 nm (due to simplification height of the substrate is not to the scale in the Fig. 4.6 (d)). The free space wavelength is $\lambda = 1000$ nm.

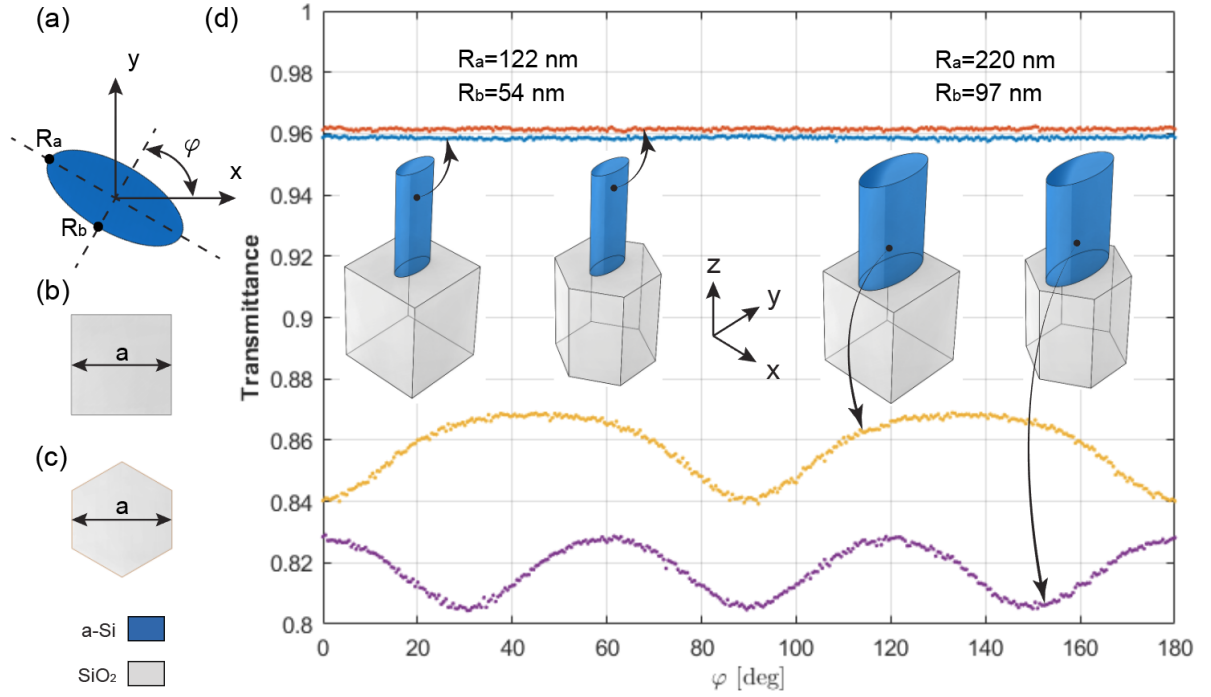


Figure 4.6: (a) top view of an elliptic cylinder oriented at an angle φ with respect to the x axis. The R_a , and R_b are the minor and major axis of the ellipse, respectively. (b) and (c) are two considered types lattices, square, and hexagonal, respectively. (d) Transmittance vs. cylinder's orientation angle, φ diagram for four different geometrical models of the simulated unit cell of the metasurfaces: two different lattices, and two different diameters of the ellipse.

4.4. DIELECTRIC METASURFACE AS MICROPATTERNED WAVEPLATE

The metasurface consisting of an array of elliptic cylinders can provide same performance as the birefringent crystal, operating as a waveplate with the required phase shift between two orthogonal polarizations. The plane wave, whose free space wavelength is λ , propagating in the isotropic medium of refractive index n , is retarded by $2\pi nd/\lambda$. If the medium is uniaxially linearly birefringent, the refractive indices for two orthogonal axes are different (n_e , and n_o), causing different propagation speeds (c/n_e , and c/n_o) of the plane wave for two orthogonal polarizations. n_e , and n_o are known as the ordinary and the extraordinary refractive indices of the medium, respectively. The result is relative retardation in phase, and its value depends on propagation distance d (thickness of the material).

The waveplate can be described mathematically by Jones matrix [17]:

$$\mathbf{T}_w = \begin{bmatrix} e^{-j\delta_x} & 0 \\ 0 & e^{-j\delta_y} \end{bmatrix} \quad (4.22)$$

where

$$\delta_x = \frac{2\pi d}{\lambda} n_e, \quad \delta_y = \frac{2\pi d}{\lambda} n_o \quad (4.23)$$

The relative retardation (y with respect to x) can be expressed as:

$$\delta = \frac{2\pi d}{\lambda} (n_o - n_e) \quad (4.24)$$

The quantity $(n_o - n_e)$ is called the birefringence of the medium. For $n_e < n_o$ (negative birefringence), the x axis is called the fast axis of the linear retarder and the y axis is called its slow axis. [17] For the positive birefringence, x and y axes become the slow and fast axes, respectively. Note that this relation is just an approximation because multiple reflections between the parallel faces of the waveplate are ignored. Also,

the assumption is that there is no absorption in the medium. When it comes to an array of pixelated waveplates, where each pixel has a different retardance and fast axis orientation, the manufacturing becomes very complicated. This is due to the small scale of pixels (about ten micrometers). In order to achieve that with conventional birefringent crystals, each waveplate should have a different height for corresponding retardance, and also the different orientation of the crystal for corresponding fast axis orientation.

However, the metasurface-based waveplates operate on different principle, where the retardance is achieved by designing different ratios of major and minor axes of elliptic cylinders, while the height of the metasurface-based waveplate is unchanged. Also, the fast axis orientation corresponds to the orientation of elliptic cylinders.

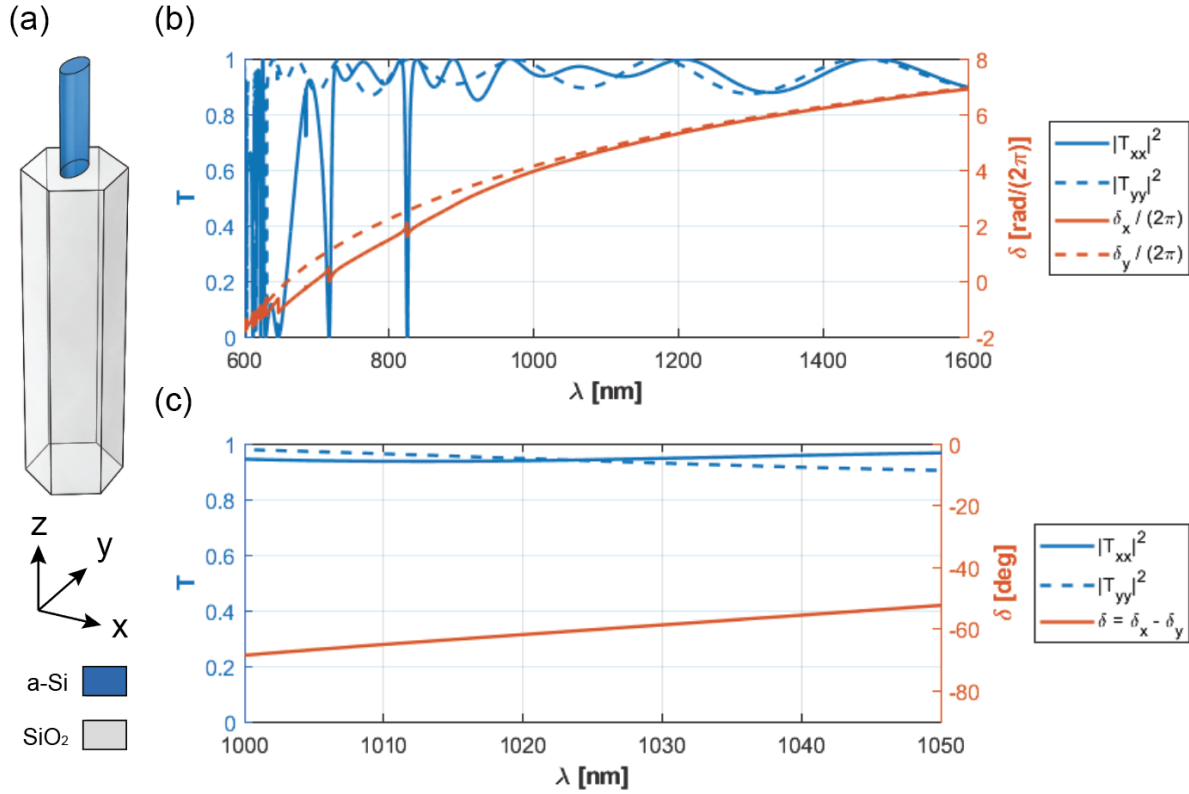


Figure 4.7: (a) The geometrical model of the simulated unit cell of the metasurface consisted of an array of elliptic cylinders in a hexagonal lattice (with minor and major diameters: $D_x = 108$ nm, and $D_y = 244$ nm). (b) The result of the simulation. The left side of the vertical axis corresponds to the transmittance, and the right side of the vertical axis corresponds to the phase of the electric field. Solid lined represents the polarization in x , and the dashed line represents the polarization in y direction. On the horizontal axis is free space wavelength. (c) Closer look for the shorter range of the spectrum, where can be seen how the transmittance and retardance are mostly uniform.

In Fig. 4.7 (a) is illustrated the geometrical model of the simulated unit cell of a metasurface, consisted of an array of elliptic cylinders in a hexagonal lattice. In Fig. 4.7 (b) is shown the result of the simulation. The left side of the vertical axis corresponds to the transmittance, and the right side of the vertical axis corresponds to the phase of the electric field. Solid lines represent the polarization in x , and the dashed line represents the polarization in y direction. On the horizontal axis is free space wavelength. In Fig. 4.7 (c) is closer look for the shorter range of the spectrum, where can be seen how the transmittance and retardance are mostly uniform. Beside uniform transmittance, an equal transmittance for two orthogonal axes is also an important parameter. The used material of the elliptic cylinder is amorphous silicon, ($a-Si$), with refractive index $n_{a-Si} = 3.6392$ (by *Pierce and Spicer 1972*). The ellipse is oriented along the x and y axes, with minor and major diameters: $D_x = 108$ nm, and $D_y = 244$ nm, respectively. The height of the cylinder is 600 nm. The material of the substrate is fused silica, SiO_2 , with refractive index $n_{SiO_2} = 1.4504$ (by *Malitson 1965*). The

height of the substrate is 2000 nm. Note that, due to simplification of the simulations, the refractive indices are kept constant over different wavelengths, corresponding to operating wavelength, $\lambda = 1000$ nm. In Fig. 4.7 (b) can be noticed a several absorption dips, at $\lambda = 825$ nm, and $\lambda = 717$ nm, and many more at shorter wavelengths. This can be interpreted as spectral range, where the resonances of magnetic and electric dipoles do not overlap spectrally. At longer wavelengths, the transmittance is mostly uniform, which corresponds to the spectral range where the resonances of magnetic and electric dipoles overlap spectrally. Since the phase difference (retardance) is changing over the spectrum, the required retardance can be achieved by proper design of the minor and major axis of the ellipse. In general larger ratio of ellipse results in larger retardance. Another parameter that affects the retardance is the cylinder height, where the height is proportional to the retardance. This specific waveplate is optimized for the **Pixel A** (in Table 4.2), with retardance, $\delta_1 = -60$ deg. The criteria for the optimization is equal transmittance for the orthogonal polarizations, $|T_{xx}|^2 = |T_{yy}|^2$ at operating wavelength (see Fig. 4.7 (c)). In this case, the operating wavelength is about 1023 nm (the selection of operating wavelength is discussed in next Section 4.5). At this point, it is important that $a - Si$ is not lossless overall spectrum. At shorter wavelengths near UV, it becomes very lossy, and for that reason, another material is considered. The appropriate material is titanium dioxide (TiO_2). More detailed discussion on that continues in Section 5.3. In Fig. 4.8 (a) is illustrated another simulated geometrical model, consisting of

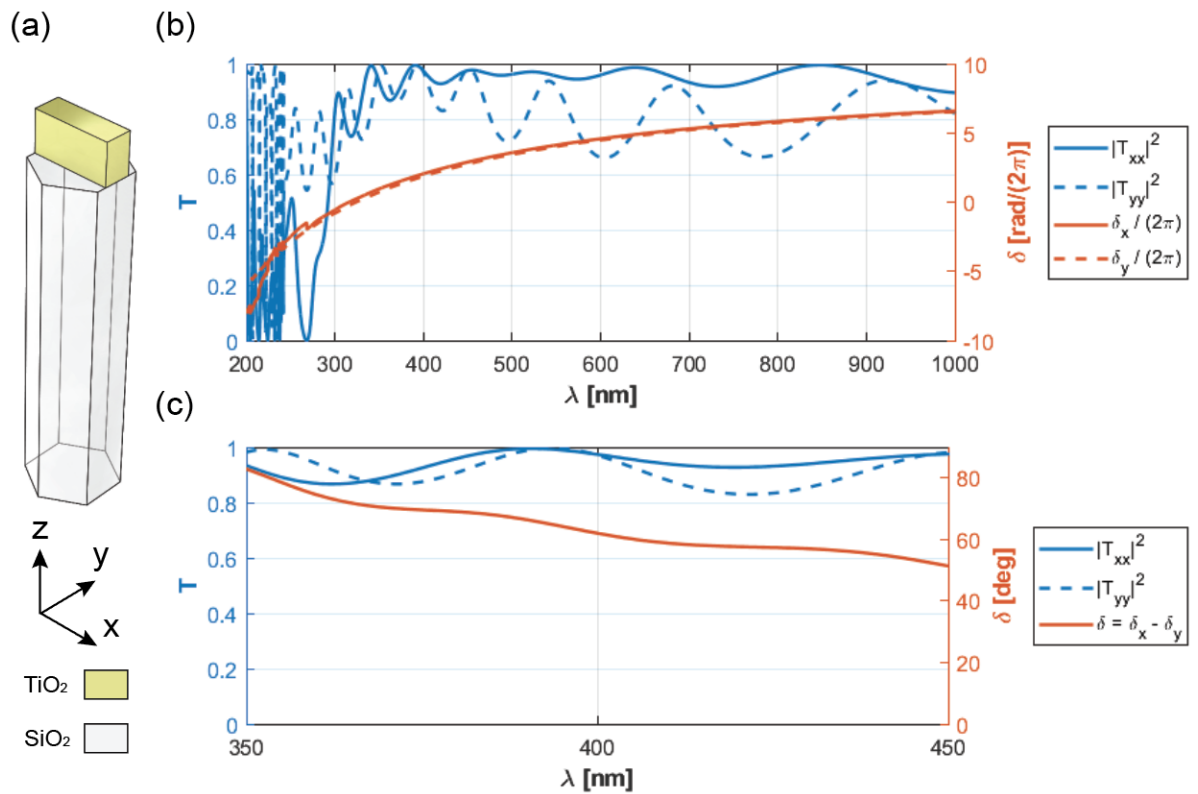


Figure 4.8: (a) The geometrical model of the simulated unit cell of the sub-wavelength grating, with the rectangular grating width of $w = 65$ nm, the height of $h_g = 100$ nm, and the grating period of $a_g = 220$ nm (b) The result of the simulation. The left side of the vertical axis corresponds to the transmittance, and the right side of the vertical axis corresponds to the phase of the electric field. Solid lined represents the polarization in x , and the dashed line represents the polarization in y direction. On the horizontal axis is free space wavelength. (c) Closer look for the shorter range of spectrum, where can be seen how the transmittance and retardance are mostly uniform.

an array of a rectangular sub-wavelength grating in a hexagonal lattice. Since the TiO_2 has a lower refractive index, to achieve the same contrast between two orthogonal axes, i.e. same retardance, higher "aspect ratio" of the nanostructure is required. This results in the grating, which has an aspect ratio equal to infinity. In Fig. 4.8 (b) is shown the result of the simulation. The left side of the vertical axis corresponds to the transmittance, and the right side of the vertical axis corresponds to the phase of the electric field. Solid lines represent the

polarization in x , and the dashed line represents the polarization in y direction. On the horizontal axis is free space wavelength. In Fig. 4.7 (c) is closer look for the shorter range of the spectrum, where can be seen how the transmittance and retardance are mostly uniform. The used material of the grating is titanium dioxide (TiO_2) with refractive index $n_{TiO_2} = 2.6811$ and extinction ratio $k_{TiO_2} = 0.00064934$ (by *Siefke et al. 2016: Thin film*). The grating is oriented along the x axis, with the grating width of $w = 65$ nm. The height of the grating is $h_g = 100$ nm. The period of the lattice is $a = 190.5$ nm, which correspond to the period of the grating $a_g = 220$ nm. The material of the substrate is fused silica, SiO_2 , with refractive index $n_{SiO_2} = 1.4701$ (by *Malitsson 1965*). The height of the substrate is 2000 nm. Note that, due to simplification of the simulations, the refractive indices are kept constant over different wavelengths, corresponding to operating wavelength, $\lambda = 400$ nm.

4.5. DIELECTRIC METASURFACE AS MICROPATTERNED PLEOHROIC FABRY-PÉROT FILTER

In this section, the design of the second layer of the spectrometer, i.e. linear polarizer is shown. It is important to note that, this second layer has two functions: as a spectral filter, and as a linear polarizer. The measurement of the spectral information is usually achieved by dispersing the light along the detector array, with a diffraction grating. However, in this design different approach is utilized. This is done by creating an array of spectral filters distributed along the detector array.

The most common way to filter out a narrow band of spectrum is to implement a Fabry-Pérot (FP) filter (also called: resonator or cavity). To clarify the terminology, there exist two different terms for FP filter: Fabry-Pérot interferometer and Fabry-Pérot etalon. The former consists of two parallel highly reflecting mirrors, and the latter is made of a transparent plate with two reflecting surfaces. In both cases, an optical cavity (resonating cavity) is created, which is separated by a distance L_{cav} (the length (height) of the cavity). A schematic illustration of the FP cavity with two reflectors of reflectivity R_1 and R_2 is depicted in Fig. 4.9. Plane waves propagating inside the cavity will interfere constructively and destructively, depending on the wavelength of the incident light. This results in stable (allowed) optical modes and attenuated (disallowed) optical modes, respectively. For lossless (non-absorbing) reflectors, the transmittance of each reflector is equal to $T_1 = 1 - R_1$, and $T_2 = 1 - R_2$. Due to the multiple reflections inside the cavity, the transmittance through the FP cavity can be expressed in terms of a geometric series. The relation for the transmittance is equal to [10]:

$$T = \frac{T_1 T_2}{1 + R_1 R_2 - 2\sqrt{R_1 R_2} \cos(2\phi)} \quad (4.25)$$

where ϕ is the phase change of the wave for a single pass between the two reflectors. In this relation, the phase changes at the reflector are neglected. When the condition of constructive interference is fulfilled, ($2\phi = 0, 2\pi, \dots$), the maximum values of the transmittance occur. Near the maximum, the transmittance has a shape of a Lorentzian function. The phase change, ϕ is related to wavelength by relation [10]:

$$\phi = 2\pi \frac{n_{cav} L_{cav}}{\lambda} = 2\pi \frac{n_{cav} L_{cav} \nu}{c} \quad (4.26)$$

where n_{cav} is the refractive index of the cavity, L_{cav} is the length of the cavity, λ is the free space wavelength, and ν is the frequency of light.

Resonator modes of the cavity can be divided into two types: longitudinal modes, which differ in frequency from each other, and transverse modes, which may differ in both frequency, and intensity pattern of the light. The basic or fundamental transverse mode of a resonator is a Gaussian beam. In the simple cavity, the allowed longitudinal modes of the cavity are those where the mirror separation distance L_{cav} is equal to an exact multiple of half the wavelength, λ . The relation relating the length of the cavity and the resonant free space wavelength, λ is equal to [40]:

$$L_{cav} = q \frac{\lambda}{2 n_{cav}} \quad (4.27)$$

where q is the longitudinal mode number. The cavity quality factor Q is defined as the ratio of the transmittance peak frequency to the peak width [10]:

$$Q = \frac{f}{\Delta f} = \frac{2 n_{cav} L_{cav}}{\lambda} \frac{\pi \sqrt[4]{R_1 R_2}}{1 - \sqrt{R_1 R_2}} \quad (4.28)$$

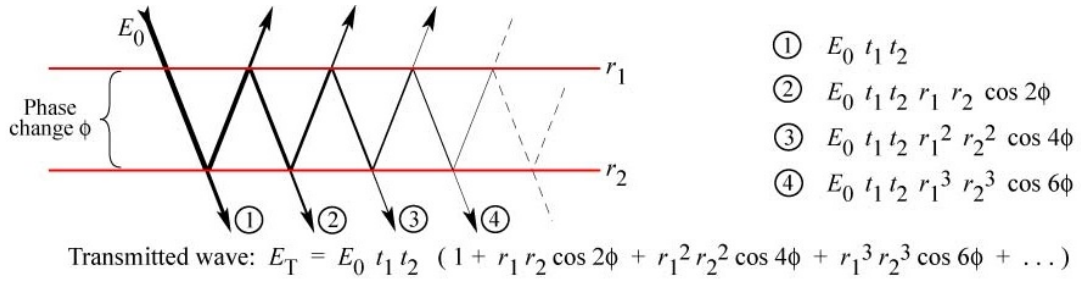


Figure 4.9: Transmission of a light wave with electric field amplitude E_0 through a Fabry-Pérot resonator. [10]

where f is resonant frequency, and Δf is the resonance width or full width at half maximum (FWHM), the bandwidth over which the transmittance is greater than half the transmittance at the resonant frequency.

The quality factor, Q characterizes a resonator's bandwidth relative to its center frequency. Higher Q indicates a lower rate of energy loss relative to the stored energy of the resonator (the oscillations are attenuated more slowly). [41]

In order to achieve high spectral resolution, the mirrors of the FP cavity should have very high values of reflectance. The metallic mirrors can provide high reflectance. However, they are not suitable for resonant applications due to high losses. Interference structures made of dielectric materials can provide a high reflectance and high efficiency. These types of structures are called multilayer high-reflectance coatings, and also, distributed Bragg reflector (DBR). They are formed of quarter-wave layers of alternate high and low refractive indices. The thicknesses of the low and high refractive index DBR layers, h_L and h_H , respectively, are defined by equation (for a normal incidence of light):

$$h_L = \frac{\lambda}{4n_L}, \quad h_H = \frac{\lambda}{4n_H} \quad (4.29)$$

where λ is the center (resonant) wavelength, n_L is the refractive index of DBR layer with lower refractive index, and n_H is the refractive index of DBR layer with higher refractive index, respectively.

The beams reflected at a low-to-high refractive index boundary undergoes a 180 degree phase shift (phase is inverted), while at high-to-low refractive index boundary the phase shift does not occur. That will ensure that all reflected beams will be in phase, leading to strong constructive interference. [3] Dielectric mirrors are capable to produce ultra-high reflectivity mirrors: values of 99.999% or better over a narrow range of wavelengths. Mirrors of this type are very common in optics, due to improved techniques that allow inexpensive manufacture of high-quality mirrors. The reflectivity of the DBR can be estimated by the relation:

$$R = \left[\frac{n_0(n_2)^{2N} - n_s(n_1)^{2N}}{n_0(n_2)^{2N} + n_s(n_1)^{2N}} \right]^2 \quad (4.30)$$

where n_0 , n_1 , n_2 and n_s are the respective refractive indices of the originating medium, the two alternating materials, and the terminating medium (i.e. backing or substrate), and N is the number of repeated pairs of low/high refractive index material.

Increasing the number of pairs in a DBR increases the mirror reflectivity. Furthermore, increasing the refractive index contrast between the materials in the Bragg pairs increases both the reflectivity and the bandwidth. A common choice of materials for the stack is titanium dioxide ($n \approx 2.5$) and silica ($n \approx 1.5$). [42]

Different central wavelengths of a FP filter can be achieved by changing the length of the cavity (Eq. (4.27)). There are already companies that implemented this approach, by making an array of pixelated Fabry-Pérot filters, by varying the length of the cavity. One example is HinaLea Imaging. They developed the world's first battery-operated, hand-held staring hyperspectral camera based on FPI (Fabry-Pérot interferometers). [43]

Another company is XIMEA which developed hyperspectral imaging camera based on Fabry-Pérot interferometers. [44], In this case, filtering of different wavelengths is achieved by changing the cavity heights.

A method to effectively vary the central wavelengths of a FP filter is proposed by [11] by putting a dielectric nano-structures (metasurface) inside the cavity as a phase shifting element between two highly reflective mirrors. This allows precise control of the filter's passband independently of the length of the cavity. Different geometries of the nanostructures inside the cavity (Fig. 4.10), will provide different phase shifts. Therefore, the resonant wavelength can be tuned without changing the physical distance between the two mirrors (enables only one lithographic step during the fabrication). Fig. 4.10 shows the dielectric metasurface layer incorporated in vertical FP resonators.

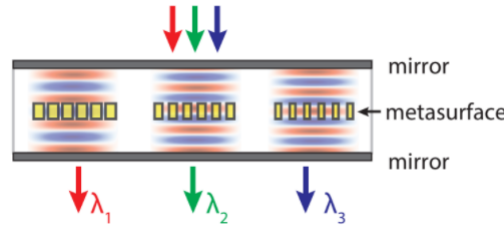


Figure 4.10: Schematic of the proposed bandpass filter array composed of vertical DBR-based micro-cavities, in which transmissive dielectric metasurface layers are inserted as phase shifting layers to tune their resonance wavelengths over a broad bandwidth. [11]

In Fig. 4.11 are depicted two simulated geometrical models of FP filters. First model (Fig. 4.11 (a) and (b)) represents simple single cavity FP filter, designed for resonant wavelength $\lambda = 1000$ nm. Fig. 4.11 (a) shows the front view of the geometrical model of unit cell of a FP cavity formed by two DBR mirrors consisted of 6 pairs of layers. The selected materials of high and low refractive index of DBR are titanium dioxide (TiO_2) with refractive index $n_{TiO_2} = 2.3137$ (by Siefke et al. 2016: Thin film), and fused silica (SiO_2) with refractive index $n_{SiO_2} = 1.4504$ (by Malitson 1965), respectively. The cavity is made of same material as low refractive index material of DBR. The following dimensions are used in the geometrical model: the period of lattice $a = 500$ nm, thickness of TiO_2 layers $h_L = 108.052$ nm, and thickness of SiO_2 layers $h_H = 172.3662$ nm. The length of the cavity for selected resonant wavelength is found to be equal to $L_{cav} = 516.5$ nm. This value does not correspond to the value from Eq. (4.27). For the longitudinal mode numbers $q = 1$, and $q = 2$, the cavity length is equal to 344.7 nm, and 689.5 nm, respectively. Note that, this equation holds for the mirrors with the indefinitely thin mirrors, while in this case, DBRs have some finite length. It seems that "effective" location of the mirrors is not at the inner edge of DBR mirrors but somewhere inside the DBR. The design cavity length is the closest to the value corresponding to the longitudinal mode number $q = 2$. Fig. 4.11 (d) illustrates the isometric view of the same geometrical model.

The second simulated geometrical model of the FP filter is depicted in Fig. 4.11 (c). The geometry of DBRs is same as in the previous model, while the cavity is modified. The amorphous silicon ($a-Si$) elliptic cylinder, with refractive index $n_{a-Si} = 3.6392$ (by Pierce and Spicer 1972) is embedded inside the cavity, as a birefringent metasurface. Because the material with the higher refractive index is inside the cavity, the length of the cavity should be shorter to get same resonant wavelength. For the diameters of ellipse $D_x = 100$ nm, $D_y = 400$ nm, and the height of the elliptic cylinder $h_c = 200$ nm, this corresponds to cavity length of $L_{cav} = 466.5$ nm. The presence of birefringent metasurface inside the cavity will result in different phase shift for the two orthogonal polarizations. As a consequence, the resonant wavelengths will be different for the orthogonal polarizations. This can be interpreted as different effective cavity length depending on the polarization of the incident light. Fig. 4.11 (b) illustrates the isometric view of the same geometrical model, where can be seen the elliptic cylinder inside the cavity.

In Fig. 4.12 (a), the results of simulation are shown. First of all, the reflectance (defined as $R = 1 - T$) of single DBR, which represents the mirror of the FP filter is denoted as the blue area on the plot. It shows how the reflectance changes over the spectrum. The DBR consists of 6 pairs of layers, designed for resonant wave-

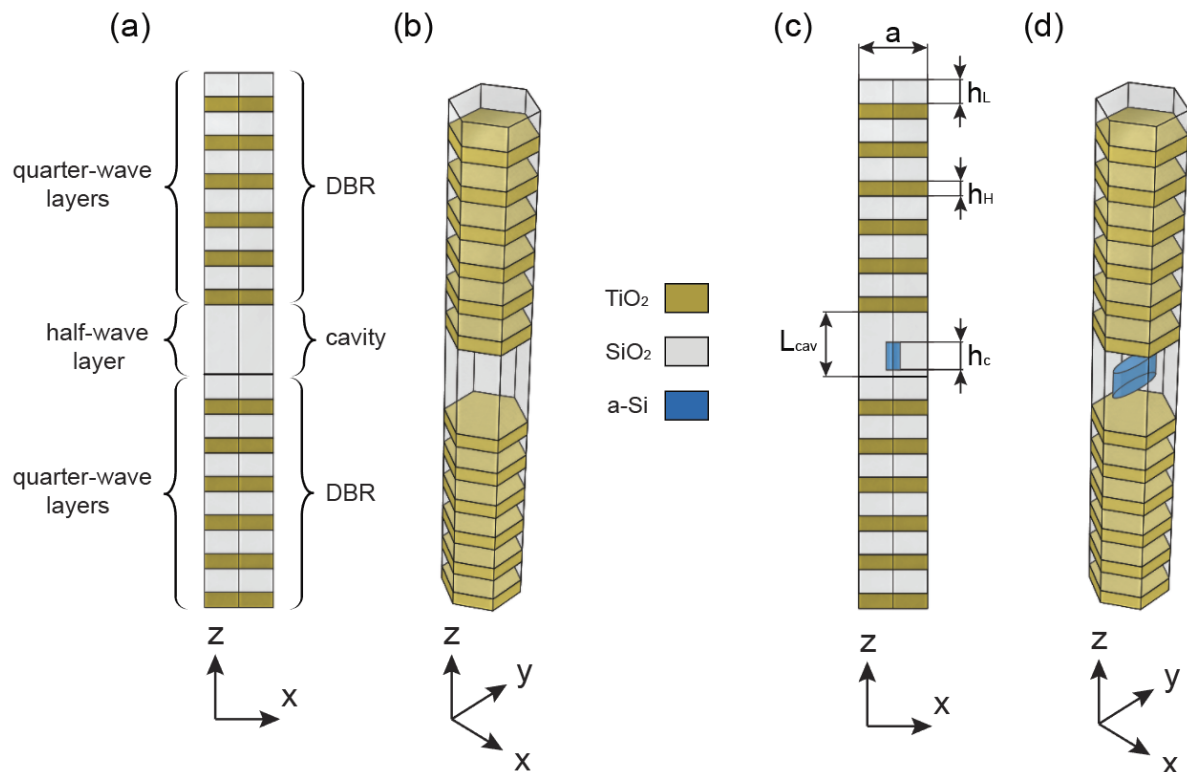


Figure 4.11: (a) Front view of the geometrical model of the unit cell of a FP cavity formed by two DBR mirrors consisted of 6 pairs of layers. The selected materials of the high and low refractive index of DBR are TiO_2 , and SiO_2 , respectively. The cavity is made of same material as low refractive index material of DBR. The following dimensions are used in the geometrical model: the period of lattice is $a = 500$ nm, thickness of TiO_2 layers $h_L = 108.052$ nm, thickness of SiO_2 layers $h_H = 172.3662$ nm, length of the cavity $L_{cav} = 516.5$ nm. (b) Isometric view of same geometrical model. (c) Front view of the same geometrical model as in the previous model with the addition of embedded $a-Si$ elliptic cylinder inside the cavity. The following dimensions are used in the geometrical model: the period of lattice is $a = 500$ nm, thickness of TiO_2 layers $h_L = 108.052$ nm, thickness of SiO_2 layers $h_H = 172.3662$ nm, length of the cavity $L_{cav} = 466.5$ nm, the height of the elliptic cylinder $h_c = 200$ nm, the diameters of ellipse $D_x = 100$ nm, and $D_y = 400$ nm. (d) Isometric view of the FP cavity with the embedded $a-Si$ elliptic cylinder.

length $\lambda = 1000$ nm. Also, on the same plot, the transmittance vs. wavelength of the FP filter geometry in Fig. 4.11 (a) is shown, for two orthogonal polarizations. The resonant narrow transmittance peak is located at $\lambda = 1000$ nm. The main disadvantage of the DBR is limitation over finite wavelength region. It can be noticed that for this particular example, the values of reflectance of DBR are limited to spectral range approximately from 900 nm to 1100 nm. As a consequence, transmittance sidebands appear on either side of the peak, which must be suppressed. In the visible and near infrared regions, the sidebands can be filtered out by adding additional longwave-pass absorption filter.

In Fig. 4.12 (b), the result of transmittance vs wavelength for three different numbers of layer pairs of DBR (for 6, 5, and 4 pairs) of FP filter is shown. In this case, the cavity height is not changed. The DBR with more layer pairs have higher reflectivity of the mirror (according to Eq. (4.30)), and therefore narrower transmittance peak. The number of layer pairs is an important parameter for spectral resolution. The selected number of layer pairs is 6, which results in a spectral resolution of less than 4 nm (Requirements list, Subsection 2.4).

By embedding the array of elliptic cylinders (Fig. 4.11 (c)) into the FP cavity, it is possible to design a pleochroic spectral filter. Pleochroism is an optical phenomenon in which a substance has different colors when observed at different angles, especially with polarized light. [45] This phenomena occur in anisotropic crystals, where optical properties vary with the direction of light. The direction of the electric field determines the polarization of light, and crystals will respond in different ways if this angle is changed. In a similar way as natural crystals, anisotropy can be created artificially with metasurfaces consisting of an array of asymmetric

nanostructures, for example, elliptic cylinders. In Fig. 4.13 is shown how different aspect ratios (while keeping same cross-section area) of elliptic cylinders affect the central wavelengths for two polarization orientations. It can be seen that in the case of aspect ratio (AR) equal to 1, the transmittance of two orthogonal polarizations overlaps (at $\lambda = 1000$ nm). As the AR of nanostructures increases the shift of central wavelengths for two orthogonal polarization moves apart from the initial wavelength of 1000 nm ($AR = 1$). The location of the central wavelength can be tuned by changing the AR and/or cross-section area of the nanostructures.

By proper tuning of diameters of the ellipse, the central wavelengths can be arranged uniformly one next to each other in order to cover some finite spectral band with a high spectral resolution (see Fig. 4.14). The effect of pleochroism is used to simultaneously design narrow band spectral filter, and to filter out only one orientation of polarization (as a linear polarizer). Since for each pleochroic FP, two peaks of the spectrum are transmitted, it is necessary to pass through only one direction of polarization. This can be achieved by putting a broad band spectral filter, as shown in Fig. 4.14. In this example, the central peaks oriented in x direction polarizations are allowed to pass. The spectral information is measured by making an array of pixelated FP filters with a uniform distribution of central wavelengths along the detector array.

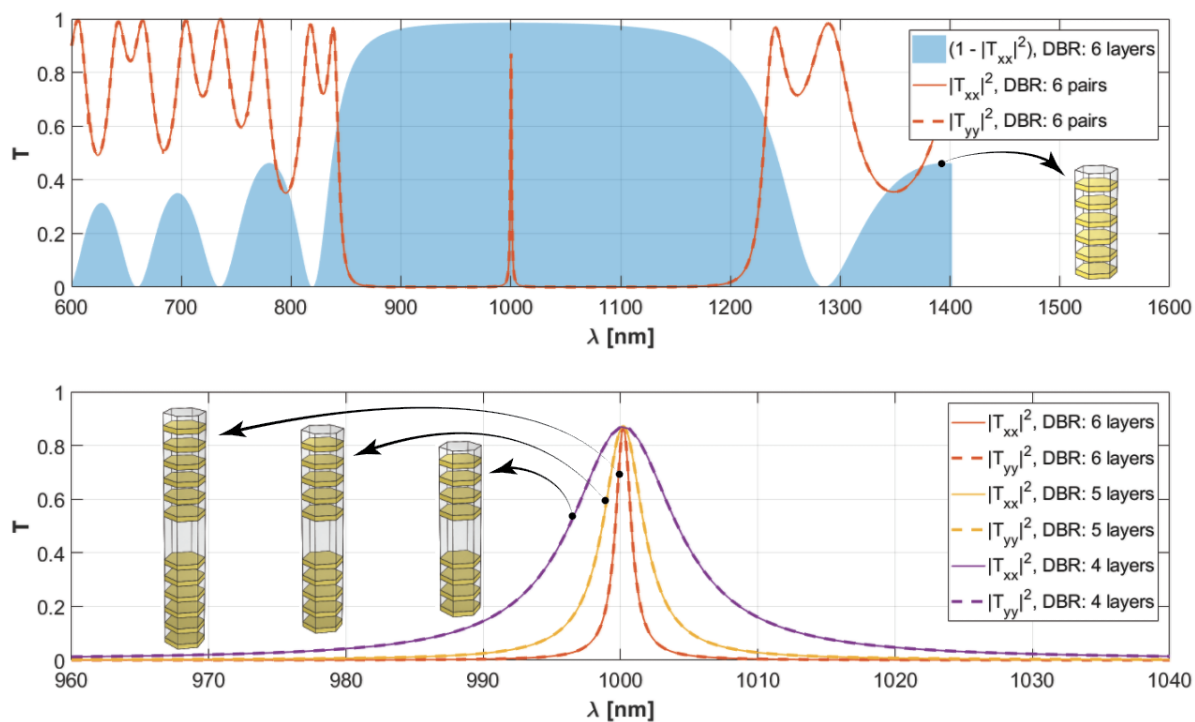


Figure 4.12: (a) The blue area represents reflectance of simulated DBR mirror consisted of 6 layer pairs. Furthermore, the red solid and dashed line represents transmittance vs wavelength for the FP filter consisted of 6 layer pairs of DBR. Resonant wavelength is located at 1000 nm. (b) FP filter: transmittance vs wavelength for 6, 5, and 4 pairs of layers of DBR.

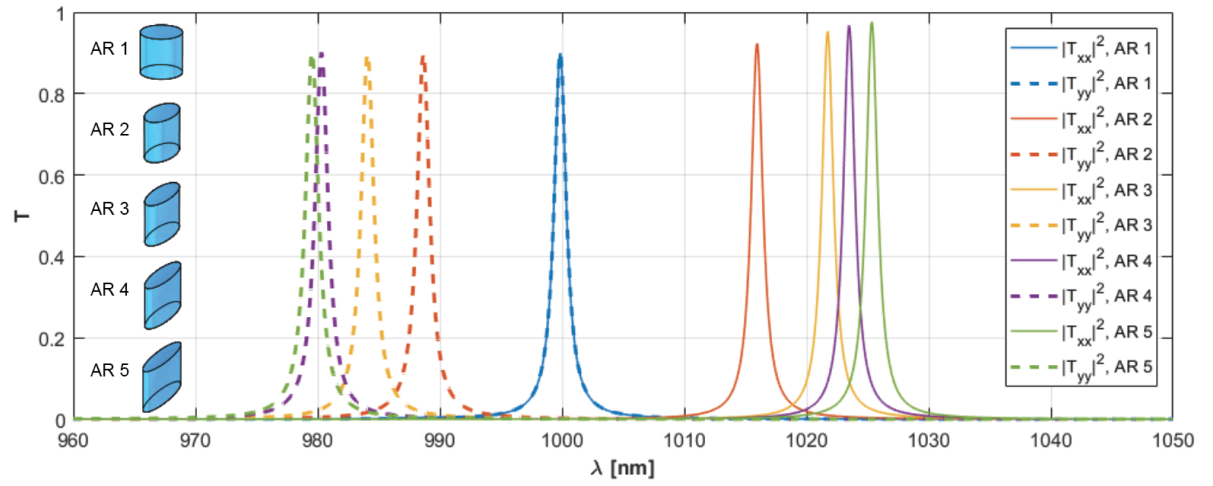


Figure 4.13: Transmission vs. wavelength for simulated DBR with 6 pairs of layers, with embedded $a-Si$ elliptic cylinder inside the cavity. Pleochroic Fabry-Pérot filters for different aspect ratio of the ellipse show shift in central wavelengths for two orthogonal polarizations

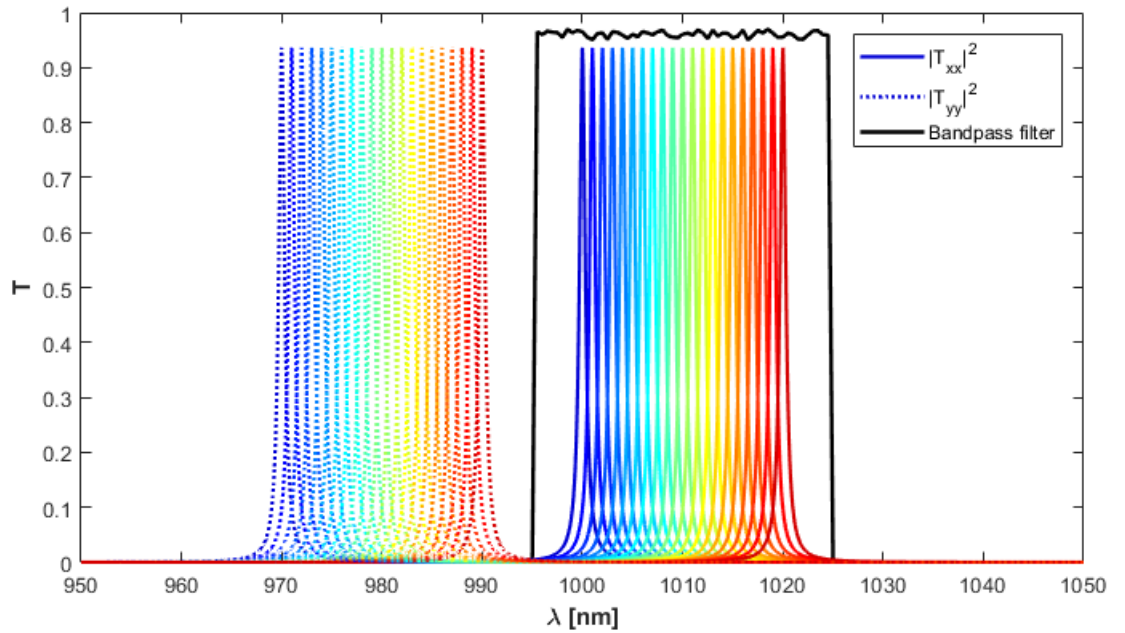


Figure 4.14: Uniformly distributed pleochroic FP filters with their center wavelengths stacked periodically in order to cover the finite spectrum with high spectral resolution. The broadband filter is implemented to allow measurement of transmitted peaks of only one orientation of polarization (T_{xx} in this case). In this plot are shown 20 different spectral bands from 1000 to 1020 nm, with a period of 1 nm. The shift in central wavelengths between two orthogonal polarizations is 30 nm. Note that, this is not the result of simulation, but only illustration of the concept.

5

DESIGN ANALYSIS

In this chapter, the selected spectropolarimeter design is analyzed. The important parameters like spatial resolution, spectropolarimetric resolution, transmission efficiency over the spectrum, and performance of the complete system are estimated. This also includes sensitivity analysis due to fabrication tolerance. In the end, the estimated parameters are compared with the reference instrument, and overall outlook of the instrument is shown.

5.1. SPATIAL RESOLUTION

In this section, the required parameters for signal-to-noise estimation, related to spatial resolutions are calculated. Some of the parameters can be derived from the requirements. The image sensor used in [29] is a 2k x 2k CMOSIS CMV4000 CMOS image sensor. It is consisted of 2048 x 2048 pixels, with pixel size of $5.5\mu m$ x $5.5\mu m$.

$N_h = 2048$, number of pixels in horizontal direction [29]

$N_v = 2048$, number of pixels in vertical direction [29]

$H = 675.5$ [km], nominal altitude of the satellite in low Earth orbit [25]

$S_w = 100$ [km], swath width [29]

$S_r = 2$ [km], required spatial resolution for polarization

$r_{\oplus} = 6378.1$ [km], radius of the Earth

The field of view (FoV) defines a solid angle that an instrument can observe (Fig. 5.1). It can be estimated from swath width and orbit altitude:

$$FoV = \frac{S_w^2}{H^2} = 0.0219 \text{ [sr]} \quad (5.1)$$

The ground sample distance (GSD) at nadir can be estimated by knowing the swath width and the detector layout (N_h and N_v).

$$GSD \approx \frac{S_w}{N_h} = 0.05 \text{ [km]} \quad (5.2)$$

The instantaneous field of view (IFoV) is defined here as a solid angle of a single detector pixel of the detector array:

$$IFoV = \frac{GSD^2}{H^2} = 5.4788 \times 10^{-9} \text{ [sr]} \quad (5.3)$$

The most convenient technique used in remote sensing is a push-broom, which requires no moving parts. The required integration time of each pixel in order to achieve a spatial resolution length of 2km is calculated from GSD and ground track velocity of the orbit. The ground track velocity of this orbit can be approximated as:

$$V_g \approx \frac{r_{\oplus}}{a} \sqrt{\frac{\mu_{\oplus}}{a}} \quad (5.4)$$

where μ_{\oplus} is the Earth's standard gravitational parameter, and a is defined as:

$$a = r_{\oplus} + H \quad (5.5)$$

Then the integration time is calculated from the required spatial resolution and velocity at the ground:

$$t_{int} = \frac{S_r}{V_g} = 0.2942 \text{ [s]} \quad (5.6)$$

The values of $IFOV$, and t_{int} are used later for signal-to-noise calculation.

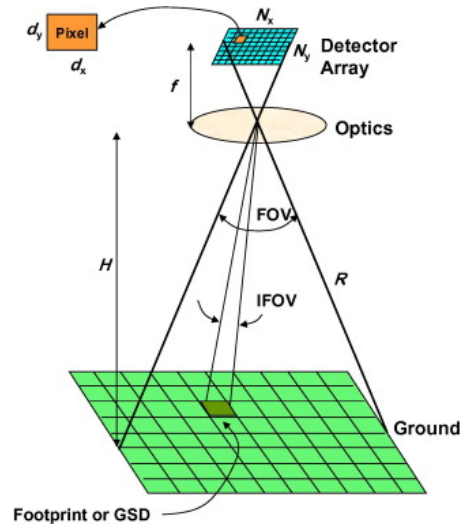


Figure 5.1: Definition of the important parameters used in this chapter. [12]

5.1.1. OPTICAL DESIGN OPTIONS

In general, the optical design can be differentiated in two categories: the telecentric lenses and non-telecentric lenses. Furthermore, the telecentricity can be divided into object space and image space telecentricity. An object space telecentric lens has the entrance pupil located at infinity in image space (the chief rays are all parallel to the optical axis in object space). This type of lenses are usually used in machine vision. An image space telecentricity is defined by the exit pupil located at infinity in object space (the chief rays are all parallel to the optical axis in image space), as shown in Fig. 5.2.

The image space telecentric lenses are interested when the filters are used in the image plane. This is because the rays land perpendicular to the sensor across its entire area. The image has a more uniform relative illumination profile. Telecentric lenses are used with image sensors that do not tolerate a wide range of angles of incidence. Because of the sensitivity of Fabry-Pérot filters on the angle, this concept simplifies the design of such filters. With the telecentric lens, the focused beam on the detector is impinging normally, with the beam forming a certain cone angle. Further analysis of the focused beam on the FP filters is discussed in Section 5.2.1. The disadvantage of this type of lenses are additional elements to achieve telecentricity, and they can grow quite large in diameter depending on the sensor size that is being used.

The significant parameter in designing an optical subsystem is a spatial resolution limitation due to the diffraction of an aperture. The diffraction pattern resulting from a uniformly illuminated circular aperture has a bright central region called airy disk, with a series of concentric rings around it. The smallest point to which a lens can focus a beam of light due to the diffraction (Fraunhofer diffraction model) is the size of the airy disk with diameter, d_{airy} :

$$d_{airy} = 1.22 \left(\frac{\lambda f}{d_{ap}} \right) \quad (5.7)$$

where f is the focal plane (Fig. 5.1), d_{ap} is the diameter of the aperture.

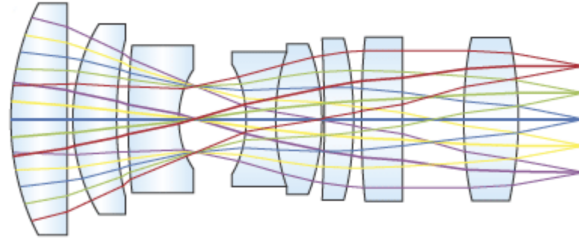


Figure 5.2: An image space telecentric lens, where the chief rays are all parallel to the optical axis in image space. Note that the image height does not change regardless of where the sensor plane is positioned, as the chief rays defining image height are all parallel to the optical axis. [13]

The f-number is defined as:

$$N_f = \frac{f}{d_{ap}} \quad (5.8)$$

In optics, the numerical aperture (NA) of an optical system is a dimensionless number that characterizes the range of angles over which the system can accept or emit light.

$$NA = n \sin(\theta_0) \quad (5.9)$$

where n is the refractive index of the medium in which the lens is working (1 for vacuum), and θ_0 is maximum half cone angle of the focused light beam that can enter the lens.

The relation between f-number and numerical aperture, NA :

$$N_f = \frac{1}{2 NA} \quad (5.10)$$

By selecting the diameter of airy disc equal to the length of the superpixel (2x2 pixels), which is equal to $11 \times 11 \mu\text{m}$, and wavelength equal to 600 nm (as midpoint from requirements, Table 2.1), the f-number is equal to $N_f \approx 15$ ($NA = 0.0333$). Furthermore, for this NA , the half cone angle is equal to $\theta_0 = 1.9$ deg. For focal length of $f \approx 0.15$ m this results in aperture diameter of $d_{ap} \approx 0.01$ m, and therefore aperture area $A_{ap} = 7.854 \times 10^{-5} \text{ m}^2$. The condition that the airy disc corresponds to the superpixel size is implemented in order to reduce the effect of polarization aliasing (different states of polarization impinging on different pixels of the superpixel).

5.2. SPECTROPOLARIMETRIC RESOLUTION

The purpose of this section is to estimate spectral resolution for polarimetry. Since the previous simulations were conducted for a normal incident plane wave, there is a need to estimate the real response of the surface when illuminated by the focused beam instead of a plane wave.

5.2.1. PLANE WAVE'S SUPERPOSITION DUE TO FOCUSED BEAM

This subsection deals with an impact of different incident angles of plane waves and focused beam of light on the transmittance of FP filters.

In Fig. 5.3 (a) is graphical illustration of the FB filter with the definition of the incident plane wave angle θ_0 . Fig. 5.3 (b) shows results of transmittance (x polarized, $|T_{xx}|^2$) of 6 pair DBR FP filter with embedded $a - Si$ elliptic cylinder with aspect ratio 4 inside the cavity (see Fig. 4.13) for five different incident angles of plane waves, θ_0 . In Fig. 5.3 (c) are shown contour maps of transmittance for x and y polarization orientation as function of incident angle, θ_0 and wavelength, λ . It can be seen that by increasing the incident angle the peak of the transmittance shifts to the shorter wavelengths. Since the incident beam is not a plane wave but a cone of light, focused by the lens, it is necessary to estimate the impact of focused beam on transmittance.

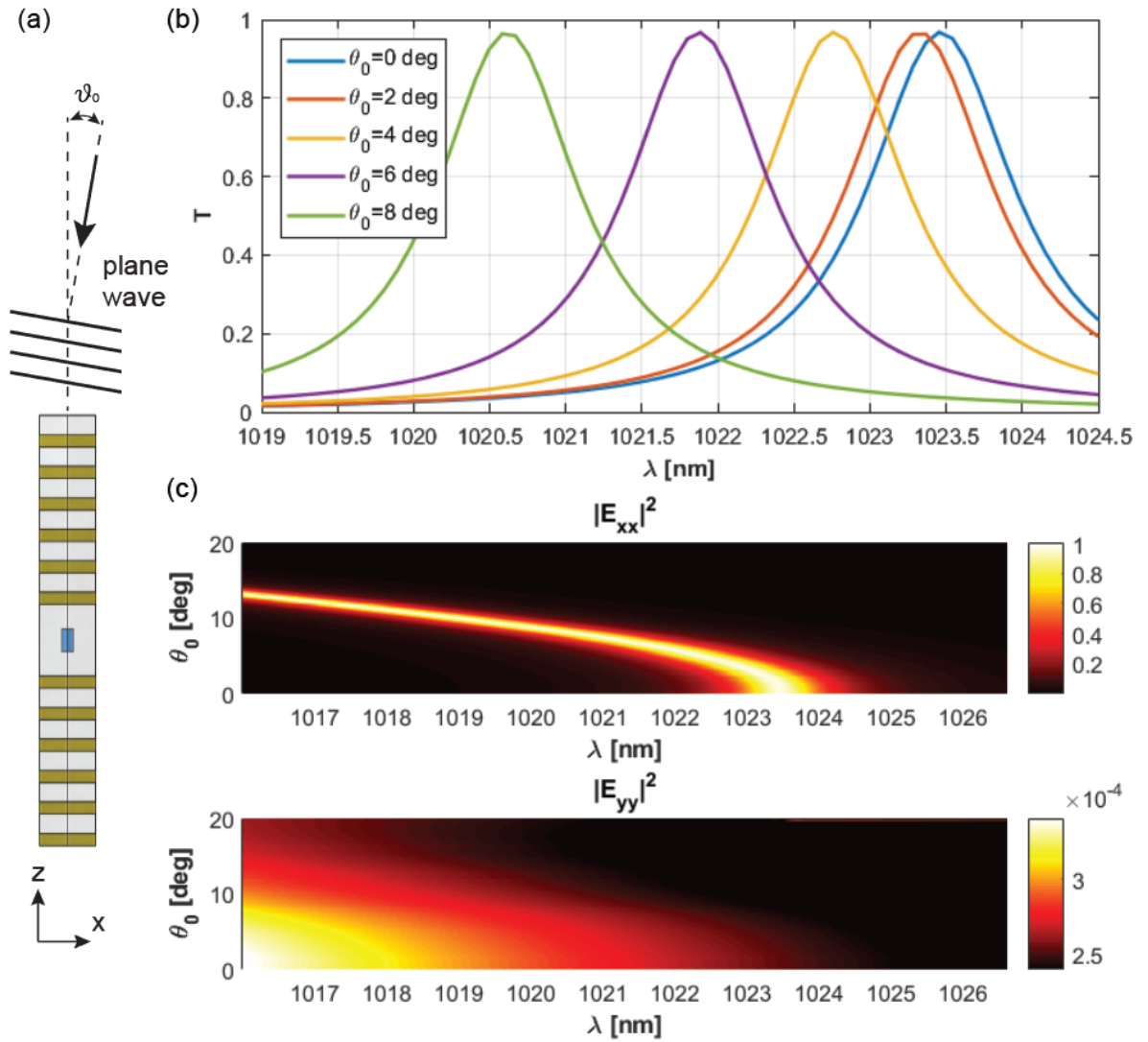


Figure 5.3: (a) Graphical illustration of the FB filter with the definition of the incident plane wave angle θ_0 . (b) Result of simulation of FP filter. Transmittance vs wavelength diagram, for different incident angles of plane waves. The used geometrical model in simulation is from Fig. 4.13, AR=4. The transmittance correspond to x polarization orientation ($|T_{xx}|^2$). The used geometrical model in simulation is from Fig. 4.13, AR=4. The transmittance correspond to y polarization orientation ($|T_{yy}|^2$).

A focused beam can be modeled by superposition of plane waves at different angles. That allows an estimation of the filter response under focused beam. From [3], for small values of θ_0 (approximation: $\theta_0 \approx \sin(\theta_0)$), the incident flux on the filter is proportional to $\theta_0 d\theta_0$. The flux as a function of wavelength can be approximated by integrating the transmittance of the filter for different incident angles of plane waves:

$$T_\lambda = C \int_0^\Theta \theta_0 T_\lambda(\theta_0) d\theta_0 \quad (5.11)$$

where Θ is maximum half cone angle of the light, and $T_\lambda(\theta_0)$ is the transmittance of the filter for particular incident plane wave angle, θ_0 . C is the scale factor used to keep the total incident flux constant for different simulations of half cone angles.

In Fig. 5.4 (a) schematically illustrates the definition of half cone angle of the focused beam, Θ impinging normally on the FP filter. In Fig. 5.4 (b) are shown results of transmittance for the incident cone of light with

four different half cone angles, Θ .

The spectral resolution is defined as full width at half maximum (*FWHM*). It can be seen in Fig. 5.4 (b) that for small half cone angle, $\theta_0 = 2$ deg (which is close to the required value calculated in Subsection 5.1.1) the *FWHM* is almost equal as for the plane wave, $FWHM = 1.1$ nm. Therefore, for this specific configuration, the spectral resolution is about $\Delta\lambda = 1.1$ nm. For larger half cone angles, Θ impinging normally on the FP filter three effects occurs [3]:

- Blue-shifted center wavelength
- Reduction in transmittance peak
- Broader transmittance (*FWHM*)

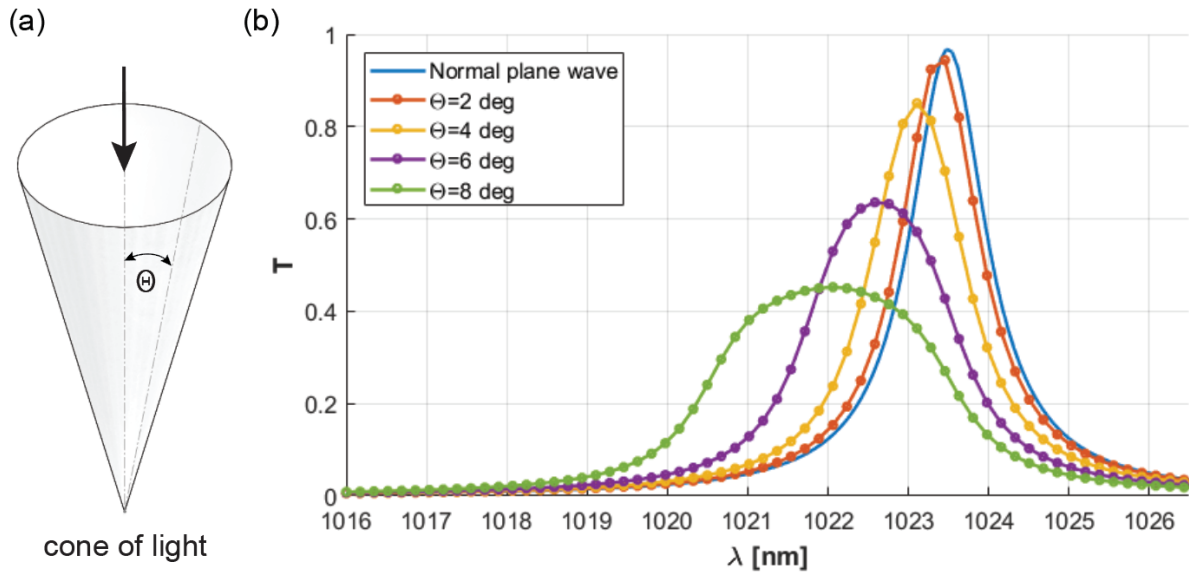


Figure 5.4: (a) Schematic illustration of half cone angle of the focused beam, Θ impinging normally on the FP filter. (b) Transmittance ($T_{xx}|^2$) vs wavelength for the plane wave and four half cone angles, Θ . The used geometrical model for simulation is from Fig. 4.13, AR=4. For the plane wave and $\Theta = 2$ deg, the spectral resolution is about $FWHM = 1.1$ nm.

5.3. TRANSMITTANCE OVER THE SPECTRUM

In this section, the efficiency in terms of transmittance of FP filters over the spectrum is analyzed. Two different types of inclusions inside the cavity are considered. The first type is an array of $a-Si$ elliptic cylinders, and the second is TiO_2 sub-wavelength grating. In both cases DBR mirrors are consisted of TiO_2 and SiO_2 layers. These two types of simulated structures are shown in Fig. 5.5 (a) and (b). Fig. 5.5 (c) shows estimated transmittance for three simulated wavelengths: 1000, 895, and 791 nm. The simulated geometrical model (from Fig. 4.13) is DBR FP filter consisted of 6 pairs of layers, with an embedded array of elliptic cylinders made of $a-Si$. As can be seen at the wavelength of 895 nm, the transmittance is already low as 33%. Therefore, the operational range of wavelengths for the $a-Si$ is in the range from 900 to 1600 nm. The reason for that is a lossy nature of this material.

Fig. 5.5 (d) shows the transmittance for the geometrical model with embedded TiO_2 subwavelength grating inside the cavity. Three wavelengths are simulated: 796.8, 589.1, and 401.6 nm. With this configuration, the transmittance starts to drop about 400 nm with its value of about 39%. This material enables the operating range in the whole visible spectrum.

The rapid decrease in transmittance can be explained by analyzing the refractive index over the spectrum

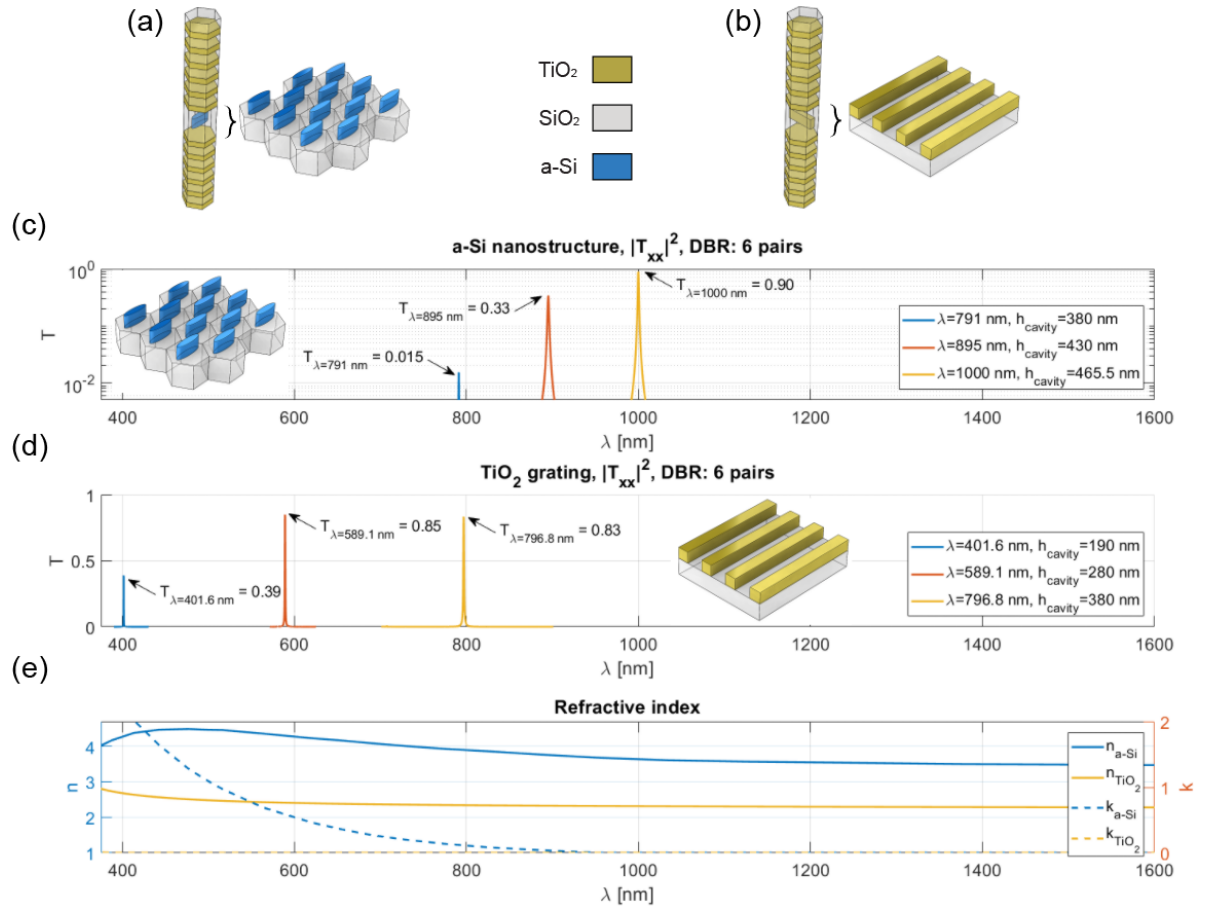


Figure 5.5: (a) Simulated structure with an array of $a-Si$ elliptic cylinders embedded inside the FP cavity. (b) Simulated structure with a TiO_2 sub-wavelength grating embedded inside the FP cavity. (c) The transmittance of the FP filters with an array of $a-Si$ elliptic cylinders embedded inside the cavity for three simulated wavelengths: 1000, 895, and 791 nm. (d) The transmittance of the FP filters with a TiO_2 sub-wavelength grating embedded inside the cavity for three simulated wavelengths: 796.8, 589.1, and 401.6 nm. (e) Refractive index vs wavelength for $a-Si$, and TiO_2 (real part n , and imaginary part k)

for the aforementioned materials. Fig. 5.5 (e) shows real part of refractive index n and imaginary part of refractive index k as function of wavelength. The imaginary part of $a-Si$ refractive index becomes substantial for wavelengths lower than 1000 nm. Similar behavior can be seen for TiO_2 at 400 nm. Note that TiO_2 DBR layers are also becoming lossy for wavelengths shorter than 400 nm, which results in the faster decline in the transmittance.

The maximum observed shift in transmittance peaks for two orthogonal polarizations is about ≈ 30 nm at $\lambda = 400$ nm, and ≈ 45 nm at $\lambda = 1000$ nm (see Fig. 4.13 for $AR = 4$). For $a-Si$ subwavelength gratings embedded inside the FP cavity at $\lambda = 1600$ nm, this shift is larger than 100 nm. For this specific concept, this maximum shift in transmittance peaks for two orthogonal polarizations indicates maximum spectral bandwidth.

An alternative for $a-Si$ could be crystalline silicon ($c-Si$). In [46] is shown that high transmission efficiency ($> 60\%$) in the visible spectrum is achievable with crystalline silicon ($c-Si$) elliptic cylinders, which operates as birefringent metasurfaces. However, for the FP filters, due to the resonant nature of such structures, the decrease in efficiency is more significant.

5.4. FABRICATION TOLERANCE

The purpose of this section is to assess how the uncertainty in fabrication is linked to spectropolarimetric performances. In the first subsection is shown how the uncertainty of fabrication impacts the performance of birefringent metasurface, operating as a waveplate. The second subsection deals with an impact on the spectral performance of the FP filters.

Photolithography, electron-beam lithography, and focused-ion-beam lithography are the conventional surface-lithography technologies for patterning nanostructures. For the fabrication of metasurfaces, the choice of fabrication technique should consider the inherent advantages and disadvantages of these technologies that satisfying the process requirements, such as resolution, throughput, reliability, reproducibility, and cost efficiency. Photolithography is the most widely used fabrication technology in semiconductor integrated circuits with high throughput at the micro and nanoscale. The patterns are transferred from photomasks to photoresists after the exposure and development steps. After the etching, depositing, and lift-off process, nanostructures are formed on the substrates. Electron-beam lithography is a maskless system capable of directly drawing arbitrary patterns with several nanoscale featured sizes. In addition, the focused-ion-beam technique is also a straightforward versatile nanofabrication method by removing and depositing the materials in one step. [9]

In [46] is reported nanofabrication resolution of 20 nm. The fabricated metasurfaces suffer from semi-axis size deviations of their elliptic cylinders. Because of that, the phase shift of metasurface deviates from the desired values. The development of lithography in semiconductor fabrication shown very rapid advance over the years. For instance, in the last 20 years, the smallest features that can be fabricated moved from around 180 nm in the year 1999 to 10 nm in the year 2018. [47] Therefore, the current fabrication tolerance can be assumed somewhere between 10 and 20 nm.

5.4.1. IMPACT ON METASURFACE AS WAVEPLATE

The simulation sweep of an array of elliptic cylinders on the SiO_2 substrate (simulated unit cell is shown in Fig. 4.7 (a)) is done for the range of ellipse diameters D_x from 80 to 200 nm, and D_y from 170 to 290 nm, with a step of 2 nm. The height of the cylinder is the same for all simulations, equal to 600 nm. The wavelength of the simulations is $\lambda = 1023.4$ nm, which corresponds to the center wavelength of the FP filter for $AR = 4$ (Fig. 4.13). In Fig. 5.6 (c) and (d) are shown contour maps (as a function of ellipse diameters D_x and D_y) of the transmittance for x and y polarization directions, respectively. Fig. 5.6 (e) represents the contour map of the subtraction between transmittance in x and y polarization directions, which is an indication of unequal transmittance. Lastly, Fig. 5.6 (f) shows the contour map of the retardance, $\delta = \delta_x - \delta_y$. Also, four marker points are indicated on all of four contour maps. The marker points, triangle pointing down ($D_x = 108$ nm, and $D_y = 244$ nm), and triangle pointing up ($D_x = 160$ nm, and $D_y = 184$ nm) correspond to the closest retardances that are optimized in Table 4.2. The down-pointing triangle marker represents $\delta = 60.71$ deg, and the up pointing triangle marker represents $\delta = 14.25$ deg. These two points are selected (optimized) in such a way that the difference in the transmittance is closest to the 0 (as shown in Fig. 5.6 (e)). These two points represent the best case or the performance that is closest to the optimized waveplates. Furthermore, the black dots around those two markers points are the diameters of ellipse inside the tolerance of the fabrication (here used ± 6 nm). The other two marker points, the triangle pointing to the right ($D_x = 114$ nm, and $D_y = 250$ nm) and to the left ($D_x = 166$ nm, and $D_y = 190$ nm), represent worst case inside the tolerance range, where the difference in transmittance is the worst. Note that the height of the cylinder is assumed constant for all simulations.

By conducting random sampling of these diameters inside the tolerance range, it is possible to simulate how the performance of the whole system changes with this uncertainty. The effect of the deviation in the retardance due to the tolerance uncertainty on condition number, CN is analyzed (see subsection 4.2.1). In this analysis, the ideal components of waveplate and linear polarizers are considered. Fig. 5.7 (a) shows how the condition number (CN) changes as a function of randomly sampled diameters of the ellipse (resulting in different retardance, δ), and also randomly sampled orientation angles (fast axis) of the waveplates, α . The assumption for the tolerance on orientation angle of the ellipse is ± 1 deg. From the results can be seen that CN ranges from approximately 1.8 to 2.2. The largest increase in CN is about 20%. Fig. 5.7 (b) depicts corresponding ideal four points of polarization modulation (shown as the blue tetrahedron), and red points show dispersion around these ideal points, due to the deviation of retardance and fast axis caused by fabrication

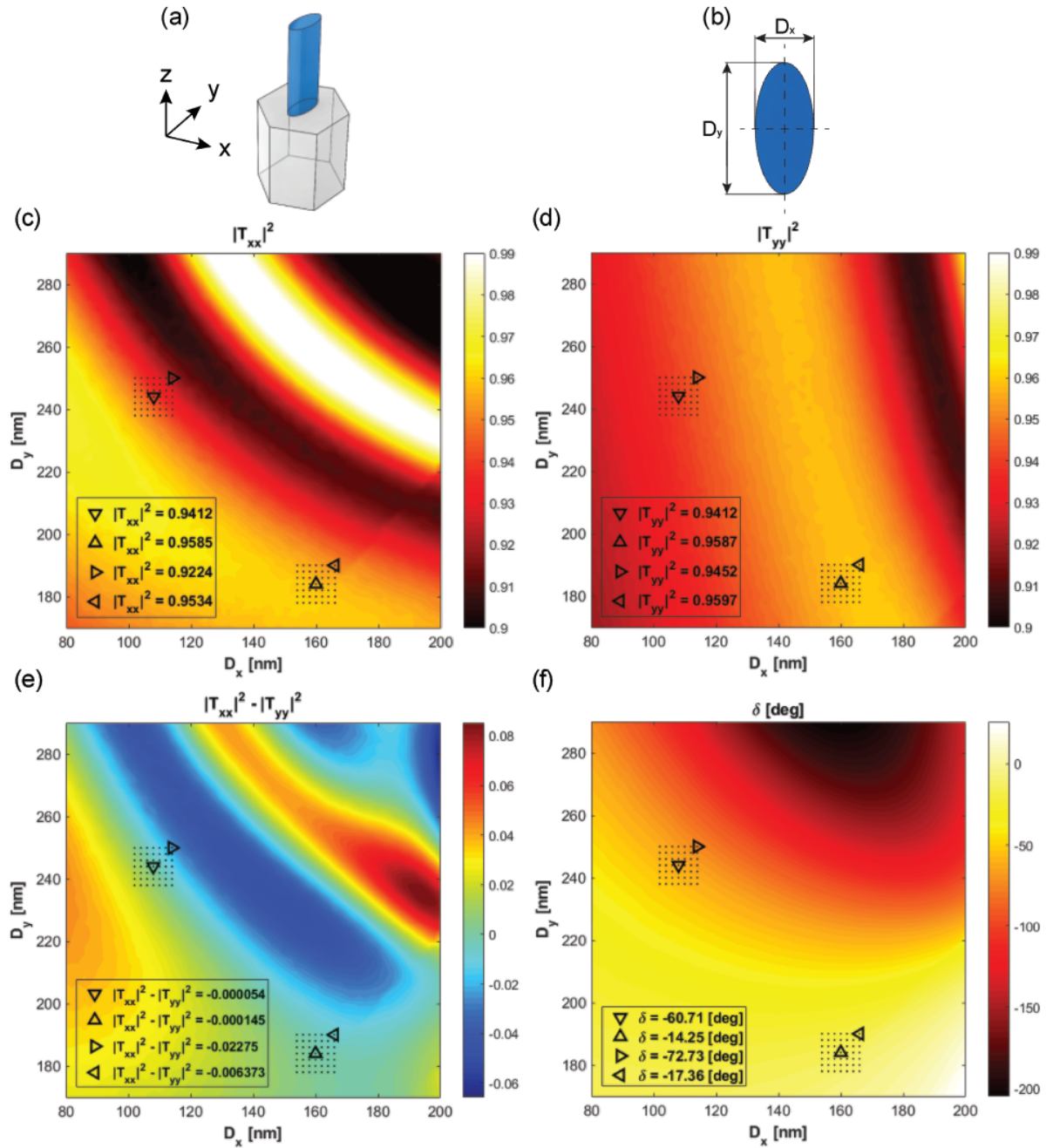


Figure 5.6: (a) Graphical illustration of the simulated unit cell of $a-Si$ elliptical cylinder on the SiO_2 substrate. (b) Top view, indicating diameters of the ellipse (D_x and D_y). (c) and (d) Contour maps (as a function of ellipse diameters D_x and D_y) of the transmittance for x and y polarization directions, respectively. (e) Contour map of the subtraction between transmittance in x and y polarization directions, which is indication of unequal transmittance. (f) Contour map of the retardance, $\delta = \delta_x - \delta_y$. The marker points with the shape of a triangle pointing down, and the triangle pointing up correspond to the closest retardances that are optimized in Table 4.2. The black dots around those two markers points are the diameters of ellipse inside the tolerance of the fabrication. The other two marker points, the triangle pointing to the right and to the left, represent worst case, where the difference in transmittance is the worst.

tolerance. Note that, in this simulation, analytical equations (ideal wave plate and linear polarizers) are used to calculate condition number and not results from simulation. This is because the point is to show how a change in retardance and fast axis individually impacts the performance.

In Table 5.1 is an overview of the parameters for the best and worst case due to the fabrication tolerance.

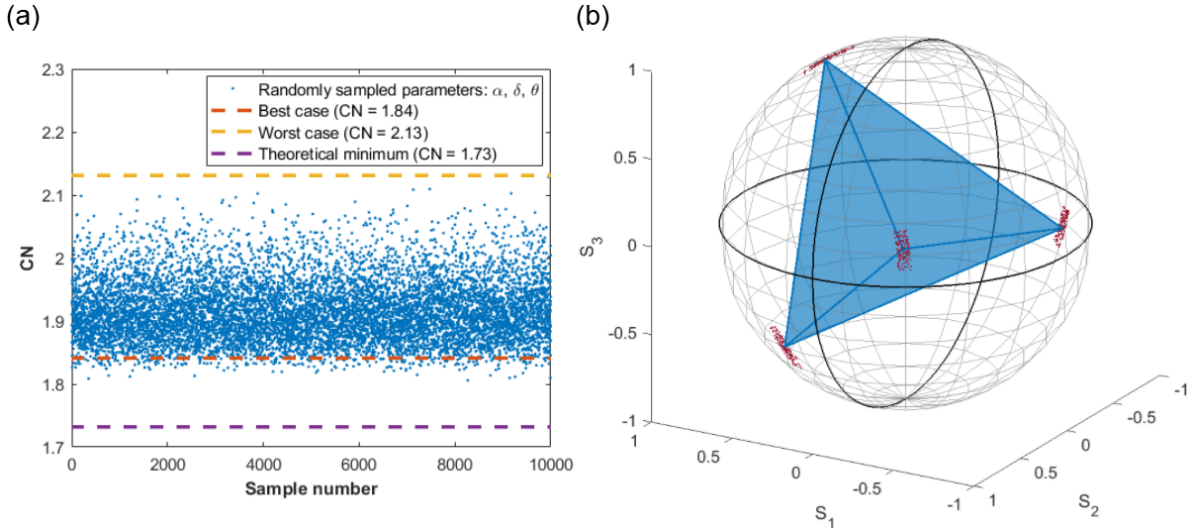


Figure 5.7: (a) CN vs. random sampling of diameters of the ellipse and fast axis. (b) Poincare sphere, where blue tetrahedron represents the ideal response of the four pixels, and the red dots are the result of random sampling, representing a deviation in polarization modulation due to fabrication tolerance.

For the first waveplate with a retardance of $\delta_1 = 60.71$ deg, the worst case is a shift of the retardance to the value of 72.73 deg. For the second waveplate with retardance of $\delta_2 = 14.25$ deg, this shift in retardance is smaller, equal to 17.36 deg (Fig. 5.6 (f)). In the same way, the larger unequal transmittance is observed for the first waveplate (Fig. 5.6 (e)). From this can be deduced that there exist "region" of elliptic cylinders where the fabrication tolerance has less impact on the performance. In order to find this region, a more extensive optimization is required, which also includes the initial design of four pixels (the values of retardance and fast axes for four pixels, see Table 4.2, Configuration 2).

Table 5.1: Overview of the parameters for the best and worst case. Values of angles are in degrees

	CN	Pixel A	Pixel B	Pixel C	Pixel D
		$\begin{bmatrix} \alpha_1 \\ \delta_1 \\ \theta_1 \end{bmatrix}$	$\begin{bmatrix} \alpha_2 \\ \delta_2 \\ \theta_2 \end{bmatrix}$	$\begin{bmatrix} \alpha_3 \\ \delta_3 \\ \theta_3 \end{bmatrix}$	$\begin{bmatrix} \alpha_4 \\ \delta_4 \\ \theta_4 \end{bmatrix}$
Best case configuration, waveplate with equal transmission	1.8392	$\begin{bmatrix} 60 \\ -60.71 \\ 0 \end{bmatrix}$	$\begin{bmatrix} 60 \\ -14.25 \\ 120 \end{bmatrix}$	$\begin{bmatrix} 120 \\ -60.71 \\ 0 \end{bmatrix}$	$\begin{bmatrix} 120 \\ -14.25 \\ 60 \end{bmatrix}$
Worst case configuration, waveplate with unequal transmission	2.131	$\begin{bmatrix} 60 \\ -72.73 \\ 0 \end{bmatrix}$	$\begin{bmatrix} 60 \\ -17.36 \\ 120 \end{bmatrix}$	$\begin{bmatrix} 120 \\ -72.73 \\ 0 \end{bmatrix}$	$\begin{bmatrix} 120 \\ -17.36 \\ 60 \end{bmatrix}$

5.4.2. IMPACT ON METASURFACE AS FABRY-PÉROT FILTER

In this subsection, an impact of fabrication tolerance on the second layer, the metasurface as FP filter is analyzed. Same as in previous subsection, the diameters of elliptic cylinder embedded inside the cavity are analyzed (Fig. 5.8 (a)). The analyzed wavelength used in the simulations is $\lambda = 1023.4$ nm, which corresponds to the center wavelength of the FP filter for $AR = 4$ (Fig. 4.13). For this particular design, the diameters of the ellipse are equal to: $D_x = 100$ nm, and $D_y = 400$ nm (Fig. 5.8 (b)). The error in diameters of the ellipse due to fabrication will cause a shift in center wavelength of the FP filter, while the value of transmittance is almost the same. The simulation sweep is done for a range of diameters: D_x from 90 to 110 nm, and D_y from 390 to 410 nm, with a step of 2 nm. The contour map of center wavelength (denoted as λ_c) can be seen in Fig. 5.8 (c) as a function of the ellipse diameters. Again, considering the same fabrication tolerance of ± 6 nm, the center

wavelength, λ_c ranges from a minimum value of $\lambda_{cmin} = 1019.9$ nm to a maximum value of $\lambda_{cmax} = 1028.4$ nm. Note that the height of the cylinder is assumed constant.

As a consequence of the uncertainty in fabrication, the placement of center wavelengths might not be as planned but rather shuffled. For this specific fabrication tolerance, the expected deviation in center wavelength, $\Delta\lambda_c$ is about ± 4 nm. This is illustrated in Fig. 5.9, where this figure serves only as a simulation of expected real design.

Therefore, the effect of the fabrication tolerance on the FP filter is only a shift in the center wavelength, but not the value of transmittance or polarization accuracy. That requires calibration of each individual pixel in order to find the real center wavelength. The assumption here is that other dimensions (like height) are not affected by fabrication. This is because the radial dimensions (diameters of the ellipse) are more critical than height.

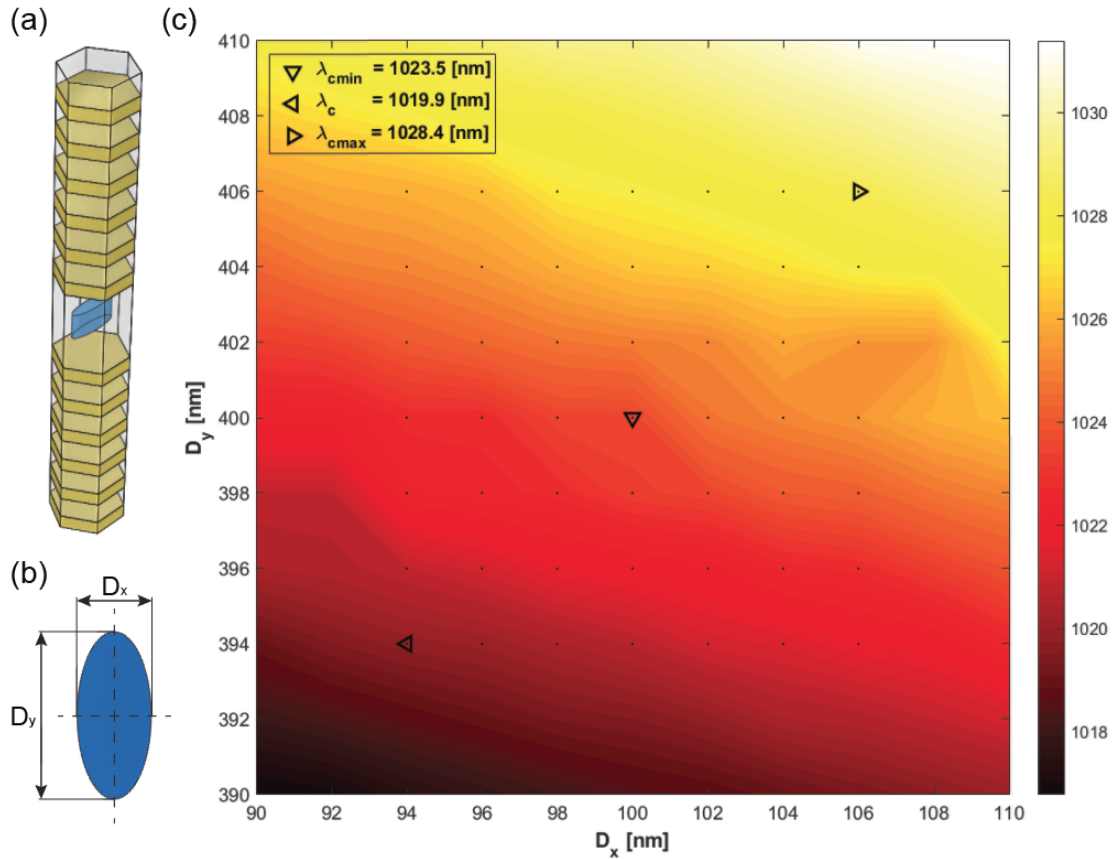


Figure 5.8: Contour map of center wavelength for different diameters of the ellipse. Black dots show region inside the tolerance range.

5.5. PERFORMANCE OF COMPLETE DESIGN (TWO LAYERED METASURFACE)

In this section, the two-layered structure consisted of the FP filter and the waveplate, which are previously discussed individually is analyzed. Those two layers are separated by a spacer made of SiO_2 . The FP filter in this simulation has $AR = 4$ of elliptic cylinder (Fig. 4.13), and the waveplate has diameters of ellipse: $D_x = 108$ nm and $D_y = 244$. This corresponds to **Pixel A**, with simulated unit cell graphically illustrated in Fig. 5.10 (a). The elliptic cylinder is placed on the top of the FP filter, separated by the spacer, with thickness t . In Fig. 5.10 (b), the result of simulation is shown. The transmittance is plotted as a function of the spacer thickness. Note that for different spacer thicknesses, the center wavelength shifts a little bit. Therefore, the result of transmittance for each spacer thickness corresponds to the center wavelength that is transmitted

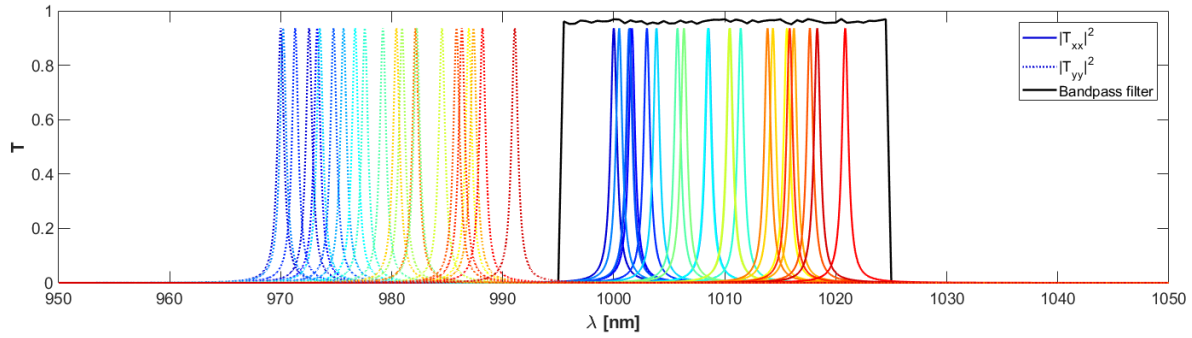


Figure 5.9: A simulation showing expected deviation in center wavelengths (due to the fabrication error) from a planned uniform coverage of the spectrum.

(around $\lambda_c = 1023.4$ nm). It can be noticed that Jones parameters T_{xx} and cross-polar oscillate periodically as a function of spacer thickness. The cross-polar T_{xy} is present due to the waveplate’s retardance. The possible explanation for the oscillation is an impact of different spacer thicknesses on the retardance of the waveplate. It seems that the effective height of the elliptic cylinder of the waveplate is affected by the spacer thickness, and as result an oscillation in retardance is present. Considering the response of the glass slab (made of SiO_2) individually (which is basically a Fabry-Pérot etalon with low reflectivity, and high transmission), a similar period of oscillations can be observed (Fig. 5.10 (c)).

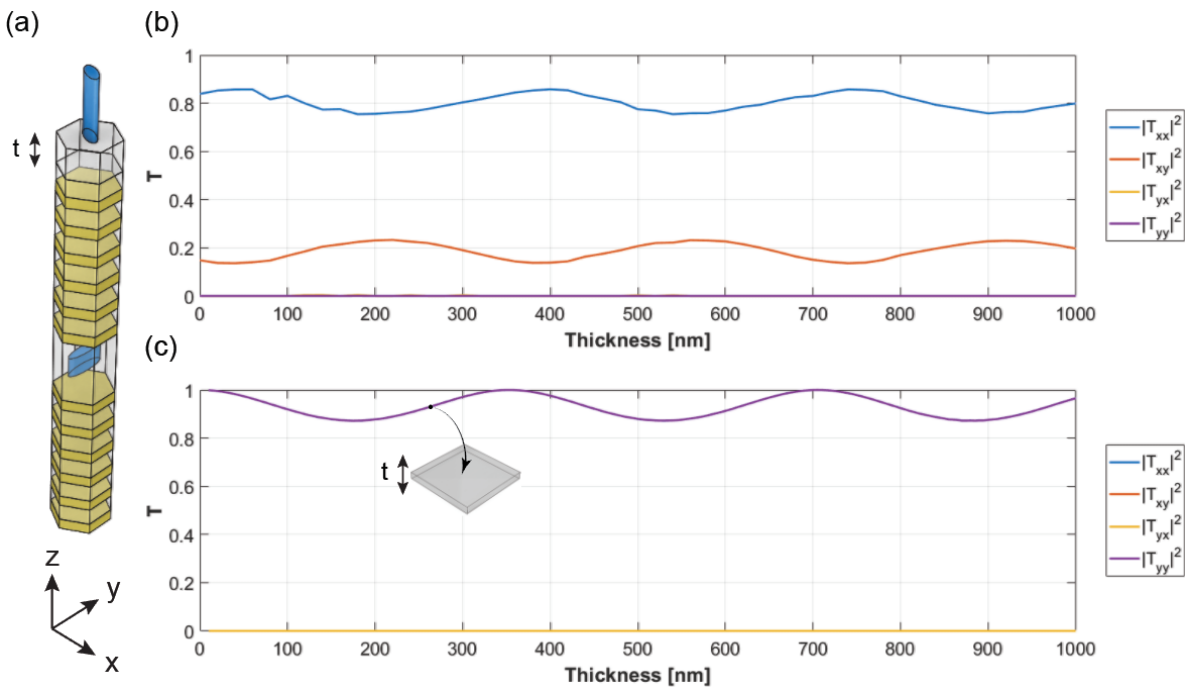


Figure 5.10: (a) Graphical illustration of the simulated unit cell with an elliptic cylinder placed on the top of the FP filter, separated by the spacer with thickness t (corresponding to **Pixel A**). (b) Transmittance vs spacer thickness diagram of **Pixel A**. (c) Transmittance vs spacer thickness diagram of a glass slab.

In Fig. 5.11 from (a) to (d) is the result of simulation for all four pixels, from A to D, respectively. In these diagrams are shown Mueller parameters, precisely the parameters of the first row of the Mueller matrix (M_{11} , M_{12} , M_{13} , M_{14}) instead of Jones parameters as a function of spacer thickness. Solid lines represent the results

of the simulation, while dashed lines are ideal (analytic) Mueller parameters for the best case configuration in Table 5.1. The ideal Mueller parameters are here normalized to have the same total intensity as result from simulation (M_{11} is the same for simulated and ideal). The values of ideal Mueller parameters are values for which the four pixels are optimized. The pixels A and C with a larger retardance of the waveplate shows the larger amplitude of oscillations as a function of the spacer thickness. Furthermore, the phase of oscillations for the pixels with larger retardance (pixels A and C) are not in the phase with oscillations for pixels with smaller retardance (pixels B and D). Also, the phase of oscillations of parameters M_{12} and M_{13} seems to be shifted by around $\pi/2$.

Because these oscillations are not in phase for all four pixels (for selected waveplates with retardances of 60.71 and 14.25 deg), there is no optimal spacer thickness which would result in zero error. However, the error in Mueller parameters could be minimized by analyzing total error of all four pixels. This can be calculated by summing up errors of each Mueller parameter for all four pixels:

$$E(M_{1i}) = \sum_{j=1}^4 |M_{1i,ideal,j} - M_{1i,sim,j}| \quad (5.12)$$

where $i = 1 : 4$ represents column element in first row of Mueller matrix, and $j = 1 : 4$ is pixel number.

Fig. 5.12 shows total error in each Mueller parameter as a function of spacer thickness, as well total error by summing up errors in all Mueller parameters (green curve). The values represent absolute error, according to Eq. (5.12). From this plot, a pattern in total error can be observed with minimum values around 300 and 600 nm. For an analysis in next sections, the spacer thickness of 300 nm is chosen. In Table 5.2 is an overview of the simulated and ideal Mueller matrices for all four pixels.

Table 5.2: Overview of the Mueller matrices for all four pixels: the simulated model with a spacer thickness of 300 nm, and ideal model.

	\mathbf{M}_{sim}	\mathbf{M}_{ideal}
Pixel A	$\begin{bmatrix} 0.4987 & 0.3082 & -0.1634 & -0.3561 \\ 0.4950 & 0.3051 & -0.1636 & -0.3541 \\ 0.0526 & 0.0436 & -0.0116 & -0.0306 \\ -0.0261 & -0.0144 & -0.0037 & 0.0259 \end{bmatrix}$	$\begin{bmatrix} 0.5000 & 0.3085 & -0.1106 & -0.3777 \\ 0.5000 & 0.3085 & -0.1106 & -0.3777 \\ 0 & 0 & 0 & 0 \\ 0 & 0 & 0 & 0 \end{bmatrix}$
Pixel B	$\begin{bmatrix} 0.4964 & -0.2265 & -0.4282 & 0.1072 \\ -0.2496 & 0.1161 & 0.2173 & -0.0423 \\ -0.4288 & 0.1947 & 0.3692 & -0.0995 \\ -0.0001 & -0.0120 & 0.0068 & 0.0011 \end{bmatrix}$	$\begin{bmatrix} 0.5000 & -0.2385 & -0.4264 & 0.1066 \\ -0.2500 & 0.1192 & 0.2132 & -0.0533 \\ -0.4330 & 0.2065 & 0.3692 & -0.0923 \\ 0 & 0 & 0 & 0 \end{bmatrix}$
Pixel C	$\begin{bmatrix} 0.4978 & 0.3063 & 0.1607 & 0.3577 \\ 0.4945 & 0.3056 & 0.1587 & 0.3552 \\ 0.0507 & 0.0201 & 0.0218 & 0.0435 \\ -0.0222 & -0.0154 & -0.0195 & -0.0090 \end{bmatrix}$	$\begin{bmatrix} 0.5000 & 0.3085 & 0.1106 & 0.3777 \\ 0.5000 & 0.3085 & 0.1106 & 0.3777 \\ 0 & 0 & 0 & 0 \\ 0 & 0 & 0 & 0 \end{bmatrix}$
Pixel D	$\begin{bmatrix} 0.4981 & -0.2263 & 0.4303 & -0.1069 \\ -0.3063 & 0.1407 & -0.2671 & 0.0540 \\ 0.3917 & -0.1763 & 0.3375 & -0.0933 \\ -0.0239 & 0.0243 & -0.0134 & 0.0059 \end{bmatrix}$	$\begin{bmatrix} 0.5000 & -0.2385 & 0.4264 & -0.1066 \\ -0.2500 & 0.1192 & -0.2132 & 0.0533 \\ 0.4330 & -0.2065 & 0.3692 & -0.0923 \\ 0 & 0 & 0 & 0 \end{bmatrix}$

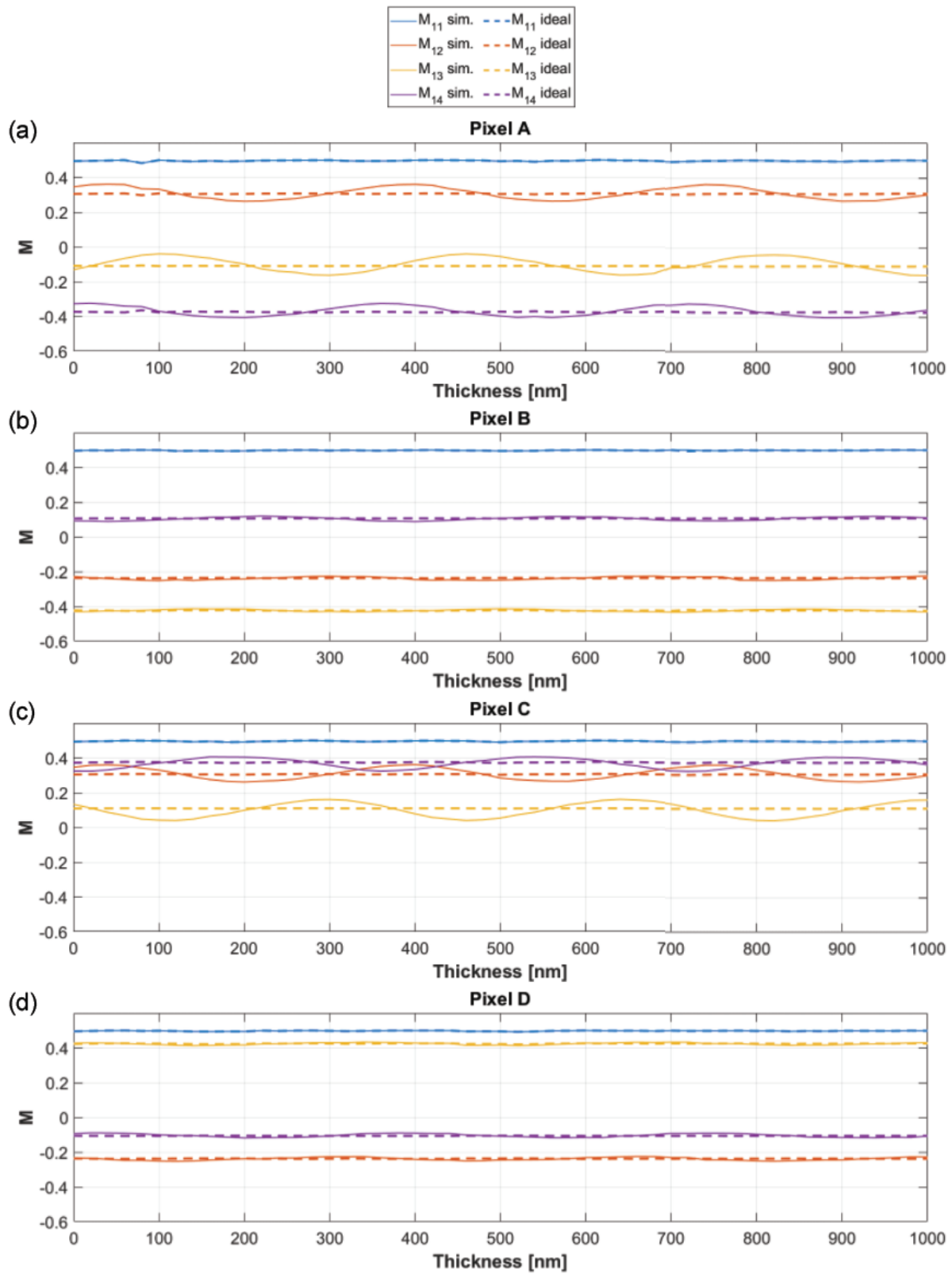


Figure 5.11: Mueller parameters (the first row of the Mueller matrix) vs spacer thickness diagram for all four pixels.

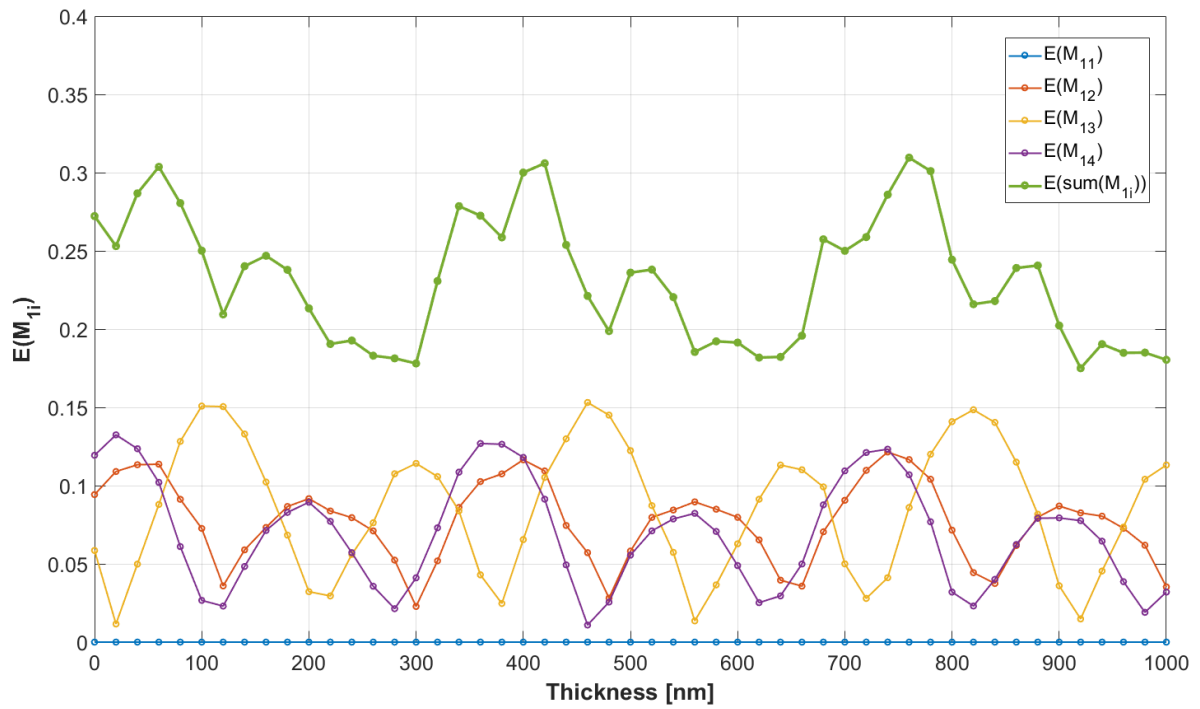


Figure 5.12: The total error in Mueller parameters (sum for all four pixels) vs spacer thickness diagram. Also, the overall error as the sum of all parameters (green curve).

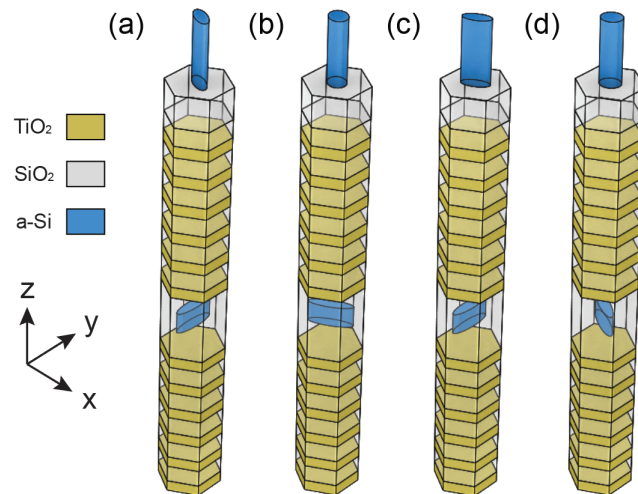


Figure 5.13: Four unit cells of the simulated two layered metasurfaces, with spacer thickness of 300 nm. Pixels from A to D correspond to (a) to (d), respectively.

5.6. FINAL CONCEPT OVERVIEW

This section serves as an overview of the complete concept. The complete spectropolarimeter is consisted of following components, starting from detector array:

- detector array with integrated two-layered metasurface used to encode polarization and spectrum
- telecentric lens

- narrow bandpass spectral filter, defining finite spectral bandwidth

The detector array with integrated layers for encoding the polarization and spectrum is consisted of following layers:

- detector array
- Fabry-Pérot filter array with embedded dielectric elliptic cylinders or sub-wavelength grating inside the cavity. That allows filtering certain wavelengths of different polarization orientations. Therefore, this layer serves as a linear polarizer and as a spectral filter in the same layer. Because this configuration of Fabry-Pérot will give two orthogonal polarizations at different wavelengths, it is necessary to filter out one transmittance peak by placing correct narrow bandpass spectral filter.
- waveplate array consisted of an array elliptic cylinders where retardance is defined by ellipse diameters and fast axis is defined by orientation angle of the elliptic cylinders.

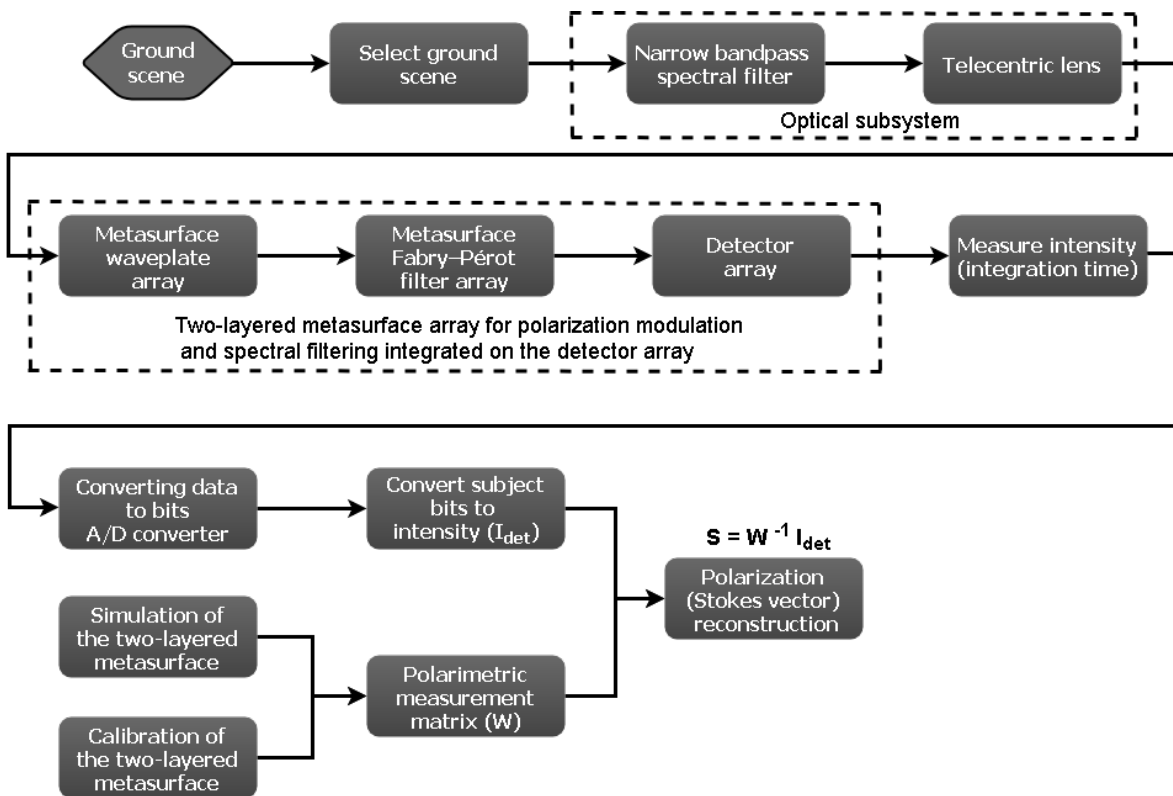


Figure 5.14: Functional Flow block diagram for the metasurface-based spectropolarimeter design.

Fig. 5.14 shows a functional flow block diagram for the metasurface-based spectropolarimeter design. Since each spectral band is reconstructed separately, this diagram represents polarization reconstruction for single spectral band. Also, blocks: *Simulation of the two-layered metasurfaces* and *Calibration of the two-layered metasurfaces* are done before implementing the spectropolarimeter. In Fig. 5.15 (a) is shown a graphical illustration of the design of the superpixel (four pixels), consisting of the two-layered metasurfaces integrated on the detector array. The front view is shown in Fig. 5.15 (b). Note that this design is not in scale. The purpose of the scheme is to show the concept. The full-scale scheme would have too many unit cells over a single detector pixel, and the scheme would not be clear.

5.6.1. DETECTOR LAYOUT

In the previous section, the scheme of the complete superpixel is shown. In this subsection, the detector layout is described.

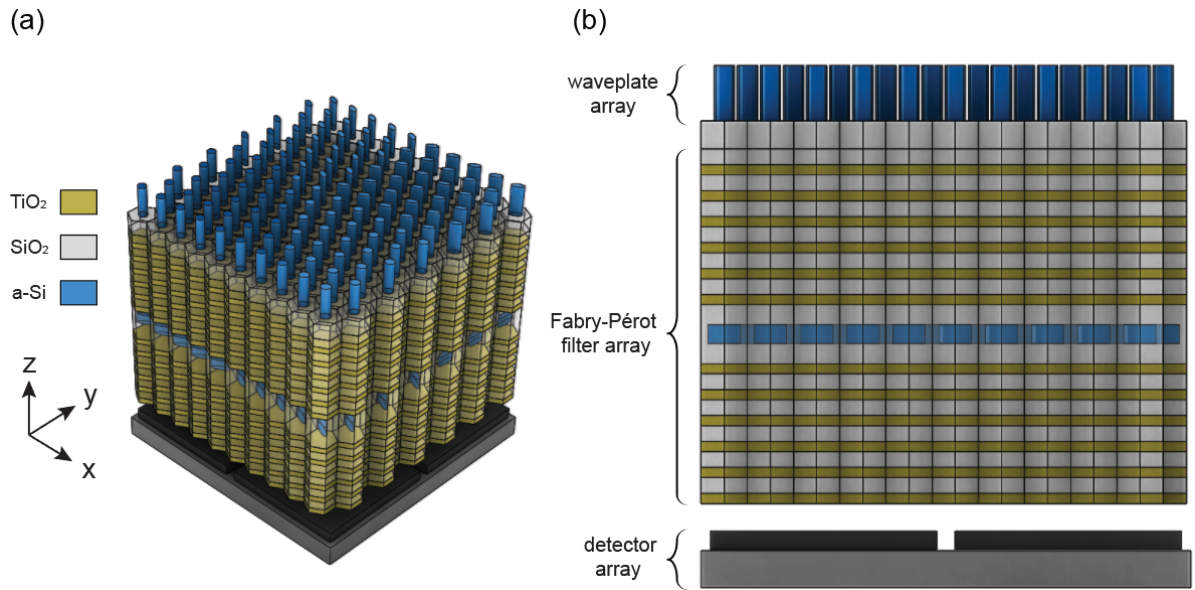


Figure 5.15: (a) Graphical illustration of the design of the superpixel (four pixels), consisting of the two-layered metasurface integrated on the detector array. (b) Front view of the superpixel. Note that scheme is not in scale.

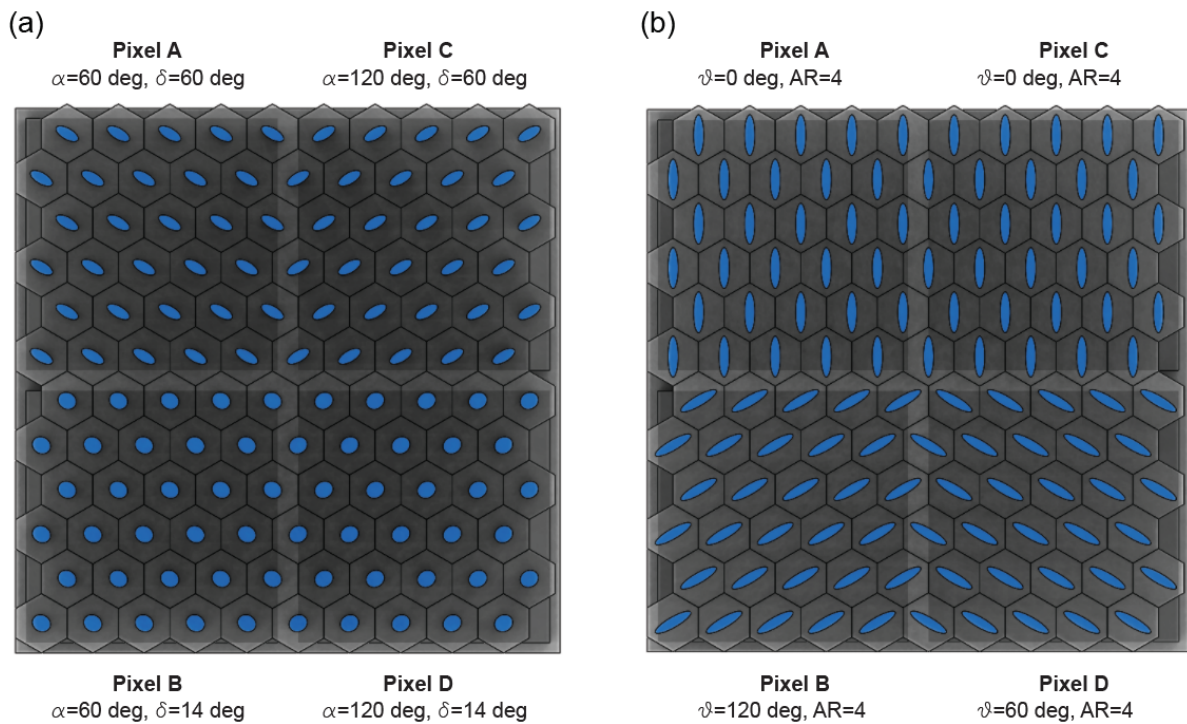


Figure 5.16: (a) Top view of the metasurface as the waveplate with different arrays of elliptic cylinders over the four pixels. (b) Cut-section of the metasurface embedded in the FP filter, with different arrays of elliptic cylinders over the four pixels. Note that scheme is not in scale.

Fig. 5.16 (a) shows the top view of the superpixel, with labeled individual pixels, and Fig. 5.16 (b) shows a

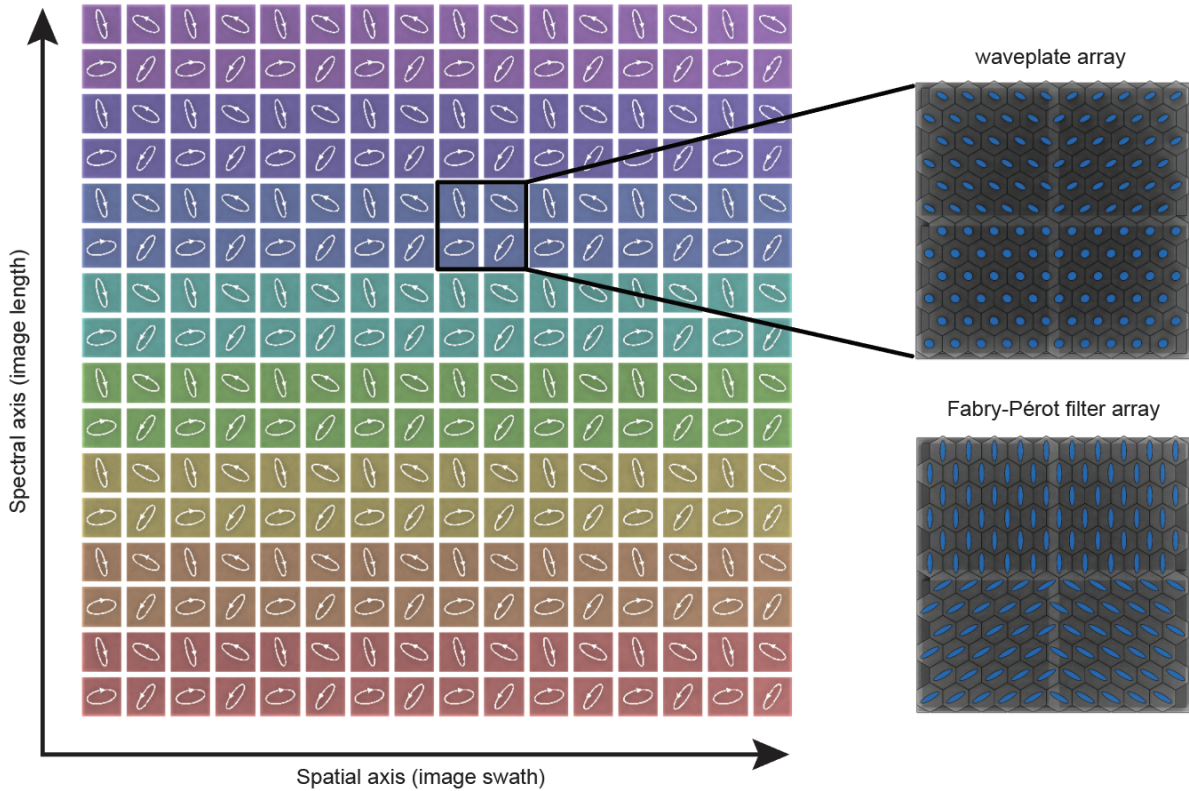


Figure 5.17: Overview of the detector layout. The superpixels consisted of 4 differently modulated surfaces integrated on the detector array. The horizontal axis corresponds to spatial (image swath), and the vertical axis corresponds to the spectral axis (image length).

cut section of embedded metasurface array inside the cavity of four FP filters. The layout of the complete detector array is illustrated in Fig. 5.17, where the horizontal axis corresponds to spatial (image swath), and the vertical axis corresponds to the spectral axis (image length). Also, the superpixel (2x2 pixels) is denoted, and its relation to the metasurface array layout. Each pixel of the superpixel has different polarization modulation, which is denoted as four different ellipses with different handedness. The superpixels are repeated in the horizontal axis, while in the vertical axis of the detector, the polarization modulation is still the same, but the filtered center wavelength are different.

5.7. POLARIZATION ACCURACY CALCULATION

In this section is estimated how the real design based on the metasurfaces, together with other sources of uncertainty, like shot noise, impacts the final polarization uncertainty.

Systematic effects and noise limit the performance of a polarimeter. The smallest polarization signal that a polarimeter can detect is defined as the polarimetric sensitivity. It is related to the final noise levels in Q/I , U/I , and V/I . Along with shot and read-out noise, other random effects like spurious polarization signals limit the detectability of a certain signal. In general, the polarimetric sensitivity is determined by errors that are not "real" polarization effects. [48]

Poisson photon counting statistics play a critical role in polarimetry. To measure a polarization degree of 10^{-n} , it is necessary to collect at least 10^{2n} photons (for shot noise limited system). For example, to measure the degree of polarization, $p \approx 10^{-3}$, it is necessary to accumulate 10^6 photons. A typical CCD has a well-depth (saturation) $\approx 10^5$ electrons per pixel. That would require approximately 10 pixel readouts to collect enough photons. [49]

Shot noise limited polarimetric sensitivity can be derived as follows. Starting from Eq. 5.13, and equalizing it with expression 10^{-n} , which represents a generic value of the polarimetric sensitivity, it becomes:

$$\sigma_X = \frac{1}{\sqrt{I}} \quad (5.13)$$

where σ_X is expected error.

$$10^{-n} = \frac{1}{\sqrt{I}} \quad (5.14)$$

After some manipulation, the expression is equal to:

$$I = 10^{2n} \quad (5.15)$$

where I is measured intensity (photons). This expression shows that in order to achieve polarimetric sensitivity of 10^{-n} , there is need to measure at least 10^{2n} photons (n is the relation parameter between polarimetric sensitivity and required photons to achieve it).

5.7.1. SIGNAL-TO-NOISE RATIO CALCULATION

Signal-to-noise ratio (SNR) is a measure used to compare the level of a signal to the level of background noise. It is an important figure of merit for a detection system. In order to estimate the signal that is impinging on the detector pixel, the radiance of an observed scene should be known. Fig. 5.18 is an example of spectral radiance, $L_{\Omega,\lambda}$ of some scene on the Earth ground surface, where L_{min} indicates minimum, and L_{max} maximum expected radiance. The radiance used to estimate the signal is the midpoint of minimum and maximum

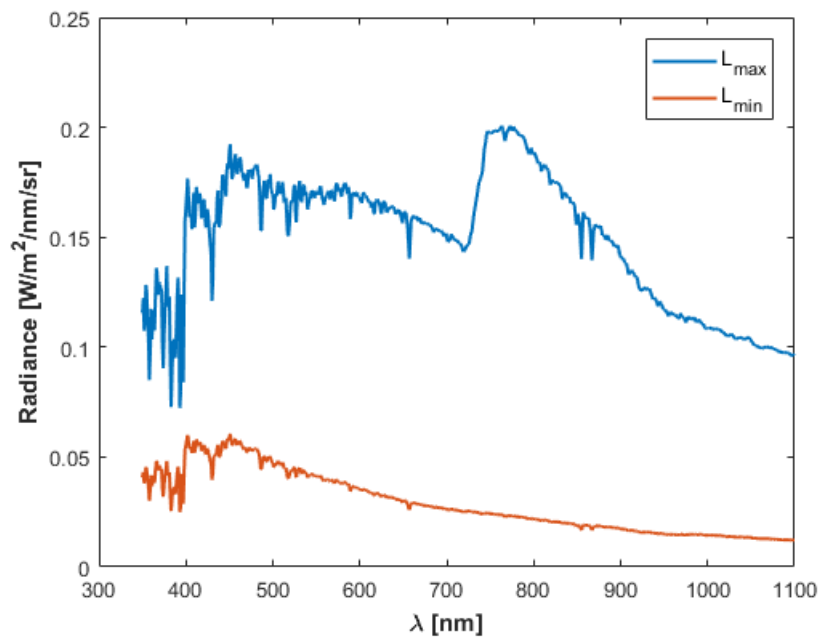


Figure 5.18: Minimum and maximum expected radiance vs wavelength. [14]

expected radiance at a reference wavelength of 600 nm (the midpoint of the spectral requirement, Table 2.1). The approximate value of this radiance is: $L_{\Omega,\lambda=600nm} = 0.1$ [W/m²/nm/sr].

Furthermore, an additional required parameter to estimate the signal is quantum efficiency of the detector. The quantum efficiency is defined as an average number of electrons created per photon. In Fig. 5.19 is shown quantum efficiency as a function of wavelength for a monochrome CMV4000 image sensor. [15] The used quantum efficiency in this calculation is $QE = 0.6$ (at the reference wavelength).

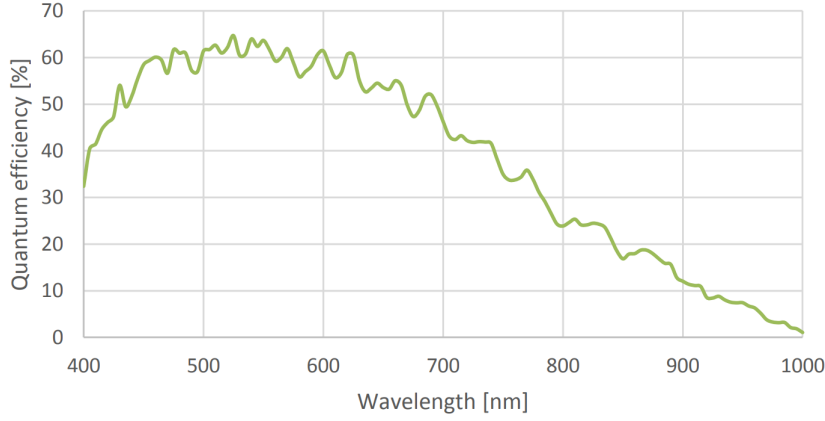


Figure 5.19: Quantum efficiency vs wavelength diagram. Spectral response of a monochrome CMV4000 with the microlenses image sensor. [15]

$$S = \left(L_{\Omega,\lambda} \frac{\lambda}{h c} \right) \Delta\lambda \text{IFOV} A_{ap} QE \eta_T t_{int} = 2.15 \times 10^4 \text{ [e}^-/\text{pixel]} \quad (5.16)$$

The parameters in the equation are explained in Table 5.3.

Total noise is calculated by using the root mean square (RMS), where considered sources of noise are: the shot noise, the dark current noise, and the read noise. The parameters are described in Table 5.4.

$$N_{total} = \sqrt{S + n_{dark}^2 + n_R^2} = 151.6 \text{ [e}^-/\text{pixel]} \quad (5.17)$$

where

$$n_{dark} = n_{dark,t} t_{int} \quad (5.18)$$

The SNR for the reference wavelength of 600 nm is then calculated as:

$$SNR = \frac{S}{N_{total}} = 142 \quad (5.19)$$

In Fig. 5.20 is shown SNR as function of wavelength. The assumption in this plot are: constant quantum efficiency QE , constant throughput η_T over the wavelengths. The radiance used is the average of minimum (L_{min}) and maximum (L_{max}) expected radiance.

Table 5.3: Overview of the parameters used in the signal calculation, Eq. (5.16).

Parameter	Value	Description
$L_{\Omega,\lambda}$	0.1 [W/m ² /nm/sr]	spectral radiance, @ 600 nm wavelength (Subsection 5.7.1)
λ	600×10^{-9} [m]	wavelength (Subsection 5.7.1)
h	6.626×10^{-34} [m ² kg/s]	Planck constant
c	299792458 [m/s]	the speed of light
$\Delta\lambda$	1.1 [nm/pixel]	spectral resolution, <i>FWHM</i> (Subsection 5.2.1)
<i>IFOV</i>	5.4788×10^{-9} [sr]	instantaneous field of view (Subsection 5.1)
A_{ap}	7.854×10^{-5} [m ²]	aperture area (Subsection 5.1.1)
QE	0.6 [e ⁻ /ph]	quantum efficiency (Subsection 5.7.1)
η_T	0.85 [-]	throughput, transmittance efficiency @ 589.1 nm wavelength (Fig. 5.5 (d), Subsection 5.3)
t_{int}	0.2942 [s]	integration time (Subsection 5.1)

Table 5.4: Overview of the parameters used in the noise calculation, Eq. (5.17).

Parameter	Value	Description
$n_{s,shot}$	\sqrt{S} [e ⁻]	signal shot noise, due to Poisson statistics
n_R	13 [e ⁻] RMS	read noise (dark noise) [15]
$n_{dark,t}$	125 [e ⁻ /s]	dark current, @ 25°C die temperature [15]

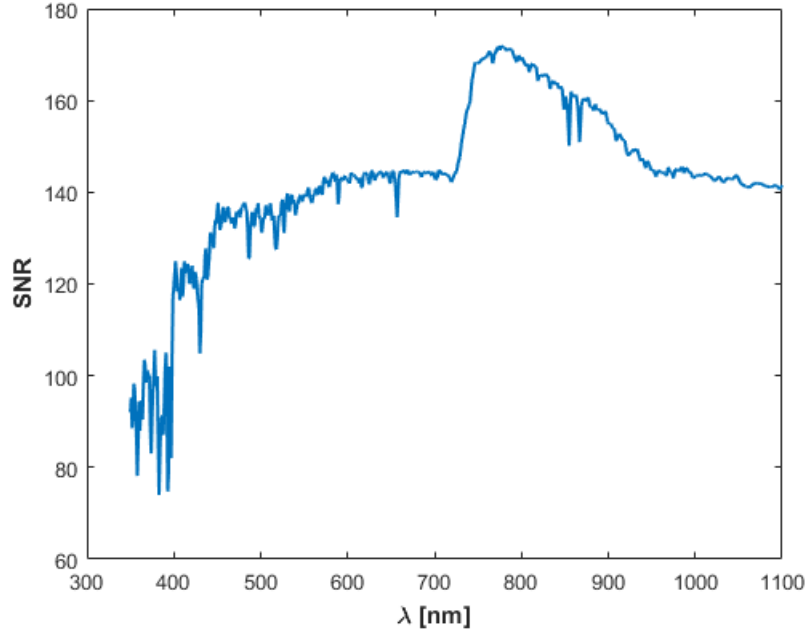


Figure 5.20: SNR vs wavelength diagram.

5.7.2. POLARIZATION UNCERTAINTY

In this subsection, the polarization uncertainty is estimated. In the previous subsection, the SNR is calculated for single detector pixel. However, the ground scene of a single detector pixel has ground sample distance $GSD = 0.05$ m, which is much less than required resolution for the polarization, $S_r = 2$ km (Section 5.1). In order to cover this resolution (S_r) about 40 pixels along the swath axis should be stacked, which then correspond to 20 superpixels. This is illustrated in the scheme in Fig. 5.21 (a). Another considered case is adding additional 5 superpixels along the scan axis, resulting in total of 100 superpixels (5.21 (b)). This allows oversampling in time (for instance in a time-delayed-integration (TDI) mode), which increases the total number of measured photons. In other words, the measurement of a ground scene is distributed over multiple detector pixels, where the average value is estimated by the least squares method.

The outgoing Stokes parameters at each pixel is calculated as:

$$\mathbf{S}_{out} = \mathbf{M}_{sim,j} \mathbf{S}_{in} \quad (5.20)$$

where $\mathbf{M}_{sim,j}$ are the Mueller matrices for pixels from A to B (with $j = 1 : 4$) in Table 5.2.

The equations from Eq. (4.17) to Eq. (4.21) from subsection 4.2.2 are now modified for this specific case:

$$I_{noise,i} = N_{randn} \sqrt{S_{out,0,i} + n_{dark}^2 + n_{RO}^2} \quad (5.21)$$

where $I_{noise,i}$ is estimated intensity measured on the detector of i th pixel, N_{randn} is normally distributed random number, and $S_{out,0,i}$ (Eq. (5.20)) is the outgoing intensity passing through ideal system composed of

corresponding waveplate and linear polarizer, defined by Mueller matrix in Eq. (4.2).

The estimated intensity on the detector, $I_{det,i}$ of i th pixel is calculated as:

$$I_{det,i} = S_{out,0,i} + I_{noise} = S_{out,0,i} + N_{randn} \sqrt{S_{out,0,i} + n_{dark}^2 + n_{RO}^2} \quad (5.22)$$

Using Eq. (4.13) the Stokes vector, \mathbf{S}_{est} is estimated, where \mathbf{I}_{det} is $n \times 1$ vector containing simulated intensities at all pixels:

$$\mathbf{S}_{est} = \tilde{\mathbf{W}}_{id}^{-1} \mathbf{I}_{det} \quad (5.23)$$

where $\tilde{\mathbf{W}}_{id}^{-1}$ is formed from ideal Mueller matrices from Table 5.2.

Then the relative error of normalized Stokes parameters is defined as:

$$ES_k = \frac{S_{in,k} - S_{est,k}}{S_{in,0}} \quad (5.24)$$

where ES_k is error in k th Stokes parameter. In the end, by taking the standard deviation of the certain number of simulation gives the estimation of uncertainty in reconstructed Stokes parameters. The number of simulations (each generating different random numbers for noise estimation) used is equal to 200. The result is a vector with the shape of $n \times 1$, \mathbf{ES}_k representing the result of errors in Stokes parameters for 200 simulations.

$$\sigma(\mathbf{ES}_k) = std(\mathbf{ES}_k) \quad (5.25)$$

In Fig. 5.22, the final results of uncertainty in stokes parameters as a function of different incident polarization states. Four plots represent uncertainty in all four Stokes parameters. Also, three different configurations are considered: 1, 20, and 100 superpixels. From this results, the polarization accuracy (sensitivity) could be estimated around 2×10^{-3} for 20 superpixels, and 10^{-3} for 100 superpixels. The assumption in this calculation is constant incident polarization over the scene. Also, the impact due to the optical subsystem on the polarization accuracy is not taken in this research.

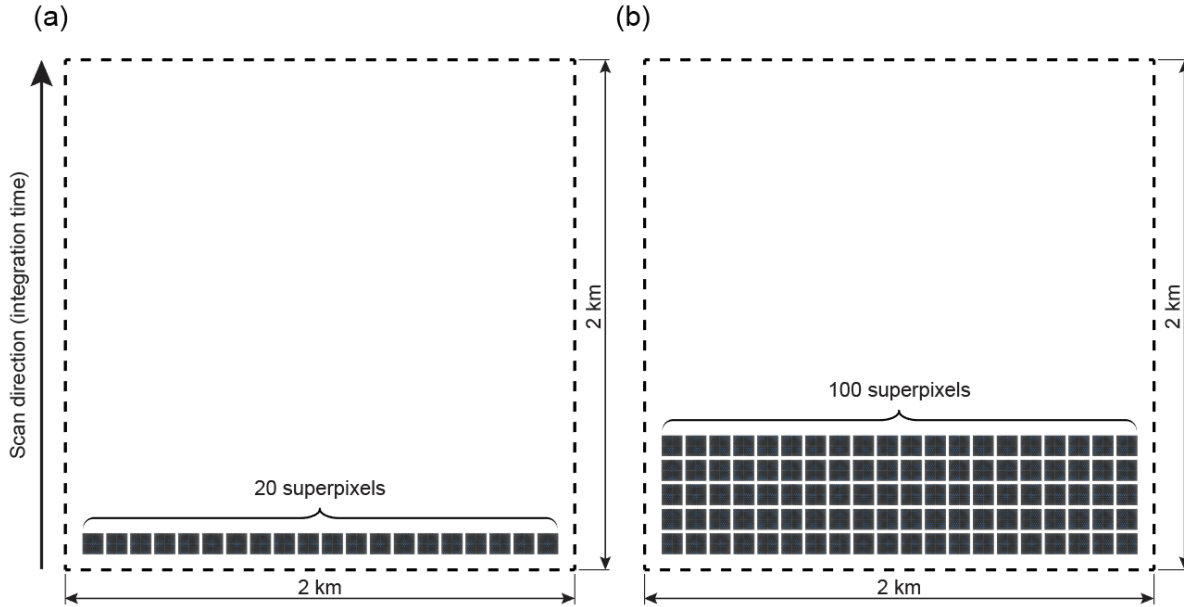


Figure 5.21: (a) A configuration of superpixels arranged in one line along the swath axis, resulting in 20 superpixels. (b) A configuration of superpixels arranged in five lines along the swath axis, resulting in 100 superpixels.

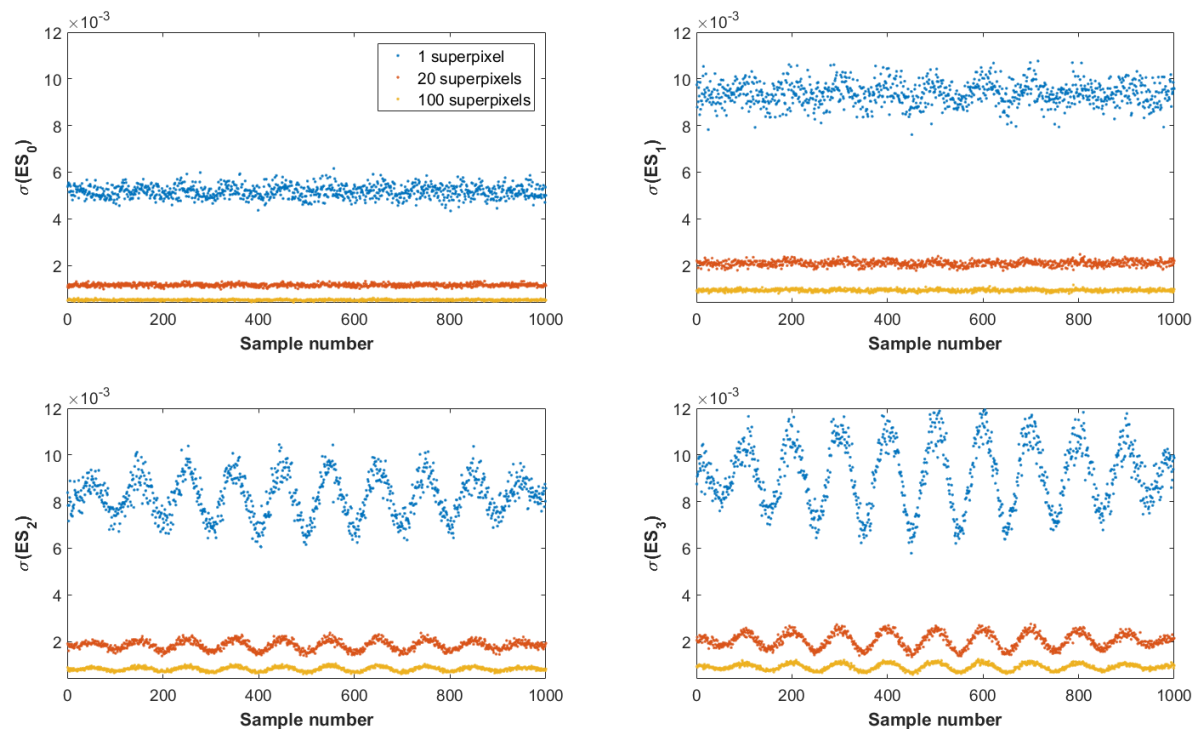


Figure 5.22: The standard deviation of error in estimated Stokes vs different incident polarization states (sample number) diagram. Blue points represent 1 superpixel, red points 20 superpixels, and 100 superpixels.

5.8. OVERVIEW OF THE RESULTS

This section serves as an overview of the results obtained in this research. In Table 5.5 is a requirements comparison between SPEXone instrument, and the instrument proposed in this research: metasurface-based design. The starting point in this research is the same swath width and spatial sampling as in the reference mission. Also, only one viewing angle is considered due to simplifications. The result showed similar achievable spectral range. However, the maximum spectral bandwidth is smaller (≈ 30 nm @ $\lambda = 400$ nm, and ≈ 100 nm @ $\lambda = 1600$ nm) than in the reference instrument, which is the only disadvantage of this concept. However, this spectral bandwidth corresponds to the design with constant cavity height over the detector array. If the multiple cavity heights are implemented, for instance with several steps (heights) along the detector array, the total spectral bandwidth can be increased several times. Furthermore, a large improvement in spectral resolution for polarization is possible. This spectral resolution can be tuned by selecting a different number of the DBR layers in the FP filter. For 6 pairs of DBR layers, the spectral resolution is about 1.1 nm, which is at least 20 times better than in the reference instrument. Also, the possibility to measure circular polarization is another advantage. The polarimetric accuracy is comparable to the reference instrument. Note that this estimation is limited, and further improvement of the budget is necessary. The value of DoCP is about 10^{-3} , which is still one order of magnitude lower than required (10^{-4}). This could be improved by increasing the aperture diameter (in this design is used 1 cm) in order to decrease the uncertainty due to shot noise. In the end, the volume of the metasurface-based spectropolarimeter concept can be reduced significantly. The total estimated volume of payload corresponds to about 1.5-unit-Cube (which is based on the focal length). It is important to note that most of the volume is taken due to the optical subsystem (telescope), while the spectropolarimeter is basically a layer of few micrometers integrated on the detector array.

Table 5.5: Comparison of the requirements of the SPEXone and Metasurface-based design. The color of the text denotes advantage (green color) and disadvantage (red color) over reference instrument SPEXone.

Parameter	SPEXone	Metasurface-based design
Swath width	9° (100 km) [25]	100 km (Section 5.1)
Viewing angles	5 (-57°, -20°, 0°, 20°, 57°) [25][29]	1 (Section 5.1)
Achievable spectral range	385-1600 nm [26][29]	400-1600 nm (Section 5.3)
Maximum spectral bandwidth	385-770 nm [26][29]	ranges from 30 to 100 nm (Section 5.3)
Spectral resolution on intensity	4 nm [29]	1.1 nm (Subsection 5.2.1)
Spectral resolution for polarization	20-40 nm [29]	1.1 nm (Subsection 5.2.1)
Spatial sampling	2.3×2.7 km ² [29]	2x2 km² (Section 5.1)
Stokes parameters measured	S ₀ , S ₁ , S ₂ [2] [29]	S₀, S₁, S₂, S₃ (Subsection 5.7.2)
Polarimetric accuracy, DoLP	0.003 [29]	0.001 (Subsection 5.7.2)
Polarimetric accuracy, DoCP	-	0.001 (Subsection 5.7.2)
Volume	6-unit-CubeSat payload [2]	1.5-unit-CubeSat payload (Subsection 5.1.1)

6

CONCLUSION AND RECOMMENDATIONS

6.1. CONCLUSION

The systematic electromagnetic analysis of metasurface-based spectropolarimeter showed its pros and cons with respect to reference instrument. The spectropolarimetric technique, the division of focal plane (DoFP) is selected, as an extremely compact concept for full-Stokes polarimetry integrated on the detector array. The full-Stokes vector can be retrieved by a set of four pixels, consisted of two layers: a waveplate and a linear polarizer. It is shown that metasurface can provide different retardance with a constant thickness of the layer, which has an advantage over conventional waveplates, where the retardance is controlled by the different thickness of crystals. That simplifies the integration since the waveplate array has a constant thickness over the detector array. Moreover, it is shown that embedding a birefringent metasurface inside the Fabry-Perot cavity forms a structure that has two functions: as a linear polarizer and as a spectral filter in a single layer. Two different configurations of metasurface are considered: an array of amorphous silicon ($a-Si$) elliptic cylinders with high transmittance ($\approx 90\%$) in wavelength range from 900 to 1600 nm, and sub-wavelength grating made of titanium dioxide (TiO_2) with high transmittance ($\approx 85\%$) in wavelength range from 400 to 800 nm. Furthermore, by implementing distributed Bragg reflector (DBR), high spectral resolutions are achievable. A spectral resolution of 1.1 nm is estimated, which is at least 20 times better than in the reference instrument. Also, the sensitivity analysis is conducted to show the impact of fabrication tolerance on the performance. The result showed that in the case of metasurface operating as a waveplate, the maximum deviation in the retardance is about 12 deg due to fabrication tolerance. Nevertheless, this deviation has a negligible impact on the polarization reconstruction (only a slight increase in the condition number). Furthermore, the deviation in center wavelength in the spectrum of ± 4 nm is present due to fabrication tolerance. That requires calibration in the spectral response of individual pixels.

The analysis of two-layered metasurface showed that the thickness of the spacer separating two layers has the impact of the total response (Mueller matrix of both layers), where a periodic deviation from the ideal response is observed. However, the total error in Mueller parameters is small, which confirms that two-layered metasurface could be used as an alternative to conventional waveplates and linear polarizers. In the end, the polarization uncertainty of final selected design is estimated. In this calculation, the signal on each pixel detector is simulated by taking into account sources of noise. The spatial and temporal oversampling of the same scene allows a larger number of photons to be detected and therefore better polarization accuracy. For instance, by implementing 100 superpixels to estimate polarization over the single ground scene of 2x2 km, the achievable uncertainty in Stokes parameters is about 10^{-3} , which is slightly better than in the reference instrument. Note that the impact of the optical subsystem on polarization state is not considered in this research since the optical subsystem was not the subject of the research. Furthermore, due to the compact design, the volume of the instrument could significantly be reduced. Taking only the estimated focal length of 15 cm, the total volume of the instrument would correspond to 1.5-unit-CubeSat payload, which is 4 times less than the reference instrument. Besides the reduction in the volume, the significance of this spectropolarimeter design is the reduction in a number of components required to modulate polarization state. In terms of requirements with respect to the reference instrument, the only disadvantage of the metasurface-based spectropolarimeter design is a small achievable spectral range, which ranges about 30 nm at the wave-

length of 400 nm, to 100 nm at the wavelength of 1600 nm. The reason for that was the initial assumption in the design of constant thickness of the metasurface over the detector array. In order to increase the spectral range, multiple thicknesses over the detector array should be implemented. Also, in this design, only one viewing angle is considered due to the simplifications. The extension to multiple viewing angles only requires modifications in the optical subsystem and projection on the detector array.

6.2. RECOMMENDATIONS

The metasurface-based spectropolarimeter design presented in this research still has space for optimization, which would require extensive computations time. The result showed that there are multiple solutions to design the required spectropolarimetric modulation. That allows finding the best dimensions of the nanostructures, where the parameter of interest is uniform inside the range of fabrication tolerance. That would result in an instrument that is less sensitive to fabrication errors. Moreover, further optimization in the performance of two-layered metasurface should be conducted, due to the presence of an error in the Mueller matrix as a function of spacer thickness.

The impact of the optical subsystem on polarization accuracy is not considered in this research. Since the lens could alter the polarization state of incoming light, this effect should also be taken into the budget of polarization uncertainty. The estimated volume of the instrument in this research is only an assumption, while the final volume could be obtained when the optical subsystem is known.

Thermal and mechanical stability under a wide range of external conditions, like temperature change of such structures, is still unexplored field and requires further study.

During the polarization uncertainty calculation, it is assumed that state of polarization is constant over the whole ground scene. This might not be the case in reality. The best arrangement of spatial sampling should be studied in order to minimize the polarization aliasing.

Since it is impossible to estimate the final performance of the system within the limited timeframe, the recommendations for further study are summarized:

- Further optimization of the metasurfaces and spectropolarimetric technique
- Design of optical subsystem (impact on the polarization accuracy)
- Thermal and mechanical stability analysis of metasurfaces
- Design of an algorithm for polarization reconstruction of multiple superpixels

BIBLIOGRAPHY

- [1] Wikipedia, *Stokes parameters*, https://en.wikipedia.org/wiki/Stokes_parameters (2018).
- [2] SRON, *Spex*, <https://www.sron.nl/earth-instrument-development/spex/spexone/> (2018).
- [3] H. Macleod, *Thin-Film Optical Filters, Fifth Edition*, Series in Optics and Optoelectronics (CRC Press, 2017).
- [4] A. Arbabi, R. M. Briggs, Y. Horie, M. Bagheri, and A. Faraon, *Efficient dielectric metasurface collimating lenses for mid-infrared quantum cascade lasers*, *Opt. Express* **23**, 33310 (2015).
- [5] H. Yu, *Controlling the flow of light using high-contrast metastructures. dissertation (ph.d.)*, California Institute of Technology, doi:10.7907/Z94X5604, <http://resolver.caltech.edu/CaltechTHESIS:09202017-124555409> (2018).
- [6] A. I. Kuznetsov, A. E. Miroshnichenko, M. L. Brongersma, Y. S. Kivshar, and B. Luk'yanchuk, *Optically resonant dielectric nanostructures*, *Science* **VOL 354 ISSUE 6314** (18 NOVEMBER 2016).
- [7] J. van de Groep and A. Polman, *Designing dielectric resonators on substrates: Combining magnetic and electric resonances*, *Opt. Express* **21**, 26285 (2013).
- [8] F. Snik, J. Craven-Jones, M. Escuti, S. Fineschi, D. Harrington, A. D. Martino, D. Mawet, J. Riedi, and J. S. Tyo, *An overview of polarimetric sensing techniques and technology with applications to different research fields*, (2014).
- [9] H. Hsiao, C. H. Chu, and D. P. Tsai, *Fundamentals and applications of metasurfaces*, WILEY-VCH Verlag GmbH & Co. KGaA, Weinheim **1**, 1600064 (2017).
- [10] E. F. Schubert, *Light-Emitting Diodes*, 2nd ed. (Cambridge University Press, 2006).
- [11] Y. Horie, A. Arbabi, E. Arbabi, S. M. Kamali, and A. Faraon, *Wide bandwidth and high resolution planar filter array based on dbr-metasurface-dbr structures*, | Vol. 24, No. 11 | DOI:10.1364/OE.24.011677 | OPTICS EXPRESS 11677 (2016).
- [12] L. Zheng and M. Tidrow, *Analyses of infrared focal plane array figure of merit and its impact on sensor system trades*, *Infrared Physics Technology* **52**, 408 (2009), proceedings of the International Conference on Quantum Structure Infrared Photodetectors (QSIP) 2009.
- [13] Edmundoptics, *Telecentric design topics*, <https://www.edmundoptics.com/resources/application-notes/imaging/telecentric-design-topics/> (2018).
- [14] ESTEC, *Co2 mission applicable reference spectra and scenes, annex 1 to srd co2-rs-es-sy-0002*, <https://earth.esa.int/> (2018).
- [15] AMS, *Cmv4000 v3 datasheet: 4.2 megapixel machine vision cmos image sensor*, https://ams.com/documents/20143/36005/CMV4000_DS000436_1-00.pdf/f03c3681-6a4c-e63b-b61a-7faa07088580 (2015).
- [16] M. Bass, C. DeCusatis, J. Enoch, V. Lakshminarayanan, G. Li, C. Macdonald, V. Mahajan, and E. Van Stryland, *Handbook of Optics, Third Edition Volume II: Design, Fabrication and Testing, Sources and Detectors, Radiometry and Photometry*, 3rd ed. (McGraw-Hill, Inc., New York, NY, USA, 2010).
- [17] R. M. A. Azzam and N. M. Bashara, *Ellipsometry and polarized light*, North-Holland personal library (North-Holland Pub. Co., 1977).
- [18] O. P. Hasekamp and J. Landgraf, *Retrieval of aerosol properties over land surfaces: capabilities of multiple-viewing-angle intensity and polarization measurements*, *APPLIED OPTICS* Vol. 46, No. 16 (2007).

- [19] O. Hasekamp, *Capability of multi-viewing-angle photo-polarimetric measurements for the simultaneous retrieval of aerosol and cloud properties*, Atmospheric Measurement Techniques, vol. 3, no. 4, p. 839 (2010).
- [20] Stam, D. M., *Spectropolarimetric signatures of earth-like extrasolar planets**, *A&A* **482**, 989 (2008).
- [21] M. Devogèle, A. Cellino, S. Bagnulo, J. P. Rivet, P. Bendjoya, L. Abe, C. Pernechele, G. Massone, D. Vernet, P. Tanga, and C. Dimur, *The calern asteroid polarimetric survey using the torino polarimeter: assessment of instrument performances and first scientific results*, *Monthly Notices of the Royal Astronomical Society* **465**, 4335 (2017).
- [22] L. Kolokolova, J. Hough, and A. Levasseur-Regourd, *Polarimetry of Stars and Planetary Systems* (Cambridge University Press, 2015).
- [23] SCARBO, *Concept, scope and challenges*, <http://scarbo-h2020.eu/> (2018).
- [24] C. L. Holloway, E. F. Kuester, J. A. Gordon, J. O'Hara, J. Booth, and D. R. Smith, *An overview of the theory and applications of metasurfaces: The two-dimensional equivalents of metamaterials*, *IEEE Antennas and Propagation Magazine* **54**, 10 (2012).
- [25] NASA, *Pace oceansciences*, <https://pace.oceansciences.org/mission.htm> (2018).
- [26] A. van Amerongen, J. Rietjens, M. Smit, D. van Loon, H. van Brug, W. van der Meulen, M. Esposito, and O. Hasekamp, *Spex the dutch roadmap towards aerosol measurement from space*, (2017).
- [27] J. H. H. Rietjens, M. Smit, G. van Harten, A. D. Noia, O. P. Hasekamp, J. de Boer, H. Volten, F. Snik, and C. U. Keller, *Accurate spectrally modulating polarimeters for atmospheric aerosol characterization*, (2015).
- [28] Bagnulo, S., Boehnhardt, H., Muinonen, K., Kolokolova, L., Belskaya, I., and Barucci, M. A., *Exploring the surface properties of transneptunian objects and centaurs with polarimetric forsl/vlt observations*, *A&A* **450**, 1239 (2006).
- [29] A. Amerongen, J. Rietjens, J. Campo, E. Dogan, J. Dingjan, R. Nalla, J. Caron, and O. Hasekamp, *Spexone: A compact multi-angle polarimeter*, (2018).
- [30] F. T. Ulaby and U. Ravaioli, *Fundamentals of Applied Electromagnetics* (Pearson, 2015).
- [31] ANSYS, *HFSS Online Help, Release 17.2* (July 2016).
- [32] M. A. Richards, J. A. Scheer, and W. A. Holm, *Principles of Modern Radar: Basic Principles*, edited by M. A. Richards, J. A. Scheer, and W. A. Holm (SciTech Publishin, 2010).
- [33] M. Losurdo and K. Hingerl, *Ellipsometry at the Nanoscale* (Springer, 2013).
- [34] A. Arbabi, Y. Horie, M. Bagheri, and A. Faraon, *Dielectric metasurfaces for complete control of phase and polarization with subwavelength spatial resolution and high transmission*. *Nature nanotechnology* **10**, 937 (2015).
- [35] P. S. J. Russell, *Optics of floquet-bloch waves in dielectric gratings*, *Applied Physics B Volume* **39**, pp 231–246 (1986).
- [36] W.-L. Hsu, G. Myhre, K. Balakrishnan, N. Brock, M. Ibn-Elhaj, and S. Pau, *Full-stokes imaging polarimeter using an array of elliptical polarizer*, *Opt. Express* **22**, 3063 (2014).
- [37] N. Gu, B. Yao, L. Huang, and R. C., *Design and analysis of a novel compact and simultaneous polarimeter for complete stokes polarization imaging with a piece of encoded birefringent crystal and a micropolarizer array*, *IEEE Photonics Journal Volume* **10**, Number 2 (April 2018).
- [38] A. Peinado, A. Lizana, J. Vidal, C. Iemmi, and J. Campos, *Optimization and performance criteria of a stokes polarimeter based on two variable retarders*, *Opt. Express* **18**, 9815 (2010).
- [39] S. S. Kruk, A. N. Poddubny, D. A. Powell, C. Helgert, M. Decker, T. Pertsch, D. N. Neshev, and Y. S. Kivshar, *Polarization properties of optical metasurfaces of different symmetries*, *Phys. Rev. B* **91**, 195401 (2015).

- [40] Wikipedia, *Longitudinal mode*, https://en.wikipedia.org/wiki/Longitudinal_mode (2018).
- [41] Wikipedia, *Q factor*, https://en.wikipedia.org/wiki/Q_factor (2018).
- [42] Wikipedia, *Distributed bragg reflector*, https://en.wikipedia.org/wiki/Distributed_Bragg_reflector (2018).
- [43] A. Fong and M. Hsu, *Hyperspectral imaging cameras in rapid detection and potential diagnosis of agricultural crop threats*, HinaLea Imaging (2018).
- [44] Ximea, *Hyper spectral imaging*, IMEC 2014 (2014).
- [45] Wikipedia, *Pleochroism*, <https://en.wikipedia.org/wiki/Pleochroism> (2018).
- [46] A. Martins, J. Li, A. F. da Mota, V. M. Pepino, Y. Wang, L. G. Neto, F. L. Teixeira, E. R. Martins, and B.-H. V. Borges, *Broadband c-si metasurfaces with polarization control at visible wavelengths: applications to 3d stereoscopic holography*, *Opt. Express* **26**, 30740 (2018).
- [47] Wikipedia, *10 nanometer*, https://en.wikipedia.org/wiki/10_nanometer (2018).
- [48] F. Snik and C. U. Keller, *Astronomical polarimetry: Polarized views of stars and planets*, in *Planets, Stars and Stellar Systems: Volume 2: Astronomical Techniques, Software, and Data*, edited by T. D. Oswalt and H. E. Bond (Springer Netherlands, Dordrecht, 2013) pp. 175–221.
- [49] W. Sparks, T. A. Germer, J. W. MacKenty, and F. Snik, *Compact and robust method for full stokes spectropolarimetry*, *Appl. Opt.* **51**, 5495 (2012).